Unraveling sedimentary precursors and metal enrichment of high-grade metamorphosed manganese-rich rocks from the Borborema Province, northeastern Brazil

Felipe Holanda dos Santos[a,b]; Wagner da Silva Amaral[b]; Kurt Konhauser[c]; Douglas Teixeira Martins[b]; Marco Paulo de Castro[d]; Glaucia Nascimento Queiroga[d]; Ernest Chi Fru[e]; Morten B. Andersen[e]

[a]Instituto de Engenharia e Geociências, Universidade Federal do Oeste do Pará, Santarém, PA, Brazil
[b]Departamento de Geologia e Recursos Naturais, Instituto de Geociências, Universidade Estadual de Campinas, Campinas, SP, Brazil
[c]Department of Earth & Atmospheric Sciences, University of Alberta, Edmonton, AB, Canada
[d]Departamento de Geologia, Escola de Minas, Universidade Federal de Ouro Preto, Ouro Preto, MG, Brazil
[e]Centre for Geobiology and Geochemistry, School of Earth and Environmental Sciences, Cardiff University, United Kingdom

Abstract

The Paleoproterozoic Lagoa do Riacho manganese deposit in the Borborema Province is central to unravelling the genesis of Paleoproterozoic manganese deposits, Paleoproterozoic redox evolution and genetic relationship to the West African Craton. With manganese contents averaging 35 wt%, the Lagoa do Riacho manganese unit is lithologically subdivided into oxidized and silicate manganese ores and a garnetite (garnet-rich rocks) subgroup. The oxidized manganese ore consists mainly of pyrolusite, manganese-oxyhydroxide and spessartine. The silicate manganese ore has rhodonite, tephroite and spessartine. Garnetite contains spessartine and minor quartz and rhodonite. The main host rocks include garnet quartzite and graphite-bearing pelitic gneiss. The composition of carbonate inclusions in spessartine-rhodonite and Ca-Mn fractionation between garnet core and rim suggests all these manganese-rich rocks probably formed from protoliths of marl composition. Biogenic, syn-sedimentary graphite in the manganese-rich rocks and their host rocks indicates organic matter was deposited along with the marl protolith. Within this general context and through chemical-petrological relations, we outline an initial environment involving anoxic sediments' deposition (eg., organic matter-rich manganese marl and black shales, and wackes) on the seafloor. The presence of spessartine, rhodonite, and tephroite suggests peak metamorphic conditions reached amphibolite facies conditions (6-7 kbars and 550-700ºC). Amphiboles indicate later retrograde stages and carbonate veins suggest a possible hydrothermal stage after manganese deposition. The metamorphosed manganese-rich rocks were upgraded to medium-grade manganese ores during exposure to surface water. Our results indicated that the manganese-rich rocks and their host rocks were generated in a sedimentary context, possibly in a marine setting with carbonate and organic matter contribution.

Keywords: Paleoproterozoic; Borborema Province; Manganese ore; Sedimentary protolith; Anoxic sediments; Amphibolite facies conditions

1. Introduction

Peak deposition of manganese formations coincided with the Great Oxidation Event (Karhu and Holland, 1996; Holland, 2006), when oxygen rose permanently in the atmosphere ~2.4 billion years ago, suggesting that the transition from the predominantly reducing Archean atmosphere to the oxygen-rich world of the Proterozoic played a crucial role in the global accumulation of Mn deposits (Roy, 2006; Maynard, 2010; Johnson et al., 2016). Mineralogically they are varied, but most commonly include the carbonates kutnohorite ($Ca^{2+}Mn^{2+}[CO_3]_2$) and rhodochrosite ($Mn^{2+}CO_3$), diverse manganese silicates, and the manganese oxides cryptomelane ($K[Mn^{4+}, Mn^{2+}]_8O_{16}$) and pyrolusite ($Mn^{4+}O_2$) (Dasgupta, 1997; Johnson et al., 2016). This variability reflects differences in the composition of the seawater primary precipitates, diagenetic modification in the sediment pile, metamorphic transformations and, in some instances, further alteration during ore formation (Dasgupta et al., 1990, 1993; Calvert and Pedersen, 1996; Mücke et al., 1999; Chisonga et al., 2012; Brusnitsyn et al., 2017; Johnson et al., 2019). Consequently, using manganese-rich rocks to infer paleo-environmental conditions is challenging and requires unraveling the paragenetic sequence of minerals.

To date, geological studies focusing on manganese-rich rocks are limited in number when compared to their iron-rich equivalents, the so-called iron formations (Konhauser et al., 2017). For example, previous studies have primarily been focused on major Paleoproterozoic deposits in Ghana, Gabon and South Africa in the Nsuta, Moanda and Kalahari manganese fields, respectively (Leclerc and Weber, 1980; Gutzmer and Beukes, 1995, 1996; Mücke et al., 1999; Tsikos and Moore, 1997; Nyame, 2001; Tsikos et al., 2001, 2003; Beukes et al., 2016). In Brazil, similar manganese deposits also exist containing proven reserves up to 43 Mt of ore (Chisonga et al., 2012). These deposits share similar age and geological setting with the aforementioned African fields (Roy, 2006; Chisonga et al., 2012; Cabral et al., 2019a; Salgado et al., 2019). For example, the location of the current study is believed to have a common paleographical provenance as the West African Craton (Klein and Moura, 2008; Neves, 2011; Costa et al., 2018; Grenholm, 2019; Grenholm et al., 2019). Moreover, both Brazilian and some African manganese deposits are hosted in carbonaceous black shales and linked to chemical rocks, such as marine carbonates and iron

formations (Roy, 2006; Beukes et al., 2016). However, not much is known about early manganese deposition in the Borborema Province, northeastern Brazil, and processes leading to their ore genesis. This information is crucial for the evaluation of the manganese ore potential in the Borborema Province, global and regional-scale reconstruction of the chemical evolution of Earth surface environments during the Paleoproterozoic, and linkages to the West African Craton prior to plate-tectonics separation.

In this work, we present the mineralogy and composition of the Lagoa do Riacho manganese deposit, the focus of the present study, in order to retrieve information on the nature of the protolith of metamorphosed manganese-rich rocks, their physicochemical depositional conditions, and associated post-depositional alteration processes that enabled the formation of the manganese ore. The Lagoa do Riacho manganese deposit is a representative example of Paleoproterozoic manganese mineralization from the Borborema Province. This deposit is hosted in medium- to high-grade Paleoproterozoic gneisses from the Canindé do Ceará Complex (Fetter et al., 2000; Gomes, 2013; Garcia et al., 2014; Costa and Palheta, 2017; Calado et al., 2019) and might be correlative with other manganese-rich rocks from South America (Chisonga et al., 2012; Cabral et al., 2019a) and Ghana in West Africa (Mücke et al., 1999; Nyame, 2001; Beukes et al., 2016). The deposit was discovered in the northeast of Brazil by the company Libra Ligas do Brazil in 2003. However, operational mining activities in the Lagoa do Riacho mine are relatively recent and date from 2011. Its activities were closed in 2020, and during this period the ore was extracted in three open-pits, with rocks containing up to 45 wt% of manganese ore. Unfortunately, there is no further data available for publication on manganese resources at this time.

2. Geological setting

2.1. Borborema Province

The Borborema Province in northeastern Brazil is believed to have been located adjacent to the West African Congo and São Francisco cratons before the opening of the Atlantic Ocean, during the Gondwana assembly around 600 Ma (Caby, 1989; Castaing et al., 1994; Brito Neves et al., 2000; Neves, 2003; De Wit et al., 2008) (Fig. 1A and B). In this context, the Borborema Province represents the westernmost segment of this palaeocontinent (Torsvik and Cocks, 2013).

Apart from the Late Neoproterozoic history, the Northern Borborema Province basement is mostly composed of Paleoproterozoic rocks (2.3-2.0 Ga) developed through juvenile arc

accretion (Fetter et al., 2000; Martins et al., 2009; Neves, 2011; Costa et al., 2015; Souza et al., 2016; Costa et al., 2018). This has led some authors to point out some geotectonic similarities between these rocks and the Birimian succession in West Africa (Klein and Moura, 2008; Neves, 2011; Costa et al., 2018; Grenholm, 2019; Grenholm et al., 2019) (Fig. 1B). Accordingly, Grenholm et al. (2019) depicted a pre-Atlantic reconstruction of South America and Africa. They placed the Northern Borborema Province adjacent to the West African Craton, suggesting a connection between both terranes.

The Borborema Province consists of several Archean nuclei composed mostly of TTG orthogneisses (Fetter 1999; Dantas et al. 2013; Ganade et al., 2017), a Palaeoproterozoic basement formed by orthogneisses, migmatites and various supracrustal rocks (Fetter et al., 2000; Hollanda et al., 2011; Souza et al., 2016; Costa et al., 2018). Additionally, a series of Meso- to Neoproterozoic granitic intrusions, metasedimentary rocks and shear zones (e.g., Patos, Pernambuco, and Transbrasiliano) developed towards the end of the Neoproterozoic era (Vauchez et al. 1995; Neves and Mariano 1999; Viegas et al. 2014) (Fig. 1B). Brito Neves et al. (2000) propose a division of the Borborema Province into three major structural domains: the (1) Northern Borborema Province, including the Médio Coreaú, Ceará Central, and the Rio Grande do Norte domains; (2) Central Domain; and (3) Southern Domain.

The Northern Borborema Province comprises an expressive Rhyacian granitic and gneissic belt and related metavolcanosedimentary sequences of the same age hosting the manganese-rich rocks presented here (Fetter et al., 2000; Hollanda et al., 2011; Costa et al., 2015; Souza et al., 2016).

2.2. Manganese mineralization from the Northern Borborema Province

Several manganese-rich rocks occur along an N-NE-directed trend within the Paleoproterozoic units of the Northern Borborema Province (Souza and Ribeira Filho, 1983; Gomes, 2013; Costa and Palheta, 2017) (Figs. 2A and B). In many cases, these are ore-grade manganese-rich rocks containing at least 35 wt% MnO_2. They are interbedded with amphibolite facies metamorphic rocks, including graphitic pelites, garnet-bearing quartzites, metagraywackes, metaconglomerates and calc-silicate rocks (Souza and Ribeira Filho, 1983; Gomes, 2013). The ore consists predominantly of the following manganese minerals: rhodochrosite, spessartine ($Mn_2^{3+}Al_2[SiO_4]_3$), rhodonite-pyroxmangite (Mn^{2+},Fe^{2+},Mg,Ca,SiO_4), and tephroite ($Mn^{2+}{}_2SiO_4$),

along with non-Mn gangue minerals such as graphite (C), pyrite ($Fe^{2+}S_2$) and pyrrhotite ($[Fe^{2+}]_{1-x}S$). Localized supergene enrichment to manganese oxide layers is recorded by massive crystallization with pyrolusite, manganite ($Mn^{3+}O[OH]$), cryptomelane, and todorokite ($[Na,Ca,K,Ba,Sr]_{1-x}[(Mn,Mg,Al]_6O_{12}\cdot nH_2O$ (Souza and Ribeira Filho, 1983; Gomes, 2013).

The Lagoa do Riacho manganese deposit is located within this mineralization trend (Figs. 2B and C). It is hosted within the Canindé do Ceará Complex, which is subdivided into two sub-domains: (1) paragneisses and schists interbedded with marbles, quartzites, calc-silicate rocks, amphibolites, and manganese and iron formations; and (2) orthogneisses of granitic to tonalitic composition and subordinate amphibolites (Fetter et al., 2000; Castro, 2004; Torres et al., 2007; Costa and Palheta, 2017) (Fig. 2B). Orthogneisses yield a U-Pb zircon crystallization age of 2.15 Ga and a Sm-Nd model age (TDM) of 2.4-2.3 Ga (Fetter et al., 2000; Castro, 2004). The gneissic rocks hosting the manganese-silicate rocks at the southern part of the Lagoa do Riacho manganese deposit have a U-Pb zircon crystallization age of 2.13 Ga (Gomes, 2013). For the first sub-domain, a maximum sedimentation age of 1.9 Ga was determined by U-Pb on a detrital zircon in a quartzite by Costa and Palheta (2017).

3. Materials and methods

3.1. Drill core description (macroscopic features)

The studied manganese-rich rocks have been sampled from three drill cores (Ocr-1; Ocr-4; Ocr-8) provided by Libra Ligas do Brasil S.A. (Fig. 2C). A systematic petrographic study was carried out on these core samples to define their general macroscopic features and mineral paragenetic sequence. Core Ocr-1 shows an approximate 50 m oblique section crosscutting, from top to base, mainly oxidized manganese ore (OMO), garnet quartzite and reaching the basement, composed of graphitic-bearing pelitic gneiss (host-rock), in the lower part of the core (Fig. 3). Core Ocr-4 is a 38 m oblique section that crosses a garnetite unit in its lower parts and a granitic rock in the bottom and does not reach the graphitic-bearing pelitic gneiss (Fig. 3). Core Ocr-8 is an oblique 46-m long section that crosses a thick layer (approximately 20 m) of garnet quartzite and OMO and garnetite interbedded with garnet quartzite at the bottom (Fig. 3). A layer of silicate manganese ore (SMO) is observed through the three cores (Fig. 3). Additionally, lateritic manganese crust is present at the top of the cores (Fig. 3).

3.2. Petrographic analysis

Thin and polished sections of representative samples were used in petrographic studies with transmitted and reflected light microscopy, respectively. Petrographic studies were performed in the Microscopy Laboratory of the Institute of Geosciences, University of Campinas, and in the SEMlab of the Federal University of Ceará, using a polarized light microscope Leica model DM 50P. Petrographic studies were complemented by qualitative mineralogy with X-ray diffraction (Appendix A) using a PANalytical X'Pert Pro diffractometer at the Institute of Geoscience, UNICAMP. Data reduction (smoothing, background subtraction, peak searching, profile fitting, and error correction) and mineral phase identification from powder diffraction was made using the Match! Version 2.0 software.

3.3. Chemical analyses of minerals and whole rock

Electron Microprobe Analysis (EMPA) was performed using a JEOL JXA-8230 super probe, equipped with five wavelength dispersive spectrometers (WDS), at the Microscopy and Microanalysis Laboratory (LMic) at the Department of Geology, Federal University of Ouro Preto, Brazil. Six different crystals were used: thallium acid phthalate on H-type spectrometer (TAPH in WDS 1), thallium acid phthalate (TAP in WDS 2), lithium fluoride on H-type spectrometer (LIFH in WDS 3), pentaerythritol on H-type spectrometer (PETH in WDS 3), pentaerythritol (PETL in WDS 5) and lithium fluoride (LIFL in WDS 5). The JEOL EMPA software Ver3.0.1.16 package was used to perform the calibration, overlap correction and quantification. Operating conditions were 15kV accelerating voltage, 20nA beam current and 5 μm beam diameter (1 μm was used for tiny grains). The work distance on EMPA is fixed at 11 mm with no variation during the analysis. The following standards were used for calibration: anorthoclase (Na), CaF_2 (F), quartz (Si), corundum (Al), olivine (Mg), $BaSO_4$ (Ba), magnetite (Fe), scapolite (Cl), chromite (Cr), fluor-apatite (P and Ca), strontianite (Sr), rutile (Ti), microcline (K) and MnO (Mn). Counting time for Ba, Sr and P was set at the 30s at peak and 15s at the background, while Na, F, Si, Al, Mg, Fe, Cl, Ti, Ca, K and Mn was set at 10 s at peak and 5 s at the background. The major spectral interferences were corrected during the standard analysis and the quantification. Lα X-ray was used for Ba and Sr while Kα X-ray was used for Na, F, Si, Al, Mg, Fe, Cl, P, Cr, Ti, Ca, K and Mn. The standard deviation to each element was: Na (1.00%), F (1.12%), Si (0.30%), Al (0.29%), Mg (0.47%), Ba

(0.34%), Fe (0.42%), Cl (1.74%), Cr (0.62%), P (0.64%), Sr (0.79%), Ti (0.21%), Ca (0.24%), K (0.5%), Mn (0.41%). The total iron content obtained by the microprobe is considered as FeO.

To determine the crystallization temperature of the carbonaceous matter (graphite) related to the manganese-rich rocks, we analyzed 50 graphite crystals from the rock matrix of the manganese-rich rocks and graphite-bearing pelitic gneiss by Raman spectroscopy. A Renishaw Raman microscope (inVia Reflex) coupled to a Leica DM2500M microscope at the Astrolab of the Chemistry Institute, University of São Paulo (USP), was used in order to acquire the Raman spectra of the carbonaceous matter. The selected crystals (in polished thin sections) were directly exposed to an Ar laser (532 nm) for 5s at a power of 10 mW to obtain a Raman shift spectra (2000-1100 cm^{-1}). Ten spectra in different crystals were acquired for each polished thin section. Data processing, including peak position, G, D1, and D2 band-area and full width at half maximum (FWHM), was performed using an open-source Fityk computer program. A graphite Raman spectrum is formed of first- and second-order regions, the first-order region ranging from 1100 to 1800 cm^{-1} and is often considered for thermobarometric studies in the carbonaceous matter (Beyssac et al., 2002). In this region, a graphite band occurs at around 1580 cm^{-1} (G band) in well-ordered graphite, whereas disordered graphite displays adjacent bands at 1350 cm^{-1} (D1), 1620 cm^{-1} (D2) and 1500 cm^{-1} (D3). The metamorphic temperature can be calculated using the following parameters from Beyssac et al. (2002) in equation I:

(I) T(ºC)=−455ºC x D1/(G+D1+D2) band area ratio + 641.

This equation works in the temperature range of 330 to 650°C, encompassing the greenschist to amphibolite facies metamorphism field and with an absolute accuracy of ± 50°C. The thermometer error is estimated at ± 50°C. Although graphitization would be an irreversible process, and thus graphite always records peak temperature, mechanical deformation can reduce the registered temperature (Barzoi, 2015; Kirilova et al., 2018). Hence, concerning reducing the effects of deformation, we use a correction factor from Barzoi (2015) in addition to the Beyssac et al. (2002) classical thermometer. The corrected temperature is calculated by equation II:

(II) $T_{corrected}=T[i] / \zeta_{strain}$

where ζ_{strain} represent positive values, with a maximum of 1 for high strained graphite samples, and T[i] is the temperature extracted from the equation I above.

The core Ocr-4 (twenty-one samples) was chosen for presenting geochemical data since it contains all range of lithological groups from this study, except the graphite-bearing pelitic gneiss extracted from the core Ocr-1. Thus, twenty-two samples were geochemically investigated. Sample preparation, major oxide geochemical analyses and carbon content determination were performed at the SGS-GEOSOL laboratory. Samples were crushed and ground to < 75 μm with respectively jaw crusher and agate mill. For major oxide, 2g of rock powder was mixed with lithium metaborate/tetraborate and heated up to 1050 °C in a muffle for 15 min. The corresponding molten material was dissolved in dilute HNO_3 (5%) and analyzed in a Phillips PW 2404 X-ray fluorescence spectrometer (XRF) using the following standards, SG-142, AMIS0258 and OREAS171. Detection limits are between 0.1 and 0.01 wt.%. For carbon content, samples were analyzed by combustion and CO_2 infrared detector techniques in a LECO equipment model CS-775. The international standard GGC-04 measured the external precision and detection limit are below 0.05%.

4. Results

4.1. Field relationships and macroscopic features of the manganese-rich and associated rocks

The Lagoa do Riacho manganese deposit occurs within a synform plunging to E-NE and S-SW. The deposit operated from three open pits and is hosted by a graphite-bearing pelitic gneiss, which is only exposed at the cores. The graphite-bearing pelitic gneiss belongs to the Canindé do Ceará Complex. The manganese-rich rocks from the Lagoa do Riacho mine show three distinct lithological groups, all containing graphite along foliation planes. The first occurs in the upper section of the cores and consists of oxidized manganese ore (OMO). The second group is formed by massive or banded silicate manganese ore (SMO), as lenses within the OMO. The third group is constituted by a finely banded spessartine-rich lithology, garnetite, with minor silicate manganese minerals.

At the mine site, there is a continuous interstratification of OMO with garnet quartzite (Figs. 4A, B, and C). The garnet quartzite is commonly fractured and has several generations of manganese oxyhydroxide ([$MnO(OH).nH_2O$]) veinlets crosscutting its bedding (Fig. 4D). The OMO appears in a 45º tilted contact with a garnet quartzite and is intruded by irregular aplitic

veins (Figs. 4E and F). Both lithological groups (OMO and garnet quartzite) extend laterally between the open pits. Manganese lateritic duricrusts and locally pisolitic crusts crop out at its uppermost surface, above the garnet quartzite.

The OMO is a banded, fine- to medium-grained rock with mm- to cm-thick, well-developed, grayish black, pyrolusite-graphite bands interleaved with pale-brownish, granular garnet-quartz (SiO_2)-pyroxene-rich bands (resemble a S_0 relict banding). Most of the pyrolusite is in close contact with mm-sized graphite (Figs. 5A and B). The gray to black appearance of the bands results from this association; locally, this looks like a graphitic rock due to the high content of this mineral in the rock matrix (Fig. 5C). Pyrolusite and cryptomelane also form interconnected veinlet networks with a dendritic texture that crosscut garnet-quartz bands (Figs. 5B-D). In general, the medium- to fine-grained quartz-garnet-rich bands are thinner than the pyrolusite and the graphite-rich bands.

The SMO varies from layered to massive rocks composed of manganese silicate-oxide minerals (Figs. 5E-H). It contains mm- to cm-thick bands of pinkish-white, fine-grained quartz-pyroxene-olivine and dark gray fine-grained pyrolusite + cryptomelane (Fig. 5E). Pale brownish garnet occurs in rims of manganese-oxyhydroxide-rich bands (Fig. 5E). The manganese-oxyhydroxide appears as greenish-black linear clusters along the foliation and crosscutting it as pyrolusite veinlets (Fig. 5E). Cryptomelane veinlets also cross the pyroxene-rich matrix (Fig. F). Massive SMO is present as meter-sized lenses within the spessartine-bearing rocks in the lower section of drill core Ocr-8 (Figs. 5G-H).

Garnetite occurs at the lower section of cores Ocr-4 and Ocr-8. It is a very fine-grained, grayish to white and green rock. It contains mm- to cm-sized bands of garnet spessartine interbedded with calc-silicate minerals (e.g., epidote ($Ca_2[Fe^{3+}, Al]_3[SiO_4]_3[OH]$), pyroxene), plagioclase ($[Na, Ca]\ [Si, Al]_4O_8$) and tiny flakes of graphite (up to 1 mm) (Figs. 6A and B). Graphite appears as mm-sized flakes disseminated throughout and aligned along the rock's foliation planes. Minor amounts of mm-sized pyroxene are recognized as brownish-green and pinkish agglomerate spots (Figs. 6A and B). Some veinlets filled by carbonate and biotite ($K[Mg, Fe^{2+}]_3AlSi_3O_{10}[OH, F]_2$) locally occurs closely related to spessartine garnet.

Several garnet quartzite beds are 0.5–12 m thick, with ochre to gray colors, commonly interbedded with the manganese-rich rocks. These rocks show a continuous foliation composed almost exclusively by an alignment of medium- to coarse-grained quartz-feldspar ([K, Na, Ca] [Si,

Al]$_4$ O$_8$) -garnet (Fig. 6C-E). The garnet quartzite contains spots of graphite (up to 5 mm) that appears either slightly oriented or randomly distributed (Figs. 6D and E). Minor sulfide minerals occur in these rocks (Fig. 6F). At the base of the Ocr-1 core, there exists light- to dark-gray colored, graphite-bearing, medium- to coarse-grained pelitic gneiss containing centimeter-sized garnet porphyroblasts and sillimanite (Fig. 6F). This rock hosts all previously described lithological groups. Garnet and sillimanite are wrapped by a continuous, spaced foliation defined by biotite, muscovite ($KAl_2[Si_3Al]O_{10}[OH, F]_2$) and graphite flakes at the base of the Ocr-1 core.

In addition, granitoid appears in the cores with an approximate thickness up to three meters crosscutting the manganese-rich rocks, with a metamorphic aureole along the contact (Fig. 6H). It is a pinkish, medium- to coarse-grained, leucocratic granite. In some cases, it has pegmatoid texture and is composed of quartz, K-feldspar, and plagioclase.

4.2 Mineralogical and textural features

Table 1 summarizes the minerals described in the following lithological groups.

4.2.1. Oxidized manganese ore - OMO

The classification of OMO is descriptive and based upon the predominance of manganese-oxyhydroxide minerals and spessartine garnet (>50%). Spessartine porphyroblasts contain abundant micro-crystalline carbonate (Ca,Mn[CO_3]) inclusions (up to 100 μm), which form aligned trails. However, it also appears with an inclusion-free core (Fig. 7A). Some manganese pyroxene and tephroite are present in the matrix of the ore and crosscut by pyrolusite and cryptomelane veinlets (Figs. 7B and C). In less weathered sections some manganese amphibole appears in contact with graphite (Fig. 7D). Pyrolusite occurs as abundant veinlets within fractures, gemination planes of some minerals (e.g., manganese pyroxene), in pockets at rock matrix and as interstitial subhedral to anhedral prismatic crystals (Fig. 7E). Todorokite is a ubiquitous secondary mineral throughout the pyrolusite-spessartine manganese ore, always as a pseudomorphic phase of manganese silicate minerals and having a distinct fibrous habit recognizable in reflected light and BSE images (Fig. 7F). Cryptomelane is also present as a secondary mineral in fractures; other than typical dendritic habit, it also displays a zoned colloform texture (Fig. 7G).

4.2.2. Silicate manganese ore - SMO

Manganese pyroxene is the most common silicate (>70%) in the SMO (Fig. 8A). In general, it is idioblastic-subidioblastic, equigranular and shows a mosaic texture (Fig. 8B). Manganese rich amphibole may be locally replaced by manganese pyroxene (Figs. 8C and D). Spessartine garnet is commonly in straight contact with manganese pyroxene, but also as inclusions in the latter. Tephroite occurs in minor content (<5%) in irregular contact with manganese pyroxene. Minor carbonate inclusions are found in manganese pyroxene (Fig. 8D).
Other minerals include pyrolusite, Fe-Mn oxyhydroxide (jacobsite and todorokite), cobaltite (CoAsS), pyrite, chalcopyrite ($CuFe^{2+}S_2$), pyrophanite and graphite. Cobaltite is found with triple points, having a straight boundary shape with spessartine (Fig. 8E). Other common sulfide minerals are pyrite and chalcopyrite, which are found as xenoblastic-subidioblastic crystals in contact with manganese pyroxene. Pyrophanite exhibits rounded to fine-grained, irregular habits (Fig. 8F).

4.2.3. Garnetite

Taking into account the high spessartine garnet content of this rock (>80%), the petrographic classification garnetite has been adopted, although gondite (Roy and Mitra, 1964) and "coticules" (Spry, 1990) are another common terms. However, garnetite is preferred to gondite and coticules because it has no genetic connotation.

Garnetite forms a thinly, banded rock (mm-sized) showing alternations of spessartine garnet and quartz-rich layers (Fig. 9A). Spessartine is subidioblastic-idioblastic (up to 2.5 mm) and grows along a continuous foliation plane (Figs. 9A and B). Mica occurs in interstitial areas close to spessartine rims (Fig. 9C). Quartz appears as idioblastic to xenoblastic, fine-grained crystals (up to 2.5 mm) with granoblastic texture in the rock matrix. Pyroxene is idioblastic-subidioblastic in equigranular crystals, with prismatic to irregular habits and commonly occurring in contact with spessartine garnet (Fig. 9D). Xenoblastic amphibole is generally a minor component replacing pyroxene (Fig. 9E).

Aligned, fine-grained (mm-sized) graphite flakes define the primary sedimentary bedding ($S_0//S_1$). Locally, epidote with titanite ($CaTiSiO_5$) inclusions occurs as isolated or agglomerated, fine-grained granular crystals along the foliation in contact with spessartine, quartz and pyroxene (Fig. 9F). Carbonate is a minor component and only as veinlets transversely crosscutting

spessartine and other matrix minerals, such as quartz and manganese pyroxene (Fig. 9G). Pyrite and chalcopyrite are local with xenoblastic and idioblastic habits.

4.2.4. Associated rocks (garnet quartzite and graphite-bearing pelitic gneiss)

The host rocks of the manganese ore are represented mainly by a: (i) medium- to coarse-grained garnet-quartzite, and (ii) graphite-bearing pelitic gneiss. For the garnet-quarzite, there are also numerous millimeter-sized garnet porphyroblasts (up to 1.25 mm) that are aligned, and thus define a continuous foliation plane (Fig. 10A). Medium-grained subidioblastic plagioclase and quartz constitute matrix minerals. Millimeter-sized (up to 2.5 mm) microcrystalline graphite flakes are abundant and commonly aligned along the foliation plane with garnet, quartz, and plagioclase. Although well-developed graphite flakes are predominant throughout the rock matrix, they are a lower crystallinity variety (Figs. 10A and B), they display an amorphous pseudo-spheroidal habit, and they occur in close relationship with garnet and pyrite. In some cases, between graphite lamellae, there exist covellite overgrowths. Pyrite and chalcopyrite appear as small, elongated individual crystals in close association with graphite. These sulfide minerals have massive, medium-grained, subhedral and anhedral shapes. Additionally, pyrite may have inclusions of covellite (CuS) in its core (Fig. 10C). Similarly, to the other lithological groups, pyrophanite appears as rounded to fine-grained irregular crystals (Fig. 10D).

For the graphite-bearing pelitic gneiss, quartz locally displays undulatory extinction and is recrystallized in sub-grains. It defines semi-continuous granoblastic lenses with feldspar (K-feldspar and albite) and cordierite ($Mg_2Al_4Si_5O_{18}$). Biotite and muscovite form conspicuous lepidoblastic layers intercalated with granoblastic layers and define a Sn foliation. This Sn foliation is usually anastomosed and wraps garnet porphyroblasts. Brownish biotite occurs as medium- to fine-grained lamellae with quartz and zircon inclusions, locally replacing garnet and sillimanite (Al_2SiO_5). Centimeter-sized, subidioblastic garnet porphyroblasts are commonly fractured (Fig. 10E). Some garnet varieties have inclusion-free cores, while others have quartz, plagioclase and biotite inclusions in their cores. Prismatic, xenoblastic sillimanite forms thin porphyroblasts along the S_n foliation in contact with biotite and garnet (Fig. 10F). Graphite flakes are ubiquitous and distributed along the main foliation.

4.3 Mineral chemical composition

Representative electron microprobe chemical compositions of garnet, pyroxene, olivine, amphibole, mica, feldspar, carbonate, pyrophanite, and manganese oxyhydroxides, from all lithological groups described in the previous section (4.2), are presented in Appendix B. All manganese and iron are reported as total MnO and FeO, respectively.

4.3.1. Garnet

The garnet chemical composition from the OMO, SMO and garnetite contains average contents of ca. 0.82, 0.80, and 0.80 mols% of the spessartine end member [X_{Spss} = Mn/(Fe + Mn + Mg + Ca)], respectively (Appendix B and Fig. 11A). In these manganese-rich rocks, garnet spessartine porphyroblasts normally exhibit irregular compositional zoning with a conspicuous core-to-rim decrease from 0.9 to 0.8 of the X_{Spss} (Figs. 12A and A'). Conversely, there is an increase from the core to rim in the grossular molecule, X_{Grs} [(Ca/(Fe + Mn + Mg + Ca)]. This chemical zoning pattern is locally reversed, with a core-to-rim increase of X_{Sps}=0.8–0.84 (Figs. 12C and C'). In general, the increase of X_{Spss} in these manganese-rich rocks is compensated by a decrease of X_{Grs} and vice versa. The garnet quartzite, in turn, presents higher X_{Alm} (mean 0.08 mol%) and X_{Prp} (mean 0.12 mol%) contents and lower contents of X_{Spss} (0.71 mols% average) than the OMO, SMO and garnetite (Figs. 12E and E'). The garnet chemical composition from the graphite-bearing pelitic gneiss is mainly constituted of X_{Alm} (0.67-0.73) and X_{Prp} (0.17-0.26), and secondarily X_{Spss} (0.04-0.07) and X_{Grs} (0.03-0.04) (Appendix B and Figs. 12F and F'). There is an increase from 0.67 to 0.73 of the X_{Alm}, from the core to rim, whereas X_{Prp} decreases from the core to the rim (0.25 to 0.15 mol%, respectively). The overall variations in the molar fractions of some components may be better visualized in the Ca-(Fe+Mg)-Mn ternary diagram, and the garnet X-ray maps (Figs. 11A and 13).

4.3.2. Manganese pyroxene

All analyzed manganese pyroxene from the OMO exhibit a rhodonite composition with 0.71–0.69 mol% manganese pyroxene (Pxmn), 0.11–0.10 mol% wollastonite (Wo), 0.13–0.11 mol% enstatite (En) and 0.07-0.05 mol% ferrosilite (Fs) (Appendix B and Fig. 11B). Besides the rhodonite composition, some pyroxene from the SMO also presents 0.76–0.48 mol% diopside (Di), 0.56–0.52 mol% hedenbergite (Hd) and 0.38–0.13 mol% johannesite (Jo) (Fig. 11C).

Pyroxene from garnetite has rhodonite composition and Pxmn average of 0.70 mol% (Appendix B). In the garnetite, the minor Pxmn content compared to the OMO and SMO groups is balanced by a higher Fs content (mean 0.08 mol%).

4.3.3. Olivine

Olivine from the OMO is predominantly of the tephroite-rich end members ($Mg_{0.17}Fe_{0.10}Ca_{0.2}Mn_{0.72}$; Fig. 11D and Appendix B). Only small variations in the FeO (6.4-6.9 wt%) and MgO (7.9-7.0 wt%) contents are observed, except for one tephroite-rich olivine, which yielded the highest FeO (7.6 wt%) and lowest MgO contents (4.0 wt%).

4.3.4. Amphibole

The chemical composition of garnetite amphibole, SMO, and garnet quartzite is mainly mangano-cummingtonite, with a few closer to the mangano-tremolite composition in the garnetite (Fig. 11E). Excluding amphibole with a mangano-tremolite composition that has CaO mean values of 17 wt%, the average CaO content is close to 4.5 wt% (Appendix B).

4.3.5. Carbonate

All carbonate minerals are from inclusions within spessartine garnet (OMO) and manganese pyroxene (SMO). These inclusions display chemical composition close to manganese calcite and kutnohorite, between calcite (Ca-rich) and rhodochrosite (Mn-rich) end members, as shown in the calcite – (magnesite + siderite) – rhodochrosite ternary diagram (Fig. 11F). The carbonate inclusions display small variations in the X_{Clc} and X_{Rhc} contents (0.66-0.75 wt.% and 0.22-0.31 wt.%, respectively) and have a formula range of $Mn_{0.22–0.31}Ca_{0.66–0.75}Mg_{0.02–0.04}FeCO_3$ (Fig. 11F and Appendix B).

4.3.6. Pyrophanite

Pyrophanite presents composition close to the ideal stoichiometry with a formula range of $Mn_{0.98–0.86}Fe._{0.13–0.02}MgTiO_3$ (Fig. 11G and Appendix B). Two pyrophanite groups are distinguished based on the ilmenite mol% content, one with 0.08-0.13 mol% and another with 0.02-0.05 mol%. These differences in the ilmenite end-member values are counterbalanced by the increase and decrease of pyrophanite end members, respectively.

4.3.7 Manganese oxyhydroxides

Manganese oxyhydroxides are sub-divided into pyrolusite, cryptomelane, and Fe-Mn oxyhydroxide. Pyrolusite displays uniform chemical composition, formed basically by manganese oxide (MnO; up to 78 wt%). Minor contents (0.1-0.5 wt%) of Al_2O_3, MgO, CaO, Na_2O, K_2O, CoO, and NiO are documented (Appendix B). Additionally, in one sample SiO_2 content reaches up 10 wt%. Iron is in general below the detection limit. The X-ray map shows pyrolusite in the rock matrix with low Si content and similar Mn values throughout (Fig. 13). Cryptomelane and undifferentiated manganese oxyhydroxides have minor manganese content compared to pyrolusite (Appendix B). Figure 14 shows the principal compositional differences regarding pyrolusite, cryptomelane, and undifferentiated manganese oxyhydroxides.

4.3.8 Mica and Feldspar

Two types of mica are recognized, manganese phlogopite in garnetite and biotite in the graphite-bearing pelitic gneiss (Fig. 14D). Manganese phlogopite has MnO up to 1.5% wt% (Appendix B). All biotite is in contact with spessartine garnet and have TiO_2, FeO and MgO values ranging from 1.30-1.86 wt%, 16.52-16.91 wt%, and 8.57-10.78 wt%, respectively (Appendix B). Two types of feldspar from the graphite-bearing pelitic gneiss were analyzed: one close to the oligoclase (mean 0.74 mol% of Ab) composition, whereas the second (microcline) displays minor Na content with mean K/K+Na+Ca = 0.88% (Fig. 14E and Appendix B).

4.4. Whole-rock chemical composition

Twenty-one whole rock chemical analyses are presented in Appendix C and Figure 15, including one sample of granitic rock from the local basement, for core Ocr-4.

The OMO is characterized by a wide range of SiO_2 contents (20.4–44.2 wt%), associated Al_2O_3 (9.51–20.5 wt%), Fe_2O_3 (5.61 to 11.6 wt%), and MnO (25.8 to 33.1 wt%), and subordinate concentrations of K_2O (0.35–2.9 wt%), CaO (0.19 to 2.59 wt%) and MgO (0.52 to 1.64 wt%). The SMO yielded variable SiO_2 (10.4–43.7 wt%), MnO (22.5–41.5 wt%), Al_2O_3 (7.73-13.9 wt%) and Fe_2O_3 (4.96-16.9 wt%) contents with minor CaO (0.23–3.64 wt%), MgO (0.37–1.84 wt%) and K_2O (0.27–3.86 wt%) concentrations. The garnetite has similar SiO_2 (37-41.1 wt%) and MnO (33.6-35.7 wt%), slightly minor Al_2O_3 (8.25-10 wt%), Fe_2O_3 (4.66-5.25 wt%), K_2O (0.01-0.93 wt%) and higher CaO (2.81-4.89 wt%) and MgO (3.04-3.68 wt%) contents than the OMO and

SMO. The contents of graphitic carbon in the manganese-rich rocks reach 3.09 wt%. The garnet quartzite has higher SiO_2 (42.1-57.3 wt%) and K_2O (up to 8.82 wt%) and minor MnO (5.88-26.7 wt%) contents compared to the manganese-rich rocks previously reported above. The granitic rock displays an acidic composition (70 wt% of SiO_2) and low MnO content (1.29 wt%).

The geochemical profile along core Ocr-4 allows better assessment of the compositional heterogeneities of the described lithological groups (Fig. 15). In general, MnO has a positive correlation with Fe_2O_3, (r^2= 0.13) and CaO (r^2= 0.29), a strong anti-correlation with SiO_2 (r^2= 0.72) and weak correlation concerning MgO (r^2= 0.056) contents. Although the graphitic carbon content is irregular and the profile has some gaps, it concentrates along all the manganese-rich rocks.

4.5. Thermodynamic modeling and P-T-X conditions

Thermodynamic calculations were carried out to constrain P-T-X relationships during the evolution of the manganese-rich succession and their host rocks with independent methods from micro-Raman spectroscopy, pseudosection modeling, and isopleth thermobarometry, as presented below.

4.5.1. Micro-Raman thermometry on graphite (carbonaceous material)

The metamorphic peak temperatures of graphite are over 580ºC-652ºC, 509ºC-664ºC, and 597ºC-634ºC for the OMO, SMO, and garnetite, respectively. Although the temperature ranges are large, they lie within the amphibolite facies and in agreement with the thermometer error. The graphite-bearing pelitic gneiss and garnet quartzite yield temperatures ranging between 582-639ºC and 539-675ºC, respectively. Considering uncertainties and limitations related to the applied method, the estimated metamorphic peak temperature of graphite for the manganese-rich rocks is broadly in agreement with the graphite temperature reached for the host rocks (e.g., graphite-bearing pelitic gneiss). Detailed micro-Raman thermobarometric results are shown in Table D.1 (Appendix D); textural features and Raman spectra of the analyzed graphite crystals are found in Figures D.1 and D.2 (Appendix D), respectively.

4.5.2. Petrological phase equilibria modeling of silicate manganese ore and graphite-bearing pelitic gneiss

In a pseudosection (equilibrium phase diagrams), minor chemical changes in a genetically related rock group will result in minor topological differences in the graphs. Thus, as minerals from pelitic rocks are susceptible to pressure and temperature changes (Palin and Dyck, 2020), only one representative sample of the graphite-bearing pelitic gneiss was chosen to provide these measurements. Similarly, one representative sample of the SMO group was chosen because it contains a full mineral assemblage, from carbonates to oxides and silicates.

The P-T, T-X(CO_2) and log$f$(S_2) vs. log$f$(O_2) pseudosections have been calculated following the Gibbs free-energy minimization approach using the Perple_X (Connolly, 2005) software and the internally consistent thermodynamic database for mineral and fluids of Holland and Powell (1991, 1998; updated 2004).

For the host rock (sample 10029; graphite-bearing pelitic gneiss), the MnNCa(KF)MAST-COH chemical system was used under a specific bulk-rock composition (Fig. 16 and Appendix C). The following solution models from White et al. (2014) were used: "Bi (W)" for biotite; "Mica (W)" for muscovite, "Gt (W)" for garnet, "St (W)" for staurolite, "Crd (W)" for cordierite, "melt (W)" for the silicate melt, in addition to the C-O-H (COH) fluids. The model 'feldspar' is based on the solution model of Fuhrman and Lindsley (1988). Due to the abundance of graphite in this rock (which indicates low $f$$O_2$), the chemical system was saturated in C-O-H fluids with reduced H_2O activity (e.g., Connolly and Cesare, 1993). The O_2 content was constrained at a ratio of $2H_2$:$1O_2$, according to Bartoli et al. (2013; JMG). These initial conditions (e.g., X_O = 1/3 of Connolly and Cesare, 1993) are the most suitable for graphite precipitation (Huizenga, 2011). The amount of H_2O content used in modeling the graphite-bearing pelitic gneiss was assumed as the loss of ignition from XRF. For the SMO (sample 10046) two pseudosections were prepared, one in the MnCaMAST chemical system under isobaric T–X(CO_2) conditions and another through the MnCa(F)S-C chemical system as a function of log$f$(S_2) vs. log$f$(O_2) (Fig. 17). All modeled phases in the MnCaMAST chemical system are considered as pure end members and binary H_2O-CO_2 fluid in excess. The FeO was neglected because it changes the equilibria of some end members, specifically tephroite, and besides all studied manganese silicate are iron-poor end members (see Appendix B). Potassium was also not included because, excluding cryptomelane, the mineral assemblage is potassium poor. Through this system, we evaluated the equilibria between manganese-rich silicates (e.g., spessartine, rhodonite, tephroite) with pyrophanite and carbonates (calcite and rhodochrosite). The redox state of the system was constrained using the MnCa(F)S-C

system in a log$f(S_2)$ vs. log$f(O_2)$ grid. The solution model of pyrrhotite from Holland and Powell (1998) was used and rhodonite, tephroite, spessartine, pyrolusite, rhodochrosite, calcite, graphite, pyrite, and quartz as pure end members.

In the pseudosection under the MnNCa(KF)MAST-COH system (graphite-bearing pelitic gneiss; Sample 10029) (Fig. 16), the near-peak conditions have been estimated by combining natural petrological observations with compositional isopleths of garnet (X_{Mg} and X_{Ca}) and feldspar (X_{Ab}). Notably, we observe an intersection of X_{Mg} (0.69) and X_{Ca} (0.04) compositional isopleths for garnet at 707 °C and 6.2 kbar that closely matches with natural observations (Figs. 16B and D). Besides, combining the compositional isopleths of XMg (0.69) and plagioclase (XAb = 0.7) constrains P–T conditions to ~7.2 kbar at ~687 °C, which is also following petrographic assemblages found in thin sections. This result indicates that the graphite-bearing pelitic gneiss equilibrated at these P-T conditions.

The pseudosections of the MnCaMAST system for SMO (sample 10046) consist predominantly of large trivariate fields (Fig. 17A). Spessartine is stable in practically all fields, except at lower temperatures (T < 420ºC) for X(CO_2) > 0.2. At a temperature higher than 540ºC, tephroite and rhodonite stability fields extend over almost all X(CO_2), 0.1-0.97. Carbonates (calcite and rhodochrosite) are not stable only between 610-750ºC for 0.01 X(CO_2) (field 9 in Fig. 17A, left upper corner). At lower temperatures (<500ºC), some fields contain cummingtonite, kaolinite, paragonite, and pyrophyllite. In the pseudosection, the highlighted field in blue contains the near-peak mineral assemblages described in the petrographic section. The resulting log$f(S_2)$ vs. log$f(O_2)$ pseudosection at the MnCa(F)S-C system shows that graphite is stable under fO_2 $<10^{-17}$ overall range of fS_2. Pyrrhotite is stable from 10^0 to 10^{-1} of fS_2, and pyrite occurs from the breakdown of pyrrhotite (under $fS_2 > 10^{-1}$). Pyrolusite occurs at high fO_2 fugacity close to 10^{-1}. Quartz and calcite occur in all fugacity fields (Fig. 17B).

5. Discussion

5.1. Paragenetic model

Our textural and mineralogical observations make it possible to construct a conceptual paragenetic model for the Lagoa do Riacho manganese deposit, involving the mineralogical composition of the manganese-rich rocks (OMO, SMO and garnetite) from diagenesis to metamorphism to supergene alteration (Fig. 18).

The earliest minerals formed in the proposed setting, in the sediment through diagenesis, would be the manganese carbonates (e.g., kutnohorite), which are found as inclusions in the core of spessartine and rhodonite. This is in line with the findings of Johnson et al (2016) and Polgári et al (2012). Furthermore, in unmetamorphosed manganese deposits, such as the Francevillian, Gabon, the earliest, diagenetic minerals are dominated by manganese carbonate phases (Leclerc and Weber, 1980; Gauthier-Lafaye and Weber, 2003; Beukes et al., 2016). Besides, these latter minerals, braunite (not identified here), abundant in low-grade manganese sequences as the Hotazel formation (Gutzmer and Beukes, 1995; Gutzmer and Beukes, 1996; Johnson et al., 2016) is also precipitated in the earliest stages. It grows through the reduction of Mn(IV) oxides in the presence of silica (Johnson et al., 2016). Likewise, manganese carbonate phases would be generated by reductive dissolution of manganese oxide and hydroxide particles plus organic matter at or below a redoxcline (Beukes et al., 2016; Johnson et al., 2016). Although lack direct evidence on these primary precipitates of manganese-oxyhydroxide minerals, the widespread graphite dissemination may suggest an early organic matter deposition. Thus, the graphite would be a remnant of organic carbon derived from bacterial biomass. Similarly, pyrite was formed via respiration of organic carbon linked to bacterial sulfate reduction. The other sulfide minerals (e.g., cobaltite and covellite) would have syngenetically precipitated with pyrite and graphite. Triple contacts, at approximately 120º found between cobaltite and surrounding matrix minerals, reinforce this statement since this feature suggests that the mineral either crystallized or recrystallized during metamorphism (Cabral et al., 2019b).

Quartz and feldspar are remnants of detrital components in an early sedimentary stage or also as part of pre-peak metamorphic assemblage together with spessartine. Some quartz does exist as late-stage veinlets and thus represents a late metamorphic stage. The metamorphic peak mineral assemblage is represented by garnet-rhodonite-tephroite-pyrophanite, here considered as a product of progressive regional metamorphism through decarbonation and dehydration reactions. Biotite found in the garnetite was developed during prograde metamorphism, while retrograde metamorphism led to the formation of mangano-cummingtonite. Some carbonate veinlets that replace rhodonite through fractures could be suggestive of a local hydrothermal process. At the end of the paragenetic sequence, manganese-oxyhydroxides (e.g., pyrolusite, cryptomelane) formed from either oxic surficial or subsurface fluid alteration.

5.2. Effects of metamorphism, metasomatism and other post-depositional processes on the manganese mineralogy

Metamorphism involves mineralogical transformations of isochemical nature, i.e., with no change in the bulk composition of the protolith, apart from loss of volatiles (Fyfe et al., 1978; Philpotts and Ague, 2009; Yardley, 2009; Putnis and Austrheim, 2010; Ague, 2017). This, of course, excludes both partial melting where there is substantial geochemical differentiation (Sawyer, 1994) or Na-Si-K metasomatism, which can also significantly alter the initial composition of a rock (Putnis and Austrheim, 2010). In such situations, due to the passage of fluids, there is the possibility of adding chemical components, some of which contain exogenous metals (e.g., Fe, Mn, Cu, Au, Pb, and Zn) (Audétat, 2019).

Most of our results are not compatible with fluids of this nature. Excluding a local occurrence of calcite veins that replaces rhodonite according to reaction (1), typical features developed by fluid-induced processes (eg., hydrothermal alteration), such as multiples veins and corresponding selvages are practically absent. Although the local presence of an intrusive granitic body has been documented, the chemical, textural and petrographic features from the manganese-rich rocks do not support their origin as hydrothermal. For example, the whole-rock geochemical profiles along the cores show a strong anti-covariance between SiO_2 and MnO (r^2= 0.72). Furthermore, high SiO_2 (up to 60 wt%) and K_2O (~ 9 wt%) coincides only with the input of a siliciclastic component (garnet quartzite).

$$MnSiO_{3\ (Rhodonite)} + CO_2 = MnCO_{3\ (Rhodochrosite)} + SiO_{2\ (Quartz)} \quad (1)$$

Additionally, garnet composition allows us to make inferences on the gains and losses of manganese during metamorphism and also monitor external fluid input into the system. For instance, manganese-rich garnet with weak chemical zoning in the Transvaal Supergroup was interpreted to have formed during a manganese-rich fluid flow event (Johnson et al., 2019). Our observations of irregular garnet chemical zoning in the OMO, SMO, and garnetite (Fig. 12 and Appendix B) indicates its growth from the fractionation between Ca-Mn-rich end members during progressive metamorphism. Calcium typically has a slow diffusion rate and is temporarily stored in the reactant carbonate during metamorphic garnet growth, leading to a Ca-depletion in the product (Willner et al., 2001). Conversely, the garnet chemical zoning pattern in typical open

systems, such as skarn deposits, is more complex than those described in our samples. In such settings, garnet commonly displays a distinct oscillatory zoning texture, which results from growth by fluid-rock interaction, providing an unequivocal evidence of hydrothermal alteration (Ciobanu and Cook, 2004; Park et al., 2017; Zhang et al., 2017). Besides that, in most cases garnet from these examples has grossular-andradite-rich end members, differing significantly from the spessartine-rich garnet presented here. This further suggests that no external fluids have been present during spessartine garnet growth. Therefore, we propose that spessartine garnet was formed at the expense of a manganese carbonate and an aluminous phase during a progressive metamorphic P-T path along reactions 2 and 3, according to Nyame (2001). Rhodonite shows a similar behavior to spessartine, with an irregular Ca-Mn exchange during its growth (Appendix B).

Thus, chemical and textural features support spessartine and rhodonite development by decarbonation and dehydration isochemical reactions during prograde regional metamorphism (reactions 2, 3, and 4). Regional metamorphism as the driving mechanism of the mineralogical changes is further supported by the large area of manganese-rich rocks occurring in the field. At a regional scale, these manganese sequences extend for at least 70 km in a linear belt of N-NE direction, precluding a local, hydrothermal mechanism of formation.

$3MnCO_3$ (Rhodochrosite or kutnohorite) + $Al_2Si_4O_{10}(OH)_2$ (Pyrophyllite) = $Mn_3Al_2(Si_3O_{12})$ (Spessartine) + SiO_2 (Quartz) + H_2O + $3CO_2$ (2)

$3MnCO_3$ (Rhodochrosite or kutnohorite) + SiO_2 (Quartz) + $Al_2Si_2O_5(OH)_4$ (Kaolinite) = $Mn_3Al_2(Si_3O_{12})$ (Spessartine) + $2H_2O$ + $3CO_2$ (3)

$MnCO_3$ (Rhodochrosite) + SiO_2 (Quartz) = $MnSiO_3$ (Rhodonite) + CO_2 (4)

Under minimum CO_2 molar fraction conditions (XCO_2 = 0.1%) and in an assemblage composed of rhodonite-diopside-spessartine-calcite, tephroite develops at the expense of rhodochrosite (reactions 5 and 6 below) under amphibolite facies metamorphic conditions (at least 575ºC, may reach 650ºC under intermediate XCO_2 0.4%), as observed in the pseudosection modeled for the SMO (Fig. 17). Although the equilibrium curve for tephroite formation occurs at

temperatures up to 120ºC higher than another modeling (e.g., Peters et al. 1973, Candia et al. 1975; Munteanu et al., 2004), it is compatible with the P-T metamorphism estimates for the graphite-bearing pelitic gneiss (700ºC) and the estimated temperatures for graphite (range 560-670ºC) in manganese-rich rocks.

$2MnCO_3$ (Rhodochrosite) + SiO_2 (Quartz) = Mn_2SiO_4 (Tephroite) + $2CO_2$ (5)

$Mn_3Al_2(Si_3O_{12})$ (Spessartine) + $CaMgSi_2O_6$ (Diopside) + $MnSiO_3$ (Rhodonite) + $CaCO_3$ (Calcite) + $MnCO_3$ (Rhodochrosite) = $Mn_3Al_2(Si_3O_{12})$ (Spessartine) + $CaMgSi_2O_6$ (Diopside) + $MnSiO_3$ (Rhodonite) + $CaCO_3$ (Calcite) + Mn_2SiO_4 (Tephroite) (6)

After peak metamorphism, retrograde processes likely took place as suggested by the presence of mangano-cummingtonite (Figs. 8, 9 and 11; Appendix B); this amphibole replaces diopside pyroxene (reaction 7). Although Dasgupta (1997) indicated this replacement to take place between 550-600ºC under P < 5kbar, our results suggest slightly lower temperatures (500-550ºC) for reaction (7):

$Mn_3Al_2(Si_3O_{12})$ (Spessartine) + $Mg_2Mg_5Si_8O_{22}(OH)_2$ (Cummingtonite) + SiO_2 (Quartz) + $CaCO_3$ (calcite) + $MnCO_3$ (Rhodochrosite) = $Mn_3Al_2(Si_3O_{12})$ (Spessartine) + $CaMgSi_2O_6$ (Diopside) + SiO_2 (Quartz) + $CaCO_3$ (Calcite) + Mn_2SiO_4 (Tephroite) (7)

During post-metamorphic processes, manganese-rich minerals were further modified by supergenesis (Jović, 1998) forming high-grade manganese ores (Roy, 2006; Beukes et al., 2016). Pyrolusite and cryptomelane are the main minerals developed at surface conditions. Besides field features typically formed in these settings, such as mangano-ferruginous duricrust, some silicates (e.g., rhodonite) are leached through micro fractures filled with manganese-oxyhydroxide. Such leaching would be related to alkaline and O_2-poor groundwater that mixed with O_2-rich meteoric waters allowing manganese-oxyhydroxides precipitation under supergene conditions (Dill et al., 2012, 2013). In the Ocr-4 core, higher MnO contents (close to 40 wt%) are detected in areas with high pyrolusite contents and low SiO_2 (10 wt%), reinforcing silicate leaching. The analyzed pyrolusite crystals (Appendix B) similarly show a negative correlation with SiO_2 (Fig. 15) and

accordingly the X-ray maps (Fig. 13) show pyrolusite with low SiO_2 content. The enrichment in BaO, K_2O, and Na_2O (Appendix B) in these minerals (e.g., pyrolusite) supports alkaline low-temperature oxidizing water percolation in their formation. The physicochemical oxidizing conditions of surface waters required for pyrolusite precipitation, for example, was modeled (fO_2 *vs*. fS_2) for the SMO, being compatible with oxic environments (fO_2 of 10^0). It is also possible to observe that pyrolusite was formed by the breakdown of rhodonite, as observed texturally, through reaction (8):

$$Mn_2SiO_{4\ (Tephroite)} + MnSiO_{3\ (Rhodonite)} + SiO_{2\ (Quartz)} + (Mn,Ca)CO_{3\ (carbonate)} = Mn_2SiO_{4\ (Tephroite)} + MnO_{2\ (Pyrolusite)} + SiO_{2\ (Quartz)} + (Mn,Ca)CO_{3\ (Carbonate)} \quad (8)$$

A metamorphic origin, along a progressive metamorphic P-T path for the manganese minerals at the Lagoa do Riacho manganese deposit, is proposed. On the other hand, in other Brazilian manganese deposits, alternative hypotheses exist (e.g., Park et al., 1951; Rodrigues et al.2019a, 2019b). In such environments, similar manganese-bearing minerals (e.g., spessartine, rhodonite tephroite) may have developed by contact metamorphism followed by hydrothermal alteration, suggesting an epigenetic rather than syngenetic genesis.

5.3. Paleoenvironmental constraints: Textural features and mineral assemblages as proxies for protolith nature

Finely banded metamorphic rocks, rich in manganese (OMO), with common intercalations of garnet quartzite and graphite-bearing pelitic gneiss, indicate a sedimentary protolith. Specifically, the continuous foliation defined by internal segregations between spessartine-rich and quartz-feldspathic layers suggests the existence of a metamorphic foliation parallel to the primary sedimentary bed ($S_n//S_0$). Moreover, spessartine garnet requires, for its formation, the existence of a protolith with a notable aluminous contribution (e.g., mudstones; Dasgupta et al., 1990; Nyame, 2001). In this sense, millimetric to centimetric intercalations between pelitic and psammitic layers can be interpreted as interlaminations of clays and sands, respectively, in the protolith, common in a range of marine depositional settings, from deep to shallow deposits (Pickering et al., 1986; Mutti et al., 2009). However, and in agreement with Nyame (2001), an aluminous composition alone would not explain the formation of spessartine in large quantities,

such as in the OMO, and mainly garnetite. According to this same author, we highlight reactions (2) and (3) as plausible mechanisms to produce spessartine garnet.

Notably, the spessartine garnet, especially in the OMO, has kutnohorite-type ($CaMn(CO_3)_2$) inclusions in its core, which directly indicates its origin at the expense of the consumption of a manganese-bearing carbonate phase. Other studies in manganese-rich successions have also documented the presence of spessartine garnet porphyroblasts with a manganese-carbonate inclusion-rich core (De Putter et al., 2018; Chisonga et al., 2012; Cabral et al., 2019b; Mücke et al., 1999; Mancini et al., 2000; Slack et al., 2000). As for the aluminous phase, the pseudosection approach (T-XCO_2) shows that under low-grade metamorphic conditions (400ºC and 0.2-0.9 XCO_2), the aluminous phase consumed to form spessartine is kaolinite and pyrophyllite (white mica).

Mineral assemblages involving rhodonite can also account for a mixed (pelitic-carbonatic) origin for these rocks since they form at the expense of rhodochrosite (Roy, 1981). Decarbonation reactions, according to reaction (4), are commonly necessary to form these minerals. Reaction (4) is reinforced by the presence of carbonate inclusions in some analyzed rhodonite (e.g., SMO; sample 10046). However, unlike the OMO and garnetite, the SMO has a relatively minor amount of spessartine garnet, which would reflect low amounts of aluminum in the protolith composition. Therefore, the protolith of the OMO and garnetite may be muddy marls, while the SMO, because it has a relatively lower aluminous contribution and a higher amount of quartz-feldspar, may be related to silty marls. Marl protoliths spatially related to manganese rocks are usually associated with organic matter-rich sedimentary environments (e.g., Polgari et al., 2012; Scholz et al., 2018; Biondi and Lopez., 2019; Ostrander et al., 2019; Yu et al., 2019; Biondi et al., 2020).

Based on the widespread dissemination of graphite in the manganese-rich rocks, and their host rocks, we speculate that graphite formed as a result of organic matter conversion during metamorphism and/or as a precipitate from a C-O-H fluid (e.g., Huizenga, 2011; Luque et al., 2012; Bernard and Papineau, 2014). First, considering that there is a direct correlation between the peak metamorphic temperatures of graphite crystals (up to 675°C) and that of the graphite-bearing pelitic gneiss (~700°C), it is unlikely that graphite was introduced late, by metasomatism/ hydrothermal alteration, for instance. A similar approach was used by Tashiro et al. (2017) as evidence of early traces of life in high grade metamorphosed graphite-rich sequences in the Archean Saglek Block, Labrador. Second, graphite in the present study occurs as flakes distributed

along the foliation within the crystalline rock matrix, without any relationship with cross-cutting veins and other filling textures. Third, graphite from this same graphite-bearing paragneiss unit (Canindé do Ceará Complex) displays $\delta^{13}C$ values between -30 and -20‰, which suggest a biogenic origin for the carbonaceous matter (Fragomeni and Pereira, 2013). Thus, all these constraints agree to Bernard and Papineau (2014) suggested criteria for assigning a biogenic origin to graphitic carbon.

Preservation of organic matter-rich accumulations in the sedimentary environment requires rapid burial into anoxic sediments for its preservation (Calvert et al., 1996). Several textural features described above point to a reducing environment. All described sulfide minerals (e.g., pyrite), for instance, are strictly related to graphite, and this association reflects its crystallization under fO_2 of 10^{-17}. In this regard, the most likely mechanism was bacterial sulfate reduction, where porewater sulfate served as an electron acceptor and organic carbon as the primary electron donor (e.g., Boesen and Postma, 1988). The textural relationship in which pyrite occurs parallel to the foliation in elongated crystals, and metamorphic equilibrium (fO_2 vs. fS_2) between pyrite and graphite, correlate well with this assumption. The occurrence of other sulfide minerals with redox-sensitive metals, such as cobaltite (Co) and covellite (Cu), as well as the whole-rock P_2O_5 content (0.05-0.3 wt%; Appendix C), also point to a reducing environment (Maynard, 2010). In this scenario, the precipitation of these minerals was most probably related to redox-sensitive trace metals (eg., Co and Cu) scavenging during organic matter settling (Tribovillard et al., 2006; Planavsky et al., 2018).

Additionally, the metal enrichment and previous reported fO_2 conditions (10^{-18} to 10^{-25}) are also supported by the presence of pyrophanite that requires a Mn-Ti-rich precursor under low fO_2 (Nayak and Mohapatra, 1998; Velilla and Jiménez-Millán 2003). Within this general context, we outline an initial environment involving the deposition of anoxic sediments (eg., organic matter-rich manganese marl, black shales, and wackes) on the seafloor (Fig. 19A). Such scenario may exist in redox-stratified basins, such as the Baltic Sea, where a redoxcline separates deep anoxic/euxinic waters from shallow oxic waters (Huckriede and Meischner, 1996). During transgressive phases, manganese oxides earlier settled above the oxic-anoxic interface would then be reduced, shifting to the anoxic bottom sediments, re-precipitating as manganese carbonates over the sedimentary pile (Calvert and Pedersen, 1996; Roy, 2006). Manganese oxide's reductive dissolution is also used to explain the manganese-carbonate-rich strata in the Paleoproterozoic

Francevillian basin (Okita et al., 1988; Maynard et al., 2010; Beukes et al., 2016; Mayika et al., 2020).

The metamorphism previously discussed would be responsible for the physicochemical transformation of the sedimentary protoliths into manganese-rich rocks (OMO, SMO, and garnetite), graphite-bearing pelitic gneiss and garnet quartzite, respectively (Figure 19B).

5.4. Similarities with other manganese-rich successions

In general, the field relationships and the mineralogical changes that the protoliths of the studied manganese-rich rocks experienced, reaching the metamorphic peak in the upper amphibolite facies, are compatible with South American and West African Paleoproterozoic history (Alkmim and Marshak, 1998; Feybesse et al. 2006; Rosa-Costa et al., 2006; Vasquez et al. 2008; Baratoux et al., 2011; Brito Neves., 2011; Teixeira et al., 2017). Between 2250-2100 Ma, during the Transamazonian/Eburnean accretionary orogeny, fragments from north and northeast Brazil were connected to the West African Craton (Klein and Moura, 2008; Neves, 2011; Costa et al., 2018; Grenholm, 2019; Grenholm et al., 2019). This orogeny was a promising candidate to trigger the high-grade metamorphism imprinted in these rock fragments. As a consequence of this process, other Paleoproterozoic manganese-rich rocks from South America and West Africa share some similar features to the Brazilian rocks in terms of mineral assemblage and metamorphic grade (e.g., Mücke et al., 1999; Chisonga et al., 2012; Borges et al., 2015; Cabral et al., 2019a; Rodrigues et al., 2019a, b; Salgado et al., 2019). In this setting, the best correlation maybe with the Serra do Navio manganese deposit in the Amazonian Craton (Chisonga et al., 2012) and the manganese ores at Morro da Mina, in the southern Quadrilátero Ferrífero (Cabral et al., 2019a). In these, manganese ores composed of spessartine, rhodonite, tephroite, and rhodochrosite are hosted by graphitic gneiss, manganese carbonate rocks, garnet-bearing quartzite, and cummingtonite-biotite schists, metamorphosed under amphibolite facies conditions (Scarpelli, 1968; Rodrigues et al., 1986, Chisonga et al., 2012; Cabral et al., 2019a), which strongly resemble the manganese-rich Lagoa do Riacho rocks presented here. Additionally, this paragenetic association is close to that of similar-aged manganese chemical sediments of the Nsuta manganese field from the Birimian, West African (N-NE Brazil counterpart) succession (Mücke et al., 1999). The mineralogical associations from Otjosondu ferromanganese deposit in the Neoproterozoic Damara Supergroup (Cabral et al., 2011) are also similar to those described in our study. Interestingly, the protolith of

all these manganese-rich sequences has chemical nature and is associated with siliciclastic rocks, including black shales (Mücke et al., 1999; Chisonga et al., 2012; Cabral et al., 2019a; Roy, 2006), such as in the Lagoa do Riacho manganese deposit.

Contrasting with previous examples, useful unmetamorphosed and undeformed analogs of black-shale hosted manganese deposits would be those from the Paleoproterozoic Franceville basin (Leclerc and Weber, 1980; Gauthier-Lafaye and Weber, 2003; Beukes et al., 2016). These are interbedded with black shales, siltstones, sandstones and dolomite deposited in deltaic to marine depositional systems (Gauthier-Lafaye and Weber, 2003; Ossa Ossa et al., 2018). The well-preserved Francevillian sedimentary protoliths would be examples of likely precursors for the Lagoa do Riacho metamorphic protoliths in northeastern Brazil. For example, the presence of the garnet-quartzite (sandstone remnant) and the graphite-bearing pelitic gneiss (black shale remnant) closely related to manganese-rich rocks (Fig. 19B) reinforces this point of view. Additionally, the origin of these black shales from the Franceville Basin may be correlated to a global, large-scale organic carbon burial event that took place in the Great Oxidation Event aftermath, during the so-called Lomagundi-Jatuli event at ca. 2.2-2.0 Ga. (Karhu and Holland, 1996; Kump et al., 2011; Canfield et al., 2013; Ossa Ossa et al., 2018; Mayika et al., 2020). In the Morro da Mina manganese deposit, southern Quadrilátero Ferrífero, Cabral et al. (2019a) correlated this sequence to the Lomagundi-Jatuli event based on the genetic relationship between manganesiferous and organic-rich rocks deposited at 2.07–1.86 Ga. In a similar approach, considering the sedimentation age for the metasedimentary rocks from the Canindé do Ceará Complex (host to manganese-rich rocks) roughly at 2.1-1.9 Ga., it is possible that the deposition of the manganese-rich succession from northern Borborema Province and their graphite-bearing sedimentary rocks also coincided with the global event of organic matter accumulation (Kump et al., 2011; Canfield et al., 2013), according to the geochronological constraints from Fetter et al (2000), Gomes (2013), Garcia et al. (2014); Costa and Palheta (2017) and Calado et al. (2019).

6. Conclusions

The relationship between detailed petrography, mineral chemistry and whole-rock geochemistry, allied to the estimation of physical-chemical conditions, allowed us to trace the protolith nature of the metamorphosed manganese-rich sequences at the Lagoa do Riacho manganese deposit in the northern Borborema Province. Our results indicate that the manganese-

rich rocks and their host rocks were generated in a sedimentary context, possibly in a marine setting with carbonate and organic matter contribution. The organic matter contribution was supported by the lithological associations, chemical-textural relations, and matching of the temperatures of the manganese ore host rock with that obtained by the graphite crystals. Estimate for the deposition of these rocks in an anoxic/euxinic scenario was also measured based on graphite-pyrite assemblage, in addition to thermodynamic modeling using whole-rock geochemistry.

The data presented show that the sedimentary association that hosts the manganese ore was subjected to metamorphic conditions reaching the upper amphibolite facies. Assemblages typically formed by spessartine, rhodonite and tephroite reinforce these estimates. The transformations are isochemical, and most compositional changes are balanced by cation exchange between reagents and products. Additionally, post-metamorphic changes related to the supergene enrichment of these manganese-rich minerals are evidenced by the presence of late oxides and hydroxides (e.g., pyrolusite, cryptomelane).

Although the studied manganese-rich sedimentary association from the north of the Borborema Province show similarities to manganese deposits in the Amazonian Craton, Quadrilátero Ferrífero (both in Brazil) and Birimian Succession regarding field association, mineral assemblages, metamorphic grade, and age of the host-rocks, more specific studies on the ore-bearing minerals (mainly isotopic) are required in order to have more precise correlations between the depositional paleoenvironment of these manganese-rich sequences.

Acknowledgments

The first author is grateful to the Federal University of Western Pará (UFOPA) for support throughout the time, and to the Geologist Renato Braz Sue (on behalf of Libra Ligas do Brasil company) for providing full access to drill cores, whole-rock geochemical analyses from Lagoa do Riacho manganese deposit and fieldwork assistance. Authors thank the Microscopy and Microanalysis Laboratory (LMic) of the Federal University of Ouro Preto, a member of the Microscopy and Microanalysis Network of Minas Gerais State/Brazil/FAPEMIG. João Gabriel Motta, Abimbola Ogunyele, Robert Muniz and Giorgio Basilici are also acknowledged for their valuable comments on the initial draft of this paper. We truly appreciate the comments, suggestions and criticisms of the Associate Editor Professor Lydia Lobato, Bertus Smith and an anonymous reviewer that helped improve the quality of this manuscript. Furthermore, we thank the editorial

handling by Professor Huayong Chen. WSA also acknowledges the Brazilian National Research Council (CNPq) for research grant (process. 305263/2020-0). This research is part of the first author's Ph.D. thesis.

References

Ague, J.J., 2017. Element mobility during regional metamorphism in crustal and subduction zone environments with a focus on the rare earth elements (REE). Am. Mineral. 102, 1796–1821. https://doi.org/10.2138/am-2017-6130

Alkmim, F.F., Marshak, S., 1998. Transamazonian Orogeny in the Southern São Francisco Craton Region, Minas Gerais, Brazil: Evidence for Paleoproterozoic collision and collapse in the Quadrilátero Ferrífero. Precambrian Res. 90, 29–58. https://doi.org/10.1016/s0301-9268(98)00032-1

Audétat, A., 2019. The metal content of magmatic-hydrothermal fluids and its relationship to mineralization potential. Econ. Geol. 114, 1033–1056. https://doi.org/10.5382/econgeo.4673

Baratoux, L., Metelka, V., Naba, S., Jessell, M.W., Grégoire, M., Ganne, J., 2011. Juvenile Paleoproterozoic crust evolution during the Eburnean orogeny (~2.2-2.0Ga), western Burkina Faso. Precambrian Res. 191, 18–45. https://doi.org/10.1016/j.precamres.2011.08.010

Bartoli, O., Tajčmanová, L., Cesare, B., Acosta-Vigil, A., 2013. Phase equilibria constraints on melting of stromatic migmatites from Ronda (S. Spain): Insights on the formation of peritectic garnet. J. Metamorph. Geol. 31, 775–789. https://doi.org/10.1111/jmg.12044

Barzoi, S.C., 2015. Shear stress in the graphitization of carbonaceous matter during the low-grade metamorphism from the northern Parang Mountains (South Carpathians) - Implications to graphite geothermometry. Int. J. Coal Geol. 146, 179–187. https://doi.org/10.1016/j.coal.2015.05.008

Bernard, S., Papineau, D., 2014. Graphitic carbons and biosignatures. Elements 10, 435–440. https://doi.org/10.2113/gselements.10.6.435

Berni, G. V., Heinrich, C.A., Wälle, M., Wall, V.J., 2019. Fluid geochemistry of the Serra Pelada Au-Pd-Pt deposit, Carajás, Brazil: Exceptional metal enrichment caused by deep reaching hydrothermal oxidation. Ore Geol. Rev. 111, 102991. https://doi.org/10.1016/j.oregeorev.2019.102991

Beukes, N.J., Swindell, E.P.W., Wabo, H., 2016. Manganese deposits of Africa. Episodes 39, 285–317. https://doi.org/10.18814/epiiugs/2016/v39i2/95779

Beyssac, O., Goffé, B., Chopin, C., Rouzaud, J.N., 2002. Raman spectra of carbonaceous material in metasediments: A new geothermometer. J. Metamorph. Geol. 20, 859–871. https://doi.org/10.1046/j.1525-1314.2002.00408.x

Biondi, J.C., Lopez, M., 2017. Urucum Neoproterozoic–Cambrian manganese deposits (MS, Brazil): Biogenic participation in the ore genesis, geology, geochemistry, and depositional environment. Ore Geol. Rev. 91, 335–386. https://doi.org/10.1016/j.oregeorev.2017.09.018

Biondi, J.C., Polgári, M., Gyollai, I., Fintor, K., Kovács, I., Fekete, J., Mojzsis, S.J., 2020. Biogenesis of the Neoproterozoic kremydilite manganese ores from Urucum (Brazil) – A new manganese ore type. Precambrian Res. 340. https://doi.org/10.1016/j.precamres.2020.105624

Boesen, C., Postma, D., 1988. Pyrite formation in anoxic environments of the Baltic. Am. J. Sci. https://doi.org/10.2475/ajs.288.6.575

Borges, O. J., Cruz, S.C.P., Barbosa, J.S.F., Da Silva Santos, E., 2015. Structural framework of rocks of the Lagoa D'anta mine area, iron-manganese Urandi-Caetité-Licínio de Almeida District, Bahia, Brasil. Brazilian J. Geol. 45, 173–192. https://doi.org/10.1590/2317488920150002002

Brito Neves, B.B., Santos, E.J., and Van Schmus, W.R., 2000, in Tectonic History of the Borborema Province, Northeast Brazil, Cordani, U.G., Milani, E.J., Thomaz Filho, A., and Campos, D.A., Eds., Tectonic Evolution of South America, Rio de Janeiro, 31st International Geological Congress, p. 151–182.

Brito Neves, B.B., 2011. The Paleoproterozoic in the South-American continent: Diversity in the geologic time. J. South Am. Earth Sci. 32, 270–286. https://doi.org/10.1016/j.jsames.2011.02.004

Brown, P.E., Essene, E.J., Peacor, D.R., 1980. Phase relations inferred from field data for mn pyroxenes and pyroxenoids. Contrib. to Mineral. Petrol. 74, 417–425. https://doi.org/10.1007/BF00518121

Brusnitsyn, A.I., Starikova, E. V., Zhukov, I.G., 2017. Mineralogy of low grade metamorphosed manganese sediments of the Urals: Petrological and geological applications. Ore Geol. Rev. 85, 140–152. https://doi.org/10.1016/j.oregeorev.2016.07.004

Cabral, A.R., Moore, J.M., Mapani, B.S., Koubová, M., Sattler, C.D., 2011. Geochemical and mineralogical constraints on the genesis of the Otjosondu ferromanganese deposit, Namibia: Hydrothermal exhalative versus hydrogenetic (including snowball-Earth) origins. South African J. Geol. 114, 57–76. https://doi.org/10.2113/gssajg.114.1.57

Cabral, A.R., Zeh, A., Vianna, N.C., Ackerman, L., Pašava, J., Lehmann, B., Chrastný, V., 2019a. Molybdenum-isotope signals and cerium anomalies in Palaeoproterozoic manganese ore survive high-grade metamorphism. Sci. Rep. 9, 1–7. https://doi.org/10.1038/s41598-019-40998-5

Cabral, A.R., Zeh, A., Viana, N.C. da S., de Castro, M.P., Laufek, F., Lehmann, B., Queiroga, G., 2019b. Alabandite (MnS) in metamorphosed manganiferous rocks at Morro da Mina, Brazil: palaeoenvironmental significance. Eur. J. Mineral. 31, 973–982. https://doi.org/10.1127/ejm/2019/0031-2879

Caby, R., 1989. Precambrian terranes of the Benin-Nigeria and Northeast Brazil and the late Proterozoic South Atlantic fit: Geological Society of America Special Paper, v. 230, p. 145–158.

Calado, B.O., Costa, F.G., Gomes, I.P., Rodrigues, J.B., 2019. Evidence for ca. 2046 Ma high-grade metamorphism in Paleoproterozoic metasedimentary rocks of the northern Borborema Province, NE Brazil: constraints from U-Pb (LA-ICP-MS) zircon ages. Journal of the Geological Survey of Brazil, 2(3), 137-150. https://doi.org/10.29396/jgsb.2019.v2.n3.1

Calvert, S.E., Pedersen, T.F., 1996. Sedimentary geochemistry of manganese: Implications for the environment of formation of manganiferous black shales. Econ. Geol. 91, 36–47. https://doi.org/10.2113/gsecongeo.91.1.36

Calvert, S.E., Bustin, R.M., Ingall, E.D., 1996. Influence of water column anoxia and sediment supply on the burial and preservation of organic carbon in marine shales. Geochim. Cosmochim. Acta 60, 1577–1593. https://doi.org/10.1016/0016-7037(96)00041-5

Candia, M.A.F., Peters, T., Valarelli, J. V, Mineralogia, D., Paulo, S., 1975. The Experimental Investigation o f the Reactions MnCO3 + SiO2 = MnSiO3 + CO2 and MnSiO3 + MnCO3 = Mn2SiO4 + CO2 in CO2/H2O Gasmixtures at a Total Pressure of 500 Bars. Contrib. to Mineral. Petrol. 52, 261–266.

Canfield, D.E., Ngombi-Pemba, L., Hammarlund, E.U., Bengtson, S., Chaussidon, M., Gauthier-Lafaye, F., Meunier, A., Riboulleau, A., Rollion-Bard, C., Rouxel, O., Asael, D., Pierson-Wickmann, A.C., El Albani, A., 2013. Oxygen dynamics in the aftermath of the Great Oxidation of Earth's atmosphere. Proc. Natl. Acad. Sci. U. S. A. 110, 16736–16741. https://doi.org/10.1073/pnas.1315570110

Castaing, C., Feybesse, J.L., Thiéblemont, D., Triboulet, C., Chèvremont, P., 1994. Palaeogeographical reconstructions of the Pan-African/Brasiliano orogen: closure of an oceanic domain or intracontinental convergence between major blocks? Precambrian Res. 69, 327–344. https://doi.org/10.1016/0301-9268(94)90095-7

Castro, N.A., 2004. Evolução Geológica Proterozoica da Região entre Madalena e Taperuaba, Domínio Tectônico Ceará Central (Província Borborema). PhD Thesis. Instituto de Geociências, USP, Sao Paulo-SP, p. 221.

Chisonga, B.C., Gutzmer, J., Beukes, N.J., Huizenga, J.M., 2012. Nature and origin of the protolith succession to the Paleoproterozoic Serra do Navio manganese deposit, Amapa Province, Brazil. Ore Geol. Rev. 47, 59–76. https://doi.org/10.1016/j.oregeorev.2011.06.006

Ciobanu, C.L., Cook, N.J., 2004. Skarn textures and a case study: The Ocna de Fier-Dognecea orefield, Banat, Romania. Ore Geol. Rev. 24, 315–370. https://doi.org/10.1016/j.oregeorev.2003.04.002

Connolly, J.A.D., Cesare, B., 1993. C-O-H-S fluid composition and oxygen fugacity in graphitic metapelites. J. Metamorph. Geol. 11, 379–388. https://doi.org/10.1111/j.1525-1314.1993.tb00155.x

Connolly, J.A.D., 2005. Computation of phase equilibria by linear programming: A tool for geodynamic modeling and its application to subduction zone decarbonation. Earth Planet. Sci. Lett. 236, 524–541. https://doi.org/10.1016/j.epsl.2005.04.033

Cordani, U.G., Ramos, V.A., Fraga, L.M., Cegarra, M.,Delgado, I., de Souza, K.G., Gomes, F.E.M., Schobbenhaus, C., 2016. Tectonic map of South America, 2th: Commission for the geological map of the world, scale 1:5.000.000, 1 sheet.

Costa, F.G., Palheta, E.S. de M., Rodrigues, J.B., Gomes, I.P., Vasconcelos, A.M., 2015. Geochemistry and U-Pb zircon ages of plutonic rocks from the Algodões granite-greenstone terrane, Troia Massif, northern Borborema Province, Brazil: Implications for Paleoproterozoic subduction-accretion processes. J. South Am. Earth Sci. 59, 45–68. https://doi.org/10.1016/j.jsames.2015.01.007

Costa F.G., Palheta E. 2017. Geologia e recursos minerais das folhas Quixadá (SB.24-V-B-IV) e Itapiúna (SB.24-X-A-IV). Escala 1:100.000. Fortaleza, CPRM. Available on line at: http://rigeo.cprm.gov.br/jspui/handle/doc/19029/

Costa, F.G., Klein, E.L., Lafon, J.M., Milhomem Neto, J.M., Galarza, M.A., Rodrigues, J.B., Naleto, J.L.C., Corrêa Lima, R.G., 2018. Geochemistry and U–Pb–Hf zircon data for plutonic rocks of the Troia Massif, Borborema Province, NE Brazil: Evidence for reworking of Archean and juvenile Paleoproterozoic crust during Rhyacian accretionary and collisional tectonics. Precambrian Res. 311, 167–194. https://doi.org/10.1016/j.precamres.2018.04.008

Costa, F.G., Klein, E.L., Harris, C., Roopnarain, S., 2019. Fluid inclusion and stable isotope (O, H, C) constraints on the genesis of the Pedra Branca gold deposit, Troia Massif, Borborema Province, NE Brazil: An example of hypozonal orogenic gold mineralization. Ore Geol. Rev. 107, 476–500. https://doi.org/10.1016/j.oregeorev.2019.03.007

Dantas, E.L., De Souza, Z.S., Wernick, E., Hackspacher, P.C., Martin, H., Xiaodong, D., Li, J.W., 2013. Crustal growth in the 3.4-2.7Ga São José de Campestre Massif, Borborema Province, NE Brazil. Precambrian Res. 227, 120–156. https://doi.org/10.1016/j.precamres.2012.08.006

Dasgupta, S., Banerjee, H., Fukuoka, M., Bhattacharya, P.K., Roy, S., 1990. Petrogenesis of metemorphosed manganese deposits and the nature of the precursor sediments. Ore Geol. Rev. 5, 359–384. https://doi.org/10.1016/0169-1368(90)90039-P

Dasgupta, S., Sengupta, P., Fukuoka, M., Roy, S., 1993. Contrasting parageneses in the manganese silicate-carbonate rocks from Parseoni, Sausar Group, India and their interpretation. Contrib. to Mineral. Petrol. 114, 533–538. https://doi.org/10.1007/BF00321757

Dasgupta, S., 1997. P-T-X relationships during metamorphism of manganese-rich sediments: Current status and future studies. Geol. Soc. Spec. Publ. 119, 327–337. https://doi.org/10.1144/GSL.SP.1997.119.01.21

Deer W.A., Howie R.A., Zussman J. 1992. Rock-forming minerals. London, 2a ed., Longmans, 696 p.

De Putter, T., Liégeois, J.P., Dewaele, S., Cailteux, J., Boyce, A., Mees, F., 2018. Paleoproterozoic manganese and base metals deposits at Kisenge-Kamata (Katanga, D.R. Congo). Ore Geol. Rev. 96, 181–200. https://doi.org/10.1016/j.oregeorev.2018.04.015

De Wit, M.J., Brito Neves, B.B., Trouw, R.A.J., and Pankhurst, R. J., editors, 2008, West Gondwana: Pre-Cenozoic Correlations across the Atlantic Region, Volume 294: Geological Society of London, Special Publication, p. 1–8.

Dill, H.G., Wemmer, K., 2012. Origin and K/Ar age of cryptomelane-bearing Sn placers on silcretes, SE Germany. Sediment. Geol. 275–276, 70–78. https://doi.org/10.1016/j.sedgeo.2012.07.016

Dill, H.G., Pöllmann, H., Techmer, A., 2013. 500Million years of rift- and unconformity-related Mn mineralization in the Middle East: A geodynamic and sequence stratigraphical approach to the recycling of Mn. Ore Geol. Rev. 53, 112–133. https://doi.org/10.1016/j.oregeorev.2013.01.004

Fetter, A.H., 1999. U-Pb and Sm-Nd geochronological constraints on the crustal framework and geologic history of Ceará State, NW Borborema Province, NE Brazil: Implications for the assembly of Gondwana. Ph.D. Thesis, Kansas.

Fetter, A.H., Van Schmus, W.R., Santos, T.J.S., Nogueira Neto, J.A., Arthaud, M.H., 2000. U-Pb and Sm-Nd Geochronological Constraints on the Crustal Evolution and Basement Architecture of Ceará State, Nw Borborema Province, Ne Brazil: Implications for the Existence of the Paleoproterozoic Supercontinent "Atlantica." Rev. Bras. Geociências 30, 102–106. https://doi.org/10.25249/0375-7536.2000301102106

Feybesse, J.L., Billa, M., Guerrot, C., Duguey, E., Lescuyer, J.L., Milesi, J.P., Bouchot, V., 2006. The paleoproterozoic Ghanaian province: Geodynamic model and ore controls, including regional stress modeling. Precambrian Res. 149, 149–196. https://doi.org/10.1016/j.precamres.2006.06.003

Fragomeni, P.R.P., Pereira, R.M., 2013. The graphite mineralization in the Aracoiába-Baturité District (CE): Geotectonic and metallogenetic implications. Brazilian J. Geol. 43, 223–234. https://doi.org/10.5327/Z2317-48892013000200003

Fuhrman, M.L., Lindsley, D.H., 1988. Ternary-feldspar modeling and thermometry. Am. Mineral. 73, 201–215.

Ganade, C.E., Basei, M.A.S., Costa, F.G., Armstrong, R., Brito, R.S., 2017. Contrasting Archaean (2.85–2.68 Ga) TTGs from the Tróia Massif (NE-Brazil) and their geodynamic implications for flat to steep subduction transition. Precambrian Res. 297, 1–18. https://doi.org/10.1016/j.precamres.2017.05.007

Garcia M., Santos T., Amaral W. 2014. Provenance and tectonic setting of neoproterozoic supracrustal rocks from the Ceará Central Domain, Borborema Province NE Brazil: constraints from geochemistry and detrital zircon ages. Int. Geol. Rev. 56 (4), 1-20. https:// doi.org/10.1080/00206814.2013.875489

Gauthier-Lafaye, F., Weber, F., 2003. Natural nuclear fission reactors: time constraints for occurrence, and their relation to uranium and manganese deposits and to the evolution of the atmosphere. Precambrian Res.120, 81–100.

Gutzmer, J. and Beukes, N.J. (1995). Fault-controlled metasomatic alteration of Early Proterozoic sedimentary manganese ores in the Kalahari Manganese Field, South Africa.Economic Geology, 90, 823-844.

Gutzmer, J. and Beukes, N.J. (1996). Mineral paragenesis of the Kalahari Manganese Field, South Africa. Ore Geology Reviews, 11, 405-428.

Fyfe, W.S., Price, N.J., Thompson, A.B., 1978. Fluids in the Earth's Crust. Elsevier, New York, 383 pp.

Gomes E.N. 2013. Protominérios e minérios de manganês de Juá-CE. MSc Dissertation, Instituto de Geociências, Universidade Federal do Ceará, Ceará, 102 p.

Grenholm, M., 2019. The global tectonic context of the ca. 2.27-1.96 Ga Birimian Orogen – Insights from comparative studies, with implications for supercontinent cycles. Earth-Science Rev. 193, 260–298. https://doi.org/10.1016/j.earscirev.2019.04.017

Grenholm, M., Jessell, M., Thébaud, N., 2019. Paleoproterozoic volcano-sedimentary series in the ca. 2.27–1.96 Ga Birimian Orogen of the southeastern West African Craton. Precambrian Res. 328, 161–192. https://doi.org/10.1016/j.precamres.2019.04.005

Holland, H.D., 2006. The oxygenation of the atmosphere and oceans. Philos. Trans. R. Soc. B Biol. Sci. 361, 903–915. https://doi.org/10.1098/rstb.2006.1838

Holland, T., Powell, R., 1991. A Compensated-Redlich-Kwong (CORK) equation for volumes and fugacities of CO_2 and H_2O in the range 1 bar to 50 kbar and 100-1600°C. Contrib. to Mineral. Petrol. 109, 265–273. https://doi.org/10.1007/BF00306484

Holland, T.J.B., Powell, R., 1998. An internally consistent thermodynamic data set for phases of petrological interest. J. Metamorph. Geol. 16, 309–343. https://doi.org/10.1111/j.1525-1314.1998.00140.x

Holland, T.J.B., Powell, R., 2004. An internally consistent thermodynamic data set for phases of petrological interest. J. Metamorph. Geol. 16, 309–343. https://doi.org/10.1111/j.1525-1314.1998.00140.x

Holland, T.J.B., Powell, R., 2011. An improved and extended internally consistent thermodynamic dataset for phases of petrological interest, involving a new equation of state for solids. J. Metamorph. Geol. 29, 333–383. https://doi.org/10.1111/j.1525-1314.2010.00923.x

Hollanda, M.H.B.M., Archanjo, C.J., Souza, L.C., Dunyi, L., Armstrong, R., 2011. Long-lived Paleoproterozoic granitic magmatism in the Seridó-Jaguaribe domain, Borborema Province-NE Brazil. J. South Am. Earth Sci. 32, 287–300. https://doi.org/10.1016/j.jsames.2011.02.008

Huckriede, H., Meischner, D., 1996. Origin and environment of manganese-rich sediments within black-shale basins. Geochim. Cosmochim. Acta 60, 1399–1413. https://doi.org/10.1016/0016-7037(96)00008-7

Huizenga, J.M., 2011. Thermodynamic modelling of a cooling C-O-H fluid-graphite system: Implications for hydrothermal graphite precipitation. Miner. Depos. 46, 23–33. https://doi.org/10.1007/s00126-010-0310-y

Johnson, J.E., Webb, S.M., Ma, C., Fischer, W.W., 2016. Manganese mineralogy and diagenesis in the sedimentary rock record. Geochim. Cosmochim. Acta 173, 210–231. https://doi.org/10.1016/j.gca.2015.10.027

Johnson, J.E., Webb, S.M., Condit, C.B., Beukes, N.J., Fischer, W.W., 2019. Effects of metamorphism and metasomatism on manganese mineralogy: Examples from the transvaal supergroup. South African J. Geol. 122, 489–504. https://doi.org/10.25131/sajg.122.0034

Jović, V., 1998. Supergene, in: Geochemistry. Springer Netherlands, Dordrecht, pp. 615–616. https://doi.org/10.1007/1-4020-4496-8_310

Karhu, J.A., Holland, H.D., 1996. Carbon isotopes and the rise of atmospheric oxygen. Geology 24, 867–870. https://doi.org/10.1130/0091-7613(1996)024<0867:CIATRO>2.3.CO;2

Kirilova, M., Toy, V., Rooney, J.S., Giorgetti, C., Gordon, K.C., Collettini, C., Takeshita, T., 2018. Structural disorder of graphite and implications for graphite thermometry. Solid Earth 9, 223–231. https://doi.org/10.5194/se-9-223-2018

Klein, C., Dutrow, B. 2007. Manual of Mineral Science. 23rd Edition. Wiley.

Klein, E.L., Moura, C.A.V., 2008. São Luís Craton and Gurupi belt (Brazil): Possible links with the West African Craton and surrounding Pan-African belts. Geol. Soc. Spec. Publ. 294, 137–151. https://doi.org/10.1144/SP294.8

Konhauser, K.O., Planavsky, N.J., Hardisty, D.S., Robbins, L.J., Warchola, T.J., Haugaard, R., Lalonde, S. V., Partin, C.A., Oonk, P.B.H., Tsikos, H., Lyons, T.W., Bekker, A., Johnson, C.M., 2017. Iron formations: A global record of Neoarchaean to Palaeoproterozoic environmental history. Earth-Science Rev. 172, 140–177. https://doi.org/10.1016/j.earscirev.2017.06.012

Kump, L.R., Junium, C., Arthur, M.A., Brasier, A., Fallick, A., Melezhik, V., Lepland, A., Črne, A.E., Luo, G., 2011. Isotopic evidence for massive oxidation of organic matter following the great oxidation event. Science (80-.). 334, 1694–1696. https://doi.org/10.1126/science.1213999

Leclerc, J., Weber, F., 1980. Geology and genesis of the Moanda manganese deposits, Republic of Gabon. Proc. XXVth Intern. Congr. Geology, Sydney (1976). In: Varensov, I.M., Gaassell, G.Y. (Eds.), Geology and Geochemitry of Manganese, 2. Schweitzerbart'sche Verl, Stutt-gart, Germany, pp. 89–109.

Luque, F.J., Crespo-Feo, E., Barrenechea, J.F., Ortega, L., 2012. Carbon isotopes of graphite: Implications on fluid history. Geosci. Front. 3, 197–207. https://doi.org/10.1016/j.gsf.2011.11.006

Mancini, F., Alviola, R., Marshall, B., Satoh, H., Papunen, H., 2000. The manganese silicate rocks of the early Proterozoic Vittinki Group, southwestern Finland: Metamorphic grade and genetic interpretations. Can. Mineral. 38, 1103–1124. https://doi.org/10.2113/gscanmin.38.5.1103

Martins, G., Oliveira, E.P., Lafon, J.M., 2009. The Algodões amphibolite-tonalite gneiss sequence, Borborema Province, NE Brazil: geochemical and geocronological evidence for Paleoproterozoic accretion of oceanic plateu/back-arc basalts and adakitic plutons. Gondwana Res. 15, 71-85.

Mayika, K.B., Moussavou, M., Prave, A.R., Lepland, A., Mbina, M., Kirsimäe, K., 2020. The Paleoproterozoic Francevillian succession of Gabon and the Lomagundi-Jatuli event. Geology 48, 1099–1104. https://doi.org/10.1130/g47651.1

Maynard, J.B., 2010. The chemistry of manganese ores through time: A signal of increasing diversity of earth-surface environments. Econ. Geol. 105, 535–552. https://doi.org/10.2113/gsecongeo.105.3.535

Mücke, A., Dzigbodi-Adjimah, K., Annor, A., 1999. Mineralogy, petrography, geochemistry and genesis of the Paleoproterozoic Birimian manganese-formation of Nsuta/Ghana. Miner. Depos. 34, 297–311. https://doi.org/10.1007/s001260050205

Munteanu, M., Marincea, S., Kasper, H.U., Zak, K., Alexe, V., Trandafir, V., Saptefrati, G., Mihalache, A., 2004. Black chert-hosted manganese deposits from the Bistritei Mountains, Eastern Carpathians (Romania): Petrography, genesis and metamorphic evolution. Ore Geol. Rev. 24, 45–65. https://doi.org/10.1016/j.oregeorev.2003.08.004

Mutti, E., Bernoulli, D., Lucchi, F.R., Tinterri, R., 2009. Turbidites and turbidity currents from alpine "flysch" to the exploration of continental margins. Sedimentology 56, 267–318. https://doi.org/10.1111/j.1365-3091.2008.01019.x

Nayak, B.R., Mohapatra, B.K., 1998. Two morphologies of pyrophanite in Mn-rich assemblages, Gangpur Group, India. Mineral. Mag. 62, 847-856.

Neves, S.P., Mariano, G., 1999. Assessing the tectonic significance of a large-scale transcurrent shear zone system: The Pernambuco lineament, northeastern Brazil. J. Struct. Geol. 21, 1369–1383. https://doi.org/10.1016/S0191-8141(99)00097-8

Neves, S.P., 2003. Proterozoic history of the Borborema province (NE Brazil): Correlations with neighboring cratons and Pan-African belts and implications for the evolution of western Gondwana. Tectonics 22. https://doi.org/10.1029/2001TC001352

Neves, S.P., 2011. Atlantica revisited: New data and thoughts on the formation and evolution of a long-lived continent. Int. Geol. Rev. 53, 1377–1391. https://doi.org/10.1080/00206814.2010.527676

Nyame, F., 2001. Petrological significance of manganese carbonate inclusions in spessartine garnet and relation to the stability of spessartine in metamorphosed manganese-rich rocks. Contrib. to Mineral. Petrol. 141, 733–746. https://doi.org/10.1007/s004100100257

Okita, P. M., Maynard, J. B., Spiker, E. C. and Force, E. R., 1988. Isotopic evidence for organic matter oxidation by manganese reduction in the formation of stratiform manganese carbonate ore. Geochim. Cosmochim. Acta, 52, 2679-2685.

Ossa, F.O., Eickmann, B., Hofmann, A., Planavsky, N.J., Asael, D., Pambo, F., Bekker, A., 2018. Two-step deoxygenation at the end of the Paleoproterozoic Lomagundi Event. Earth Planet. Sci. Lett. 486, 70–83. https://doi.org/10.1016/j.epsl.2018.01.009

Ostrander, C.M., Nielsen, S.G., Owens, J.D., Kendall, B., Gordon, G.W., Romaniello, S.J., Anbar, A.D., 2019. Fully oxygenated water columns over continental shelves before the Great Oxidation Event. Nat. Geosci. 12, 186–191. https://doi.org/10.1038/s41561-019-0309-7

Palin, R. M., & Dyck, B. (2020). Metamorphism of Pelitic (Al-Rich) Rocks. Chapter in Encyclopedia of Geology 2nd edition.

Park C.F. Jr., Dorr J.V.N. II, Guild P.W., Barbosa A.L.M. 1951. Notes on the manganese ores of Brazil. Economic Geology, 46: 1-22.

Park, C., Song, Y., Kang, I.M., Shim, J., Chung, D., Park, C.S., 2017. Metasomatic changes during periodic fluid flux recorded in grandite garnet from the Weondong W-skarn deposit, South Korea. Chem. Geol. 451, 135–153. https://doi.org/10.1016/j.chemgeo.2017.01.011

Peters, T., Schwander, H., Trommsdorff, V., 1973. Assemblages among tephroite, pyroxmangite, rhodochrosite, quartz: Experimental data and occurrences in the Rhetic Alps. Contrib. to Mineral. Petrol. 42, 325–332. https://doi.org/10.1007/BF00372610

Philpotts, A.R., Ague, J.J., 2009. Principles of igneous and metamorphic petrology, 2nd edition. Cambridge publishing.

Pickering, K., Stow, D., Watson, M., Hiscott, R., 1986. Deep-water facies, processes and models: a review and classification scheme for modern and ancient sediments. Earth Sci. Rev. 23, 75–174. https://doi.org/10.1016/0012-8252(86)90001-2

Planavsky, N.J., Slack, J.F., Cannon, W.F., O'Connell, B., Terry-Tang, Y., Asael, D.,Jackson, J.C., Hardisty, D.S., Lyons, T.W., Bekker, A., 2018. Evidence for episodic oxygenation in a weakly redox-buffered deep mid-Proterozoic ocean. Chem. Geol.http://dx.doi.org/10.1016/j.chemgeo.2018.03.028

Polgari, M., Hein, J.R., Toth, A.L., Pal-Molnár, E., Vigh, T., Biró, L., Fintor, K., 2012. Microbial action formed Jurassic Mn-carbonate ore deposit in only a few hundred years (Úrkút, Hungary). Geology 40, 903–906. https://doi.org/10.1130/G33304.1

Putnis, A., Austrheim, H., 2010. Fluid-induced processes: Metasomatism and metamorphism. Geofluids 10, 254–269. https://doi.org/10.1111/j.1468-8123.2010.00285.x

Rodrigues, O.B., Kosuki, R., Filho, A.C., 1986. Distrito Manganesífero de Serra do Navio, Amapá. In: Schbbenhaus, C.C., Silva, C.E. (Eds.), Principais Depósitos Minerais do Brasil-Volume II. Brasilia: DNPRM/CVRD, pp. 167–172.

Rodrigues, M.B., Figueiredo e Silva, R.C., Lobato, L.M., Viana, N.C.S., Alves, J.M.P., Avelar, A.N., Gonçalves, K.L.C., 2019a. Base metal minerals associated with manganese ore at Morro da Mina Mine, Conselheiro Lafaiete, Minas Gerais, Brasil: textural characterization and composition of chalcopyrite, cobaltite and pentlandite. In: Anais IV Simp Brasileiro de Metalogenia, Mai/2019, Gramado, p 120-121.

Rodrigues, M.B., Figueiredo e Silva, R.C., Lobato, L.M., Viana, N.C.S., Alves, J.M.P., Avelar, A.N., Gonçalves, K.L.C., 2019b. Petrographic caracterization and mineral chemistry of manganese ore at Morro da Mina mine, Conselheiro Lafaiete, Minas Gerais, Brasil. In: Anais IV Simp Brasileiro de Metalogenia, Mai/2019, Gramado, p 123.

Rosa-Costa, L.T., Lafon, J.M., Delor, C., 2006. Zircon geochronology and Sm-Nd isotopic study: Further constraints for the Archean and Paleoproterozoic geodynamical evolution of the southeastern Guiana Shield, north of Amazonian Craton, Brazil. Gondwana Res. 10, 277–300. https://doi.org/10.1016/j.gr.2006.02.012

Roy, S., 1981. Manganese Deposits. Academic Press, London.

Roy, S., 2006. Sedimentary manganese metallogenesis in response to the evolution of the Earth system. Earth-Science Rev. 77, 273–305. https://doi.org/10.1016/j.earscirev.2006.03.004

Roy, S., and Mitra, F.N. 1964., Mineralogy and genesis, of the gondites associated with metamorphic manganese orebodies of Madhya Pradesh and Maharashtra, India. Proc. Natl. Inst. Sci. India, **30**, 395–438.

Salgado, S.S., Caxito, F.D.A., Queiroga, G.N., De Castro, M.P., 2019. Stratigraphy, petrography and tectonics of the manganese-bearing Buritirama Formation, Northern Carajás Domain, Amazon Craton. Brazilian J. Geol. 49. https://doi.org/10.1590/2317-4889201920180106

Sawyer, E.W., 1994. Melt segregation in the continental crust. Geology 22, 1019–1022. https://doi.org/10.1130/0091-7613

Scarpelli, W., 1968. Precambrian metamorphic rocks of Serra do Navio, Brazil. (Unpublished MSc. thesis) Stanford University.

Scholz, F., Baum, M., Siebert, C., Eroglu, S., Dale, A.W., Naumann, M., Sommer, S., 2018. Sedimentary molybdenum cycling in the aftermath of seawater inflow to the intermittently euxinic Gotland Deep, Central Baltic Sea. Chem. Geol. 491, 27–38. https://doi.org/10.1016/j.chemgeo.2018.04.031

Slack, J.F., Shaw, D.R., Leitch, C.H.B., and Turner, R.J.W., 2000, Tourmalinites and coticules from the Sullivan Pb-Zn-Ag deposit and vicinity, British Columbia: Geology, geochemistry, and genesis, in Lydon, J.W., et al., eds., Geological environment of the Sullivan deposit, British Columbia: Geological Association of Canada Mineral Deposits Division Special Publication 1, 736–767.

Sousa, H.P., Parente, C.V., Magini, C., Ximenes, D.R.B., Dantas, E.L., Caby, R., Rosa Júnior, C.A., 2019. History of volcanism and sedimentation synchronous with plutonism during Rhyacian in Serra das Pipocas Greenstone Belt, Borborema Province, NE Brazil. J. South Am. Earth Sci. 95, 102220. https://doi.org/10.1016/j.jsames.2019.102220

Souza, Z.S., Kalsbeek, F., Deng, X.D., Frei, R., Kokfelt, T.F., Dantas, E.L., Li, J.W., Pimentel, M.M., Galindo, A.C., 2016. Generation of continental crust in the northern part of the Borborema Province, northeastern Brazil, from Archaean to Neoproterozoic. J. South Am. Earth Sci. 68, 68–96. https://doi.org/10.1016/j.jsames.2015.10.006

Souza, J.V. de; Ribeira Filho, E. 1983. Geologia e Gênese dos Depósitos de Manganês da Província de Aracoiaba - Pacajús, Ceará. Revista do Instituto de Geociências - Usp, São Paulo. 14, 1-11.

Spry, P.G., 1990. Geochemistry and origin of coticules (spessartine–quartz rocks) associated with metamorphosed massive sulfide deposits. In Regional Metamorphism of Ore Deposits (P.G. Spry & L.L. Bryndzia, eds.). VSP, Utrecht, The Netherlands (49-75).

Spry, P.G., Peters, J. & Slack, J.F., 2000. Meta-exhalites as keys in the search for metamorphosed ore deposits. In Metamorphosed and Metamorphogenic Ore Deposits (P.G. Spry, B. Marshall & F.M. Vokes, eds.). Rev. Econ. Geol. 11, 163-201.

Tashiro, T., Ishida, A., Hori, M., Igisu, M., Koike, M., Méjean, P., Takahata, N., Sano, Y., Komiya, T., 2017. Early trace of life from 3.95 Ga sedimentary rocks in Labrador, Canada. Nature 549, 516-518. https://doi.org/10.1038/nature24019

Teixeira, W., Oliveira, E.P., Peng, P., Dantas, E.L., Hollanda, M.H.B.M., 2017. U-Pb geochronology of the 2.0 Ga Itapecerica graphite-rich supracrustal succession in the São Francisco Craton: Tectonic matches with the North China Craton and paleogeographic inferences. Precambrian Res. 293, 91–111. https://doi.org/10.1016/j.precamres.2017.02.021

Torsvik, T.H., Cocks, L.R.M., 2013. Gondwana from top to base in space and time. Gondwana Res. 24, 999–1030. https://doi.org/10.1016/j.gr.2013.06.012

Torres, P.F.M., Cavalcante, J.C., Palheta, E.S.M., Vasconcelos, A.M., Oliveira, F.V., 2007. Folha Quixada. Folha SB-24-V-B, Escala 1:250.000. Geologia e Metalogênese. In: Programa Levantamentos Geologicos Basicos do Brasil. Fortaleza: Serviço Geologico do Brasil. CPRM.

Tribovillard, N., Algeo, T.J., Lyons, T., Riboulleau, A., 2006. Trace metals as paleoredox and paleoproductivity proxies: An update. Chem. Geol. 232, 12–32. https://doi.org/10.1016/j.chemgeo.2006.02.012

Tsikos, H., and Moore, J.M., 1997, Petrography and geochemistry of the Paleoproterozoic Hotazel iron formation, Kalahari Manganese Field, South Africa: Implications for Precambrian manganese metallogenesis: Econ. Geol., v. 92, p. 87–97. https://doi.org/10.2113/gsecongeo.92.1.87

Tsikos, H., Moore, J.M., Harris, C., 2001. Geochemistry of the Palæoproterozoic Mooidraai Formation: Fe-rich limestone as end member of iron formation deposition, Kalahari Manganese Field, Transvaal Supergroup, South Africa. J. African Earth Sci. 32, 19–27. https://doi.org/10.1016/S0899-5362(01)90016-8

Tsikos, H., Beukes, N.J., Moore, J.M., Harris, C., 2003. Deposition, diagenesis, and secondary enrichment of metals in the paleoproterozoic Hotazel Iron Formation, Kalahari manganese field, South Africa. Econ. Geol. 98, 1449–1462. https://doi.org/10.2113/gsecongeo.98.7.1449

Vasquez, M.L., Macambira, M.J.B., Armstrong, R.A., 2008. Zircon geochronology of granitoids from the western Bacajá domain, southeastern Amazonian craton, Brazil: Neoarchean to Orosirian evolution. Precambrian Res. 161, 279–302. https://doi.org/10.1016/j.precamres.2007.09.001

Vauchez, A., Neves, S., Caby, R., Corsini, M., Egydio-Silva, M., Arthaud, M., Amaro, V., 1995. The Borborema shear zone system, NE Brazil. J. South Am. Earth Sci. 8, 247–266. https://doi.org/10.1016/0895-9811(95)00012-5

Velilla, N., Jiménez-Millán, J., 2003. Origin and metamorphic evolution of rocks with braunite and pyrophanite from the Iberian Massif (SW Spain). Mineral. Petrol. 78, 73–91. https://doi.org/10.1007/s00710-002-0202-7

Veríssimo, C.U.V., Magini, C., Parente, C.V., Nogueira Neto, J. de A., de Almeida, A.R., Melo, O. de O., Arthaud, M.H., Hamelak, G.M.S., de Azevedo, L.R., 2009. Petrografia e litoquímica das formações ferríferas bandadas da região de Quixeramobim - Boa Viagem, Ceará, Brasil. Geociencias 28, 43–52.

Viegas, L.G.F., Archanjo, C.J., Hollanda, M.H.B.M., Vauchez, A., 2014. Microfabrics and zircon U-Pb (SHRIMP) chronology of mylonites from the Patos shear zone (Borborema Province, NE Brazil). Precambrian Res. 243, 1–17. https://doi.org/10.1016/j.precamres.2013.12.020

White, R.W., Powell, R., Holland, T.J.B., Johnson, T.E., Green, E.C.R., 2014. New mineral activity-composition relations for thermodynamic calculations in metapelitic systems. J. Metamorph. Geol. 32, 261–286. https://doi.org/10.1111/jmg.12071

Willner, A.P., Pawlig, S., Massonne, H.J., Hervé, F., 2001. Metamorphic evolution of spessartine quartzites (coticules) in the high-pressure, low-temperature complex at Bahia Mansa, Coastal Cordillera of South-Central Chile. Can. Mineral. 39, 1547–1569. https://doi.org/10.2113/gscanmin.39.6.1547

Yardley, B.W.D., 2009. The role of water in the evolution of the continental crust. Journal of the Geological Society, London, 166, 585–600.

Yu, W., Polgári, M., Gyollai, I., Fintor, K., Szabó, M., Kovács, I., Fekete, J., Du, Y., Zhou, Q., 2019. Microbial metallogenesis of Cryogenian manganese ore deposits in South China. Precambrian Res. 322, 122–135. https://doi.org/10.1016/j.precamres.2019.01.004

Zhang, Y., Shao, Y. jun, Wu, C. Dong, Chen, H. yong, 2017. LA-ICP-MS trace element geochemistry of garnets: Constraints on hydrothermal fluid evolution and genesis of the Xinqiao Cu–S–Fe–Au deposit, eastern China. Ore Geol. Rev. 86, 426–439. https://doi.org/10.1016/j.oregeorev.2017.03.005

Tables

Table 1. Summary of the mineral assemblage for each lithological group.

Figure captions

Fig. 1. Simplified map of the Borborema Province (northeastern Brazil) and Birimian succession from West Africa for the West Gondwana. (A) West Gondwana in the Middle Paleozoic with the Borborema Province location within the black line: 1 = Amazonian; 2= São Francisco; 3= São Luís; 4= West African; and 5= Congo cratons. Modified from Cordani et al. (2016). (B) Geological framework of the Borborema Province (according to Brito Neves et al., 2000) and southeast of Birimian succession (adapted from Beukes et al., 2016) highlighting manganese mineralization in white stars. MCD= Médio Coreaú Domain; CCD= Ceará Central Domain; TBL= Transbrasiliano Lineament; OASZ= Orós-Aiuaba Shear Zone; PSZ= Patos Shear Zone.

Fig. 2. Regional and local geological field associations showing the distribution of the manganese-rich rocks from the North Borborema Province. (A) An anomalous magnetic field (AMF) geophysical map highlighs manganese-rich rocks associated with graphite ores in a NE trend. These occurrences are in areas with low AMF that correspond to metasedimentary sequences. (B) Regional geological map of the study area. (C) Aerial photograph of the Lagoa do Riacho manganese deposit.

Fig. 3. Schematic log of the Ocr-1, Ocr-4 and Ocr-8 drill cores crossing the manganese-rich rocks and their associated rocks.

Fig. 4. Photographs showing the lithologies in the studied open pits. (A) Common intercalation of banded oxidized manganese ore with a garnet-quartzite at the top. (B) Typical view of the banded nature of the oxidized manganese ore. (C) Detailed photograph showing mineralogical interstratification in the oxidized manganese ore. (D) Manganese oxyhydroxide veinlets crosscutting the garnet quartzite. (E) The oxidized manganese ore in tilted contact with garnet quartzite and both lithologies are cut by late-aplitic veins. (F) Detailed view of the contact between the oxidized manganese ore and the garnet quartzite.

Fig. 5. Hand-specimen photographs of the OMO (A-D) and SMO (D-H). (A, B) Rhythmic banding between spessartine (Spss) + quartz (Q) and graphite (Gph) + manganese-oxyhydroxide (Mn-oh) minerals. (C) Fine-grained OMO with fine graphite flakes through a continuous foliation. Note a spessartine porphyroblast wrapped by foliation. (D) Contact between OMO with SMO showing rhythmic banding of manganese-oxyhydroxide (black) and spessartine + pyroxene (Px) (grayish white) layers. (E) SMO. Rhythmic banding consists of intercalations of manganese-oxyhydroxide and spessartine + pyroxene + olivine (Ol) layers. (F) Late-cryptomelane (Cryp) veinlets crosscutting the Mn-pyroxene rich bands. (G, H) Massive SMO comprised almost entirely of Mn-pyroxene (Pxmn).

Fig. 6. Hand-specimen photographs of the garnetite (A-B), garnet quartzite (C-F), graphite-bearing pelitic gneiss (G) and granitic intrusive rock (H). (A, B) Fine-grained and strongly foliated rock comprising spessartine (Spss) and pyroxene (Px). In hand specimen, the differentiation of these minerals is very subtle; spessartine-rich layers show a more reddish aspect whereas pyroxenes show greenish tones. (C-F) Monotonous garnet (Gt) quartzite with well distributed graphite (Gph) flakes and minor sulfide spots. Note the foliated nature of the rock in E. (F) Detailed view of minor sulfide minerals. (G) Graphite-bearing pelitic gneiss showing rhythmic banding of biotite (Bi), garnet and quartz (Q) + K-feldspar (Kfs). (H) A metamorphic aureole developed at the contact between a granitic material and a manganese-rich rock.

Fig. 7. Transmitted (A-C; under cross polarized) and reflected (E) light photomicrographs, (D, F and G) BSE images showing petrographic aspects of the OMO. (A) Spessartine (Spss) porphyroblasts within a matrix of manganese oxide (Mn-o). Note several inclusion trails of carbonate minerals (Carb) within spessartine. (B) manganese-oxide crosscutting and partially replacing manganese pyroxene (Pxmn) porphyroblast. (C) Manganese-oxide replacing tephroite (Teph). (D) Graphite flakes distributed through rock matrix in contact with spessartine, manganese pyroxene and manganese amphibole (Mn-Amp). (E) Pyrolusite (Pyro) with typical gemination, along fractures and replacing manganese pyroxene. Graphite (Gph) flake in contact with manganese pyroxene. (F) Todorokite (Td) appears intergrowing and replacing manganese silicates. (G) Colloform cryptomelane (Cryp) crosscutting matrix minerals.

Fig. 8. Transmitted light photomicrographs (A-B; under cross polarized) and BSE images (C-F) showing petrographic aspects of the SMO. (A-B) Manganese pyroxene (Pxmn) defining a granoblastic texture. Minor spessartine (Spss) occurs in contact with and included in manganese pyroxene. Fine tephroite (Teph) is in contact with pyroxene and manganese-oxyhydroxide (Mn-oh) crosses the latter. (C-D) grayish black manganese amphibole (Mn-Amp) replacing manganese pyroxene. In (C), veinlets of manganese-oxyhydroxide appear crosscutting manganese pyroxene, manganese amphibole and graphite (Gph). (D) Minor carbonate inclusion (Carb) within manganese pyroxene core. (E-F) Some sulfide minerals in rock matrix of silicate manganese ore. In (E) cobaltite (Cb) is in a triple contact with spessartine, and in (F) minor pyrite (Pyr) is in contact with graphite. Note pyrophanite (Pnt) in (F) included in manganese pyroxene.

Fig. 9. Transmitted light photomicrographs (A-D, F-G) and BSE image (E) showing petrologic aspects of the garnetite. (A) Thinly (mm-sized) banded rock with alternating spessartine (Spss) and quartz (Q) + feldspar-rich layers. Several minor graphite flakes are aligned with the foliation. (B and C) Subidioblastic-idioblastic spessartine (Spss) with polygonal texture. (C) Muscovite (Mu) in interstitial areas close to spessartine rims. (D) Pyroxene (Px) in contact with spessartine. (E) Amphibole (Amph) replacing pyroxene. (F) Epidote (Ep) in contact with spessartine, quartz and pyroxene. (G) Carbonate (Carb) as veinlets transversely crosscutting spessartine and other matrix minerals, such as quartz and pyroxene. Photomicrographs A and B are under uncrossed polarized light and C-D and F-G are under cross polarized light.

Fig. 10. Transmitted (A and E; under cross polarized) and reflected (B and C) light photomicrographs, BSE images (D and F) showing petrologic aspects of the garnet quartzite and graphite-bearing pelitic gneiss. (A and B) Graphite (Gph) flakes aligned with a well-developed foliation in contact with garnet (Gt). Two textural graphite types are shown, a “pocket" graphite with low crystallinity and a well-ordered graphite (more common). Chalcopyrite (Cp), covellite (Cv) and pyrite (Pyr) are in contact with graphite flakes. (C) Detailed view of the contact between graphite and pyrite. (D) Minor ilmenite (Ilm) and pyrophanite (Pnt) in contact with garnet. (E and F) Fibrous sillimanite (Sill) in contact with biotite (Bi) and garnet in a matrix of quartz (Q) + plagioclase (Pl) in the graphite-bearing pelitic gneiss.

Fig. 11. Ternary diagrams showing the mineral composition of: (A) Garnet (Almandine [Alm], Grossular [Gr] and Spessartine [Spss]) (Klein and Duthow, 2007); (B and C) Pyroxene (Brown et al., 1980); (D) Olivine (Forsterite [Fo], Fayalite [Fa] and Tephroite [Teph]) (modified from Klein and Duthow, 2007) (E) Amphiboles (Klein and Duthow, 2007); (F) Carbonates (Calcite [Cc], Magnesite [Mg] + Siderite [Sid] and Rhodochrosite [Rhc]) (Goldsmith and Graf, 1960); (G) Pyrophanite (Nayak and Mohapatra, 1998) for the manganese-rich rocks and their associated rocks.

Fig. 12. Profiles of analyzed garnet for the: (A and A’) oxidized manganese ore (OMO); (B and B’ and C and C’) silicate manganese ore (SMO); (D and D’) garnetite. (A-D’), notice a general Ca-Mn fractionation through these profiles. Profile for garnet of the (E and E’) garnet quartzite; (F and F’) graphite-bearing pelitic gneiss. Notice a decrease, from core to rim, in the pyrope (Mg) and an increase in almandine (Fe) molecules.

Fig. 13. X-ray mapping for Al, Ca, Fe, Si, Mg and Mn in garnet porphyroblasts within a matrix of pyrolusite for the OMO. Calcium and Mn (B and F) display variations from core to rim. Carbonate inclusions appear as spots with higher calcium content in (B). Combination of Fe, Si and Mn maps shows that pyrolusite in matrix is homogeneous in Mn content, and associated veinlets are a mixing of Si, Fe and Mn contents.

Fig. 14. (A, B, C) Pyrolusite compositions plotted on Si, Na+K+Ba and Co+Ni *vs* Mn (a.p.f.u) diagrams for the OMO. (D) Binary diagram showing mica composition (Deer et al., 1992). (E) Ternary diagram showing feldspar composition (Orthoclase [Or], Albite [Ab] and Anorthite [An]) (Deer et al., 1992).

Fig. 15. Log for element abundance in the Ocr-4 core.

Fig. 16. P-T pseudosection phase diagrams in the MnNCa(KF)MAST-COH system for graphite-bearing pelitic gneiss (sample 10029B). (A) Phase diagram with possible mineral assemblage. (B) Compositional isopleths of garnet (*X*Mg) in black and (*X*Ca) in green. Estimation of near-peak conditions is at intersection of *X*Mg (0.69) and *X*Ca (0.04) compositional isopleths and showed by a yellow ellipse. (C) Compositional isopleths of garnet (*X*Mg) in black and feldspar (*X*Na) in red. Estimation of near-peak conditions is at intersection of *X*Mg (0.69) and plagioclase (XAb = 0.7) and showed by an orange ellipse. (D) Estimations of near-peak conditions at 707 °C and 6.2 kbar (yellow ellipse) and ~7.2 kbar at ~687 °C (orange ellipse) placed on the diagram (A) showing best fit areas. Best fit areas are compatible with observed natural mineral assemblage. The mineral abbreviations are those of Holland and Powell (2011). Gt = garnet, Mu= muscovite, Pa= paragonite, St= staurolite, Fsp= feldspar, Q= quartz, Rt= rutile, Gph= graphite, Sill= sillimanite, Ilm= ilmenite, Bi= biotite, Crd= cordierite, Ky= kyanite, And= andalusite.

Fig. 17. P-T-CO_2 and fS_2 vs fO_2 pseudosection phase diagram in the MnNCaMAST system for manganese silicate ore (sample 10046). (A) T-CO_2 pseudosection highlights blue field with near-peak mineral assemblages. The green, horizontal line shows the average temperature (632ºC; see Appendix D) obtained in graphite by Raman. (B) fS_2 vs fO_2 pseudosection shows phase relations with graphite and pyrite and fugacity conditions of pyrolusite precipitation. The mineral abbreviations are those of Holland and Powell (2011): Teph= tephroite, Spss = spessartine, Di= diopside, Rhod= rhodonite, Cc= calcite, Rhc= rhodochrosite, Q= quartz, Cumm= cummingtonite, Zo= zoisite, Prl= pyrophyllite, An= anorthite, Kao= kaolinite, Pxmn= pyroxmangite, Pyro= pyrolusite, Pyr= pyrite, Po= pyrrhotite, Gph= graphite, Pnt= pyrophanite, Carb= carbonate.

Fig. 18. Mineral paragenesis chart showing pre-metamorphic, metamorphic and supergene stages for the studied manganese-rich rocks of the Borborema Province. Pre-metamorphic stage is inferred as diagenetic or earliest minerals.

Fig. 19. Schematic sketch showing the evolution of manganese mineralization and their host rocks from deposition to metal enrichment. (A) Deposition of the manganese-rich sedimentary precursors and their host rocks in an

anoxic/euxinic basin. Wacke was deposited in proximal areas and interbedded with sandy/silty marl and muddy marl. Organic-rich mudstones were deposited in the most distal areas of the basin. (B) Increase of burial as a result of metamorphism recyrstallized wackes to garnet quartzite, manganese-rich sandy/silty marls to manganese silicate rocks and manganese-rich muddy marl to spessartine-bearing manganese rocks (i.e., OMO and garnetite). Graphite-bearing pelitic gneiss is the metamorphic product of organic-rich mudstones. Surface weathering and leaching of manganese silicates during uplift generated oxidized manganese minerals.

Table 1: Summary of the mineral assemblages from each lithological group.

Lithotype	Common minerals	Accessory minerals
Oxidized manganese ore - (OMO)	Pyrolusite, todorokite, cryptomelane, undifferenciated manganese-oxyhydroxide minerals, spessartine, manganese-pyroxene and graphite	Carbonate, manganese-amphibole and pyrophanite
Silicate manganese ore - (SMO)	Tephroite, manganese-pyroxene, spessartine and graphite	Carbonate, manganese-amphibole, pyrophanite, jacobsite, todorokite, cobaltite, pyrite and chalcopyrite
Garnetite	Spessartine, quartz, rhodonite, amphibole, graphite, epidote, carbonate, mica	Titanite, pyrite, chalcopyrite and magnetite
Garnet quartzite	Albite, quartz, mica, graphite and almandine garnet	Pyrite, chalcopyrite, covellite, pyrophanite, ilmenite, zircon and monazite
Graphite-bearing pelitic gneiss	Biotite, muscovite, sillimanite, quartz, cordierite, feldspar, garnet and graphite	Zircon, monazite, rutile and ilmenite

Figure 1

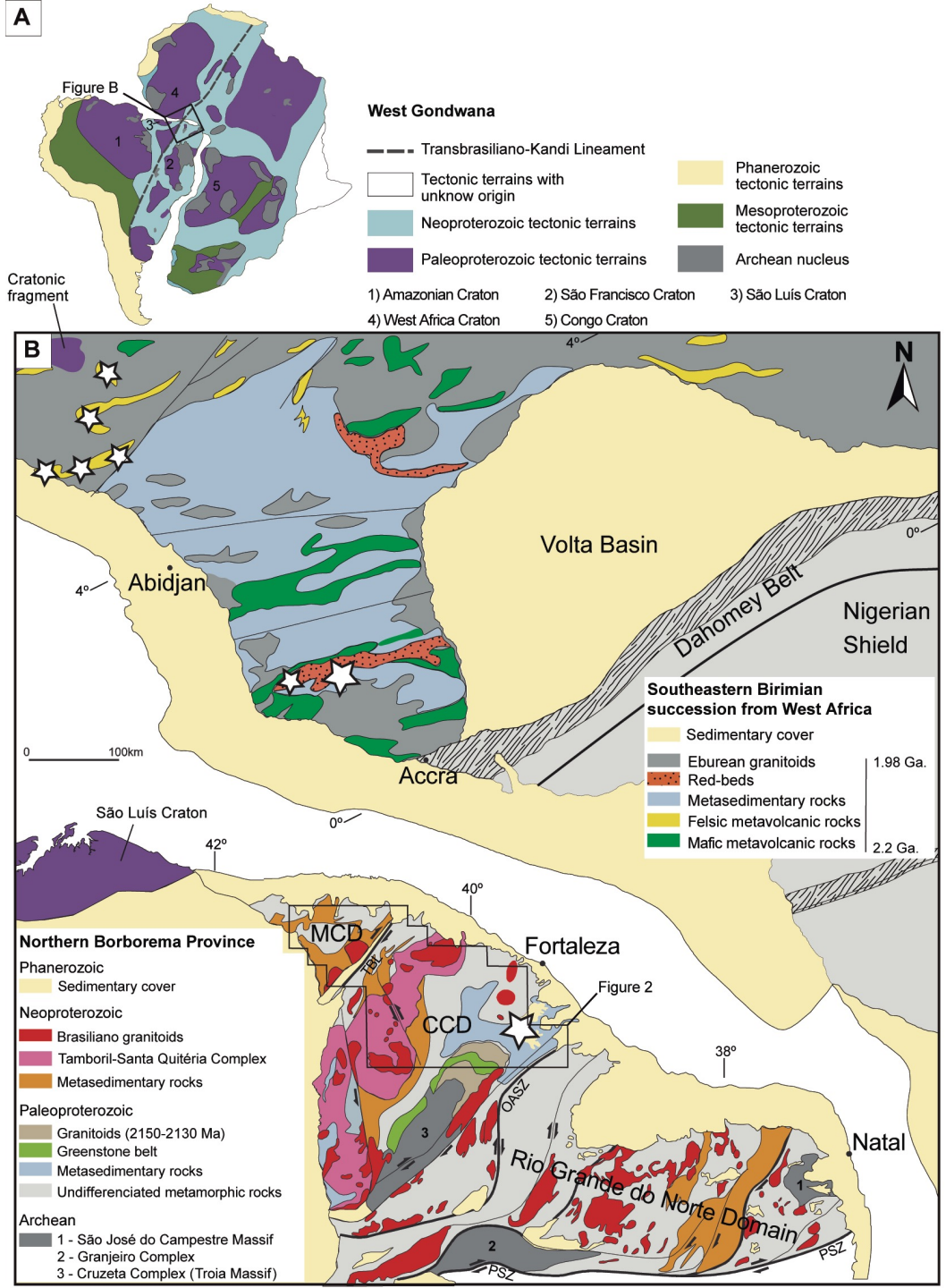
A
Figure B
1
2
3
4
5
Cratonic fragment
West Gondwana
Transbrasiliano-Kandi Lineament
Tectonic terrains with unknow origin
Neoproterozoic tectonic terrains
Paleoproterozoic tectonic terrains
Phanerozoic tectonic terrains
Mesoproterozoic tectonic terrains
Archean nucleus
1) Amazonian Craton
2) São Francisco Craton
3) São Luís Craton
4) West Africa Craton
5) Congo Craton
B
N
4º
0º
Abidjan
Volta Basin
Dahomey Belt
Nigerian Shield
Accra
0
100km
São Luís Craton
42º
40º
38º
Fortaleza
Natal
MCD
FBF
CCD
Figure 2
OASZ
PSZ
Rio Grande do Norte Domain
Southeastern Birimian succession from West Africa
Sedimentary cover
Eburean granitoids
Red-beds
Metasedimentary rocks
Felsic metavolcanic rocks
Mafic metavolcanic rocks
1.98 Ga.
2.2 Ga.
Northern Borborema Province
Phanerozoic
Sedimentary cover
Neoproterozoic
Brasiliano granitoids
Tamboril-Santa Quitéria Complex
Metasedimentary rocks
Paleoproterozoic
Granitoids (2150-2130 Ma)
Greenstone belt
Metasedimentary rocks
Undifferenciated metamorphic rocks
Archean
1 - São José do Campestre Massif
2 - Granjeiro Complex
3 - Cruzeta Complex (Troia Massif)

Figure 2

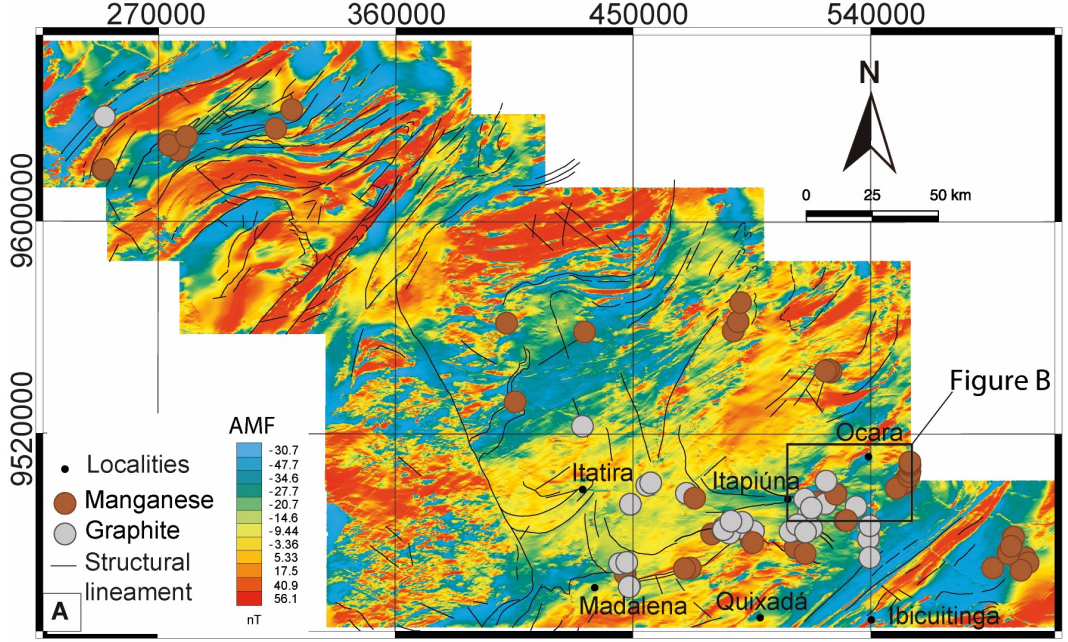

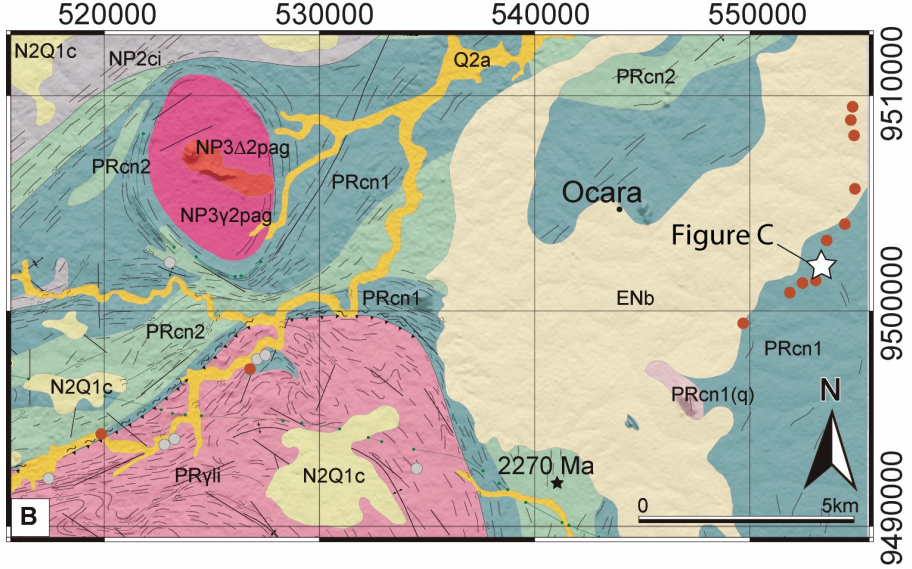

Cenozoic covers

Q2a	Alluvial deposits
N2Q1c	Colluvial-alluvial deposits: Sands, clayey sands and clays.
ENb	Barreiras Group: Medium- to fine-grained sandstones with conglomeratic layers and lateric nodules in its base.

Neoproterozoic

NP3Δ2pag	Foliated gabbro, gabbronorite and diorites of calc-alkaline nature.
NP3γ2pag	Fine-grained leucocratic granite with enclave of mafic rocks.
NP2ci	Independência Unit: Migmatitic paragneisses

Paleoproterozoic

Canindé do Ceará Complex

PRcn1	Metasedimentary Unit: Paragneiss with amphibolite, quartzite(q), metacarbonate, metamafic rock (mb) and iron formation.
PRcn2	Orthoderived Unit: Orthogneisses with subordinate amphibolite lenses (af) and rare migmatitic paragneisses.
PRγli	S-type meta-leucogranite, with or without garnet and sillimanite.

Geological features

- Dike
- Structural lineament
- Contractional shear zone
- Transcurrent dextral shear zone
- Transcurrent shear zone
- Antiform
- Synform

Ore mineral occurence

- Manganese
- Graphite

Geochronology

- ★ Whole-rock Sm-Nd isochron

Figure 3

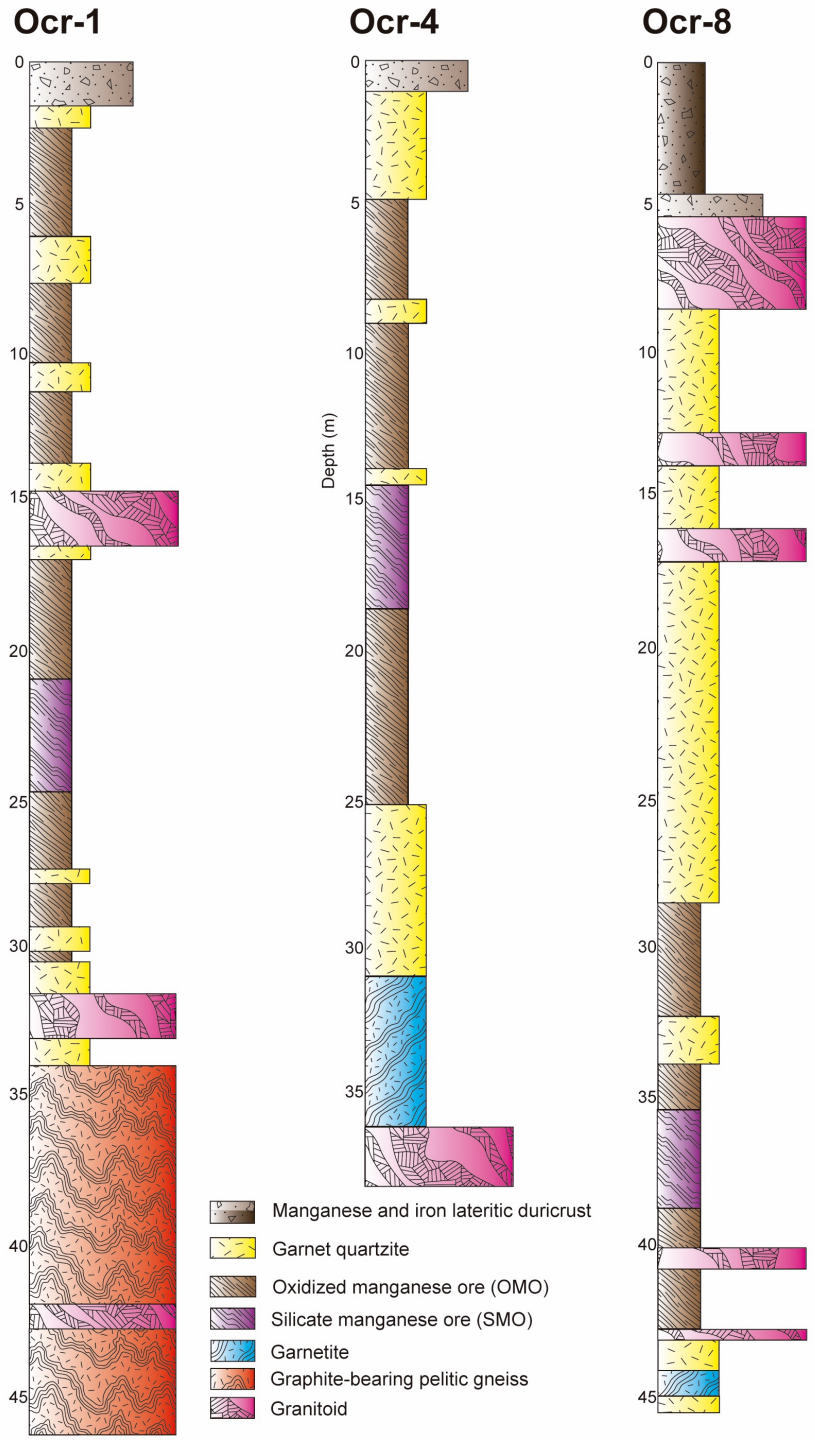
Ocr-1
Ocr-4
Ocr-8
Depth (m)
0
5
10
15
20
25
30
35
40
45
Manganese and iron lateritic duricrust
Garnet quartzite
Oxidized manganese ore (OMO)
Silicate manganese ore (SMO)
Garnetite
Graphite-bearing pelitic gneiss
Granitoid

Figure 4

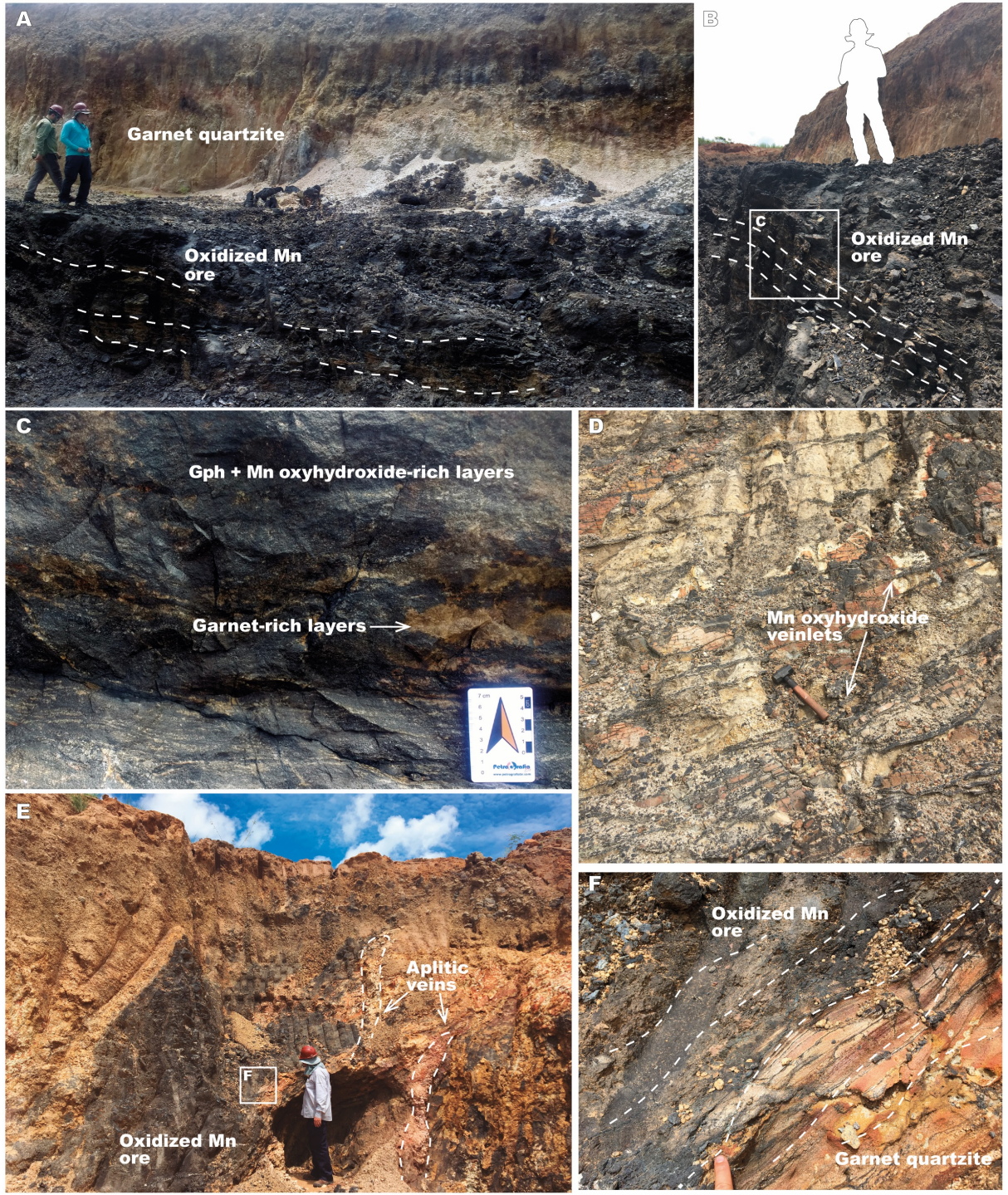
A
Garnet quartzite
Oxidized Mn ore
B
C
Oxidized Mn ore
C
Gph + Mn oxyhydroxide-rich layers
Garnet-rich layers
D
Mn oxyhydroxide veinlets
E
Aplitic veins
F
Oxidized Mn ore
F
Oxidized Mn ore
Garnet quartzite

Figure 5

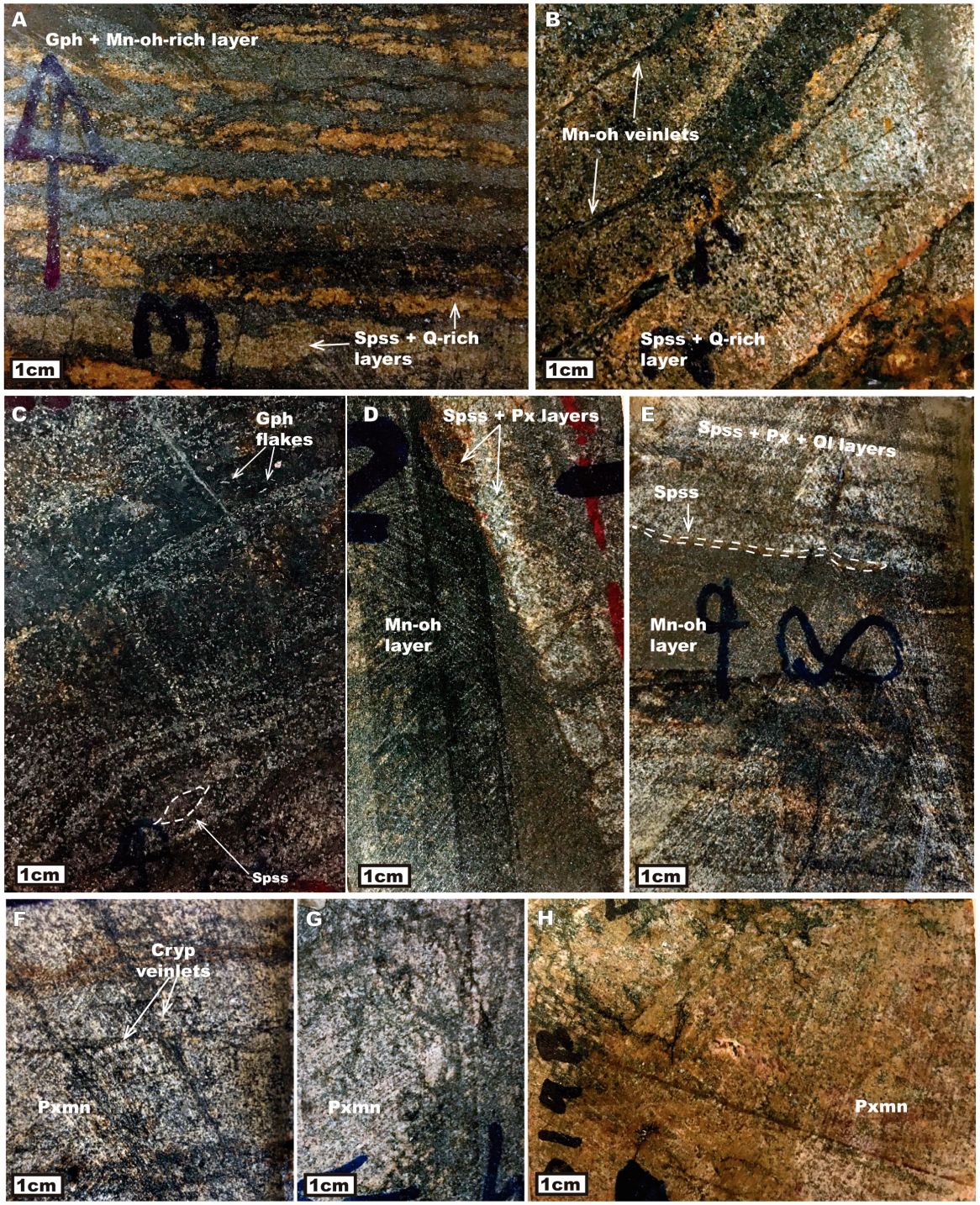
A
Gph + Mn-oh-rich layer
Spss + Q-rich layers
1cm
B
Mn-oh veinlets
Spss + Q-rich layer
1cm
C
Gph flakes
Spss
1cm
D
Spss + Px layers
Mn-oh layer
1cm
E
Spss + Px + Ol layers
Spss
Mn-oh layer
1cm
F
Cryp veinlets
Pxmn
1cm
G
Pxmn
1cm
H
Pxmn
1cm

Figure 6

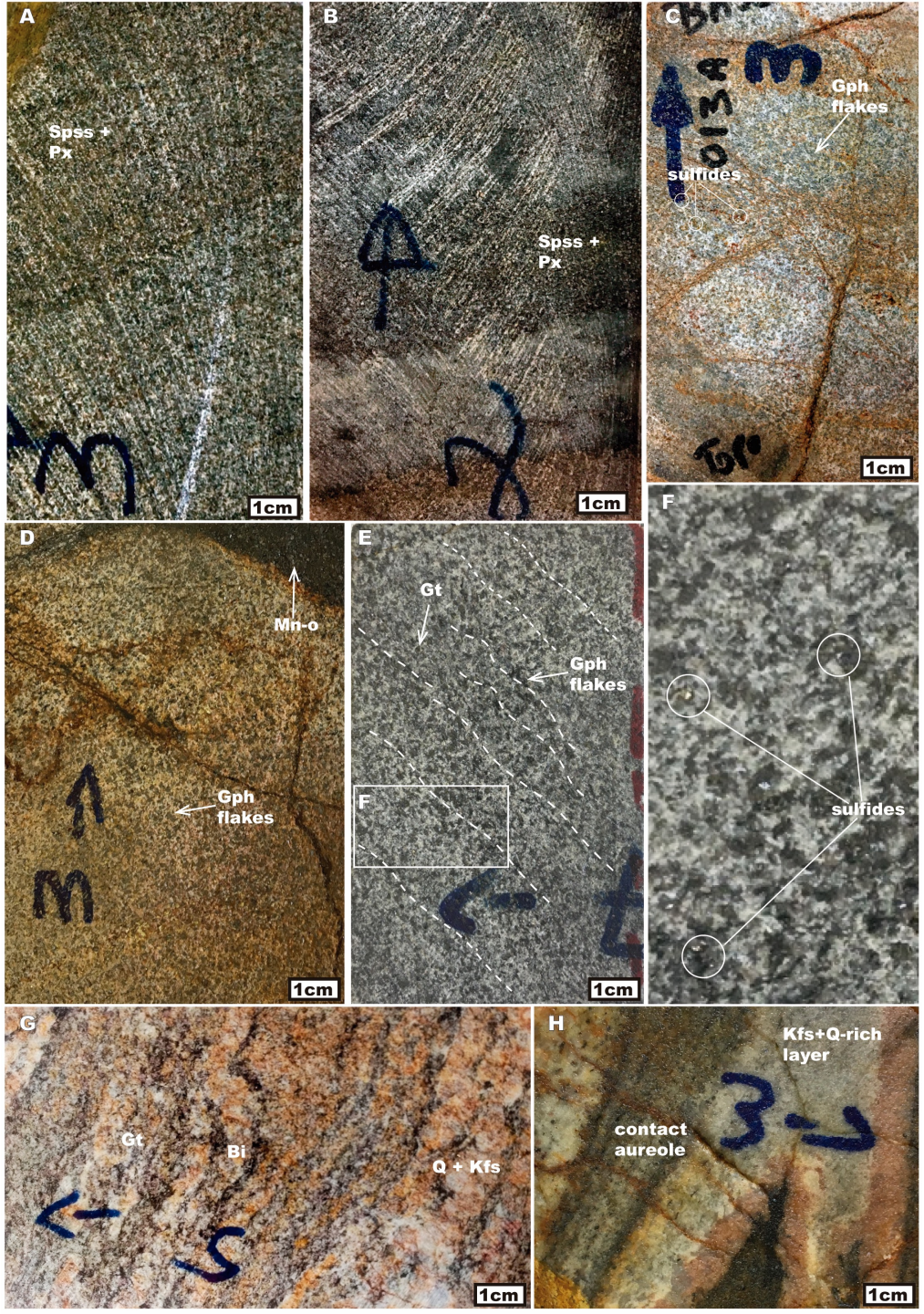
A
Spss +
Px
1cm
B
Spss +
Px
1cm
C
Gph
flakes
sulfides
1cm
D
Mn-o
Gph
flakes
1cm
E
Gt
Gph
flakes
F
1cm
F
sulfides
G
Gt
Bi
Q + Kfs
1cm
H
Kfs+Q-rich
layer
contact
aureole
1cm

Figure 7

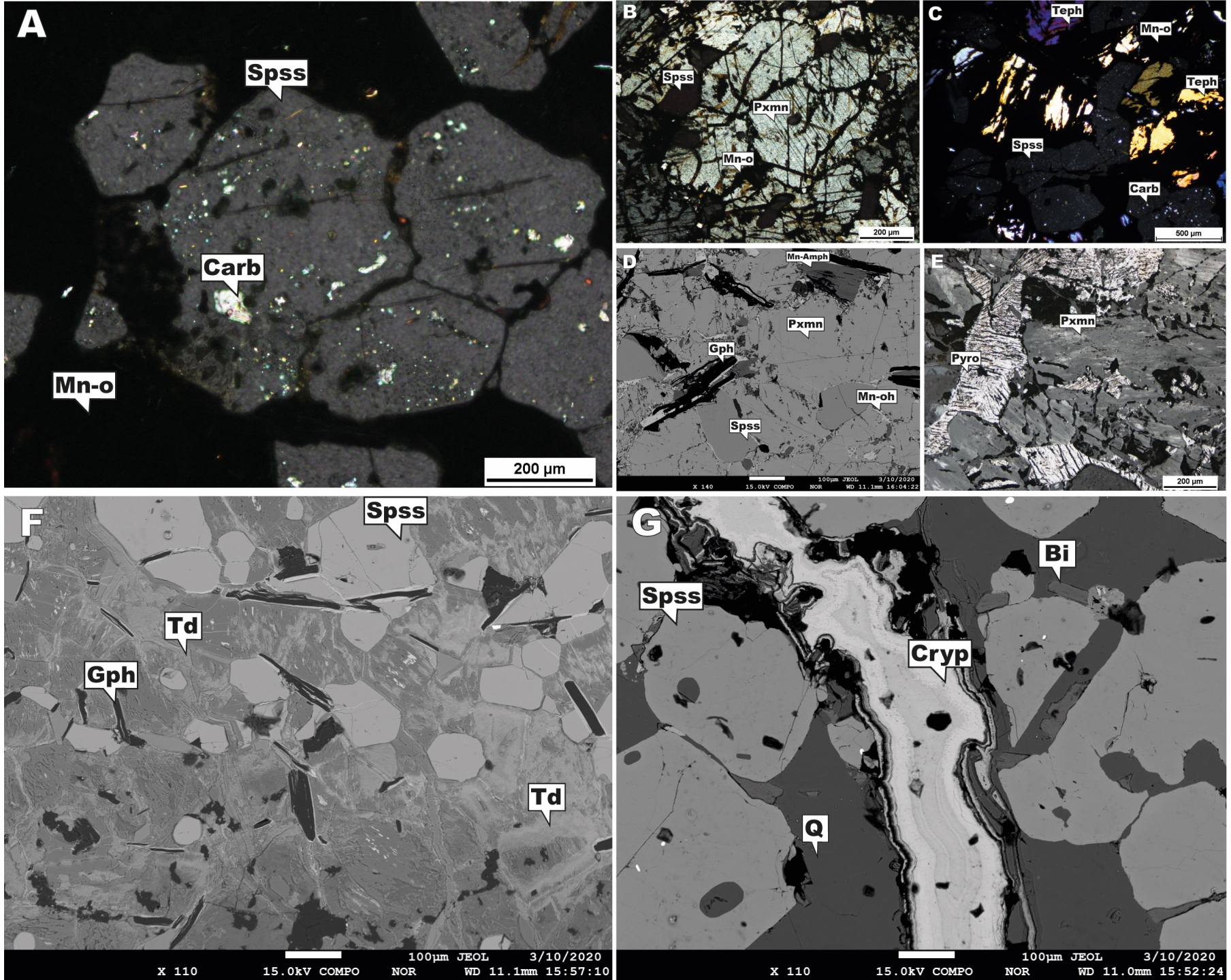
A
Spss
Carb
Mn-o
200 µm
B
Spss
Pxmn
Mn-o
200 µm
C
Teph
Mn-o
Teph
Spss
Carb
500 µm
D
Mn-Amph
Pxmn
Gph
Mn-oh
Spss
100µm JEOL 3/10/2020
X 140 15.0kV COMPO NOR WD 11.1mm 16:04:22
E
Pxmn
Pyro
200 µm
F
Spss
Td
Gph
Td
100µm JEOL 3/10/2020
X 110 15.0kV COMPO NOR WD 11.1mm 15:57:10
G
Bi
Spss
Cryp
Q
100µm JEOL 3/10/2020
X 110 15.0kV COMPO NOR WD 11.0mm 15:52:24

Figure 8

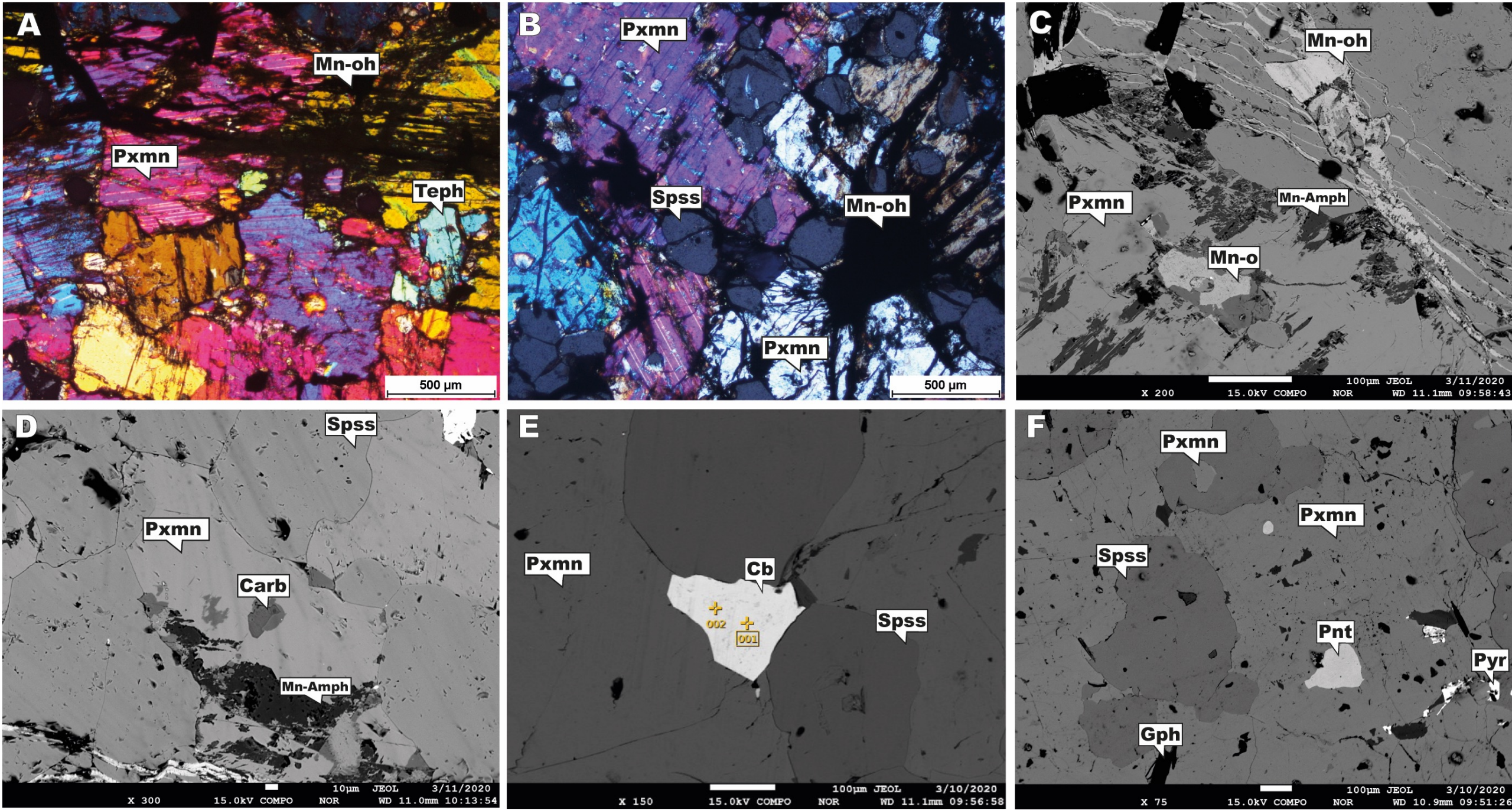
A
Mn-oh
Pxmn
Teph
500 µm
B
Pxmn
Spss
Mn-oh
Pxmn
500 µm
C
Mn-oh
Pxmn
Mn-Amph
Mn-o
100µm JEOL 3/11/2020
X 200 15.0kV COMPO NOR WD 11.1mm 09:58:43
D
Spss
Pxmn
Carb
Mn-Amph
10µm JEOL 3/11/2020
X 300 15.0kV COMPO NOR WD 11.0mm 10:13:54
E
Pxmn
Cb
002
001
Spss
100µm JEOL 3/10/2020
X 150 15.0kV COMPO NOR WD 11.1mm 09:56:58
F
Pxmn
Pxmn
Spss
Pnt
Pyr
Gph
100µm JEOL 3/10/2020
X 75 15.0kV COMPO NOR WD 10.9mm 09:51:26

Figure 9

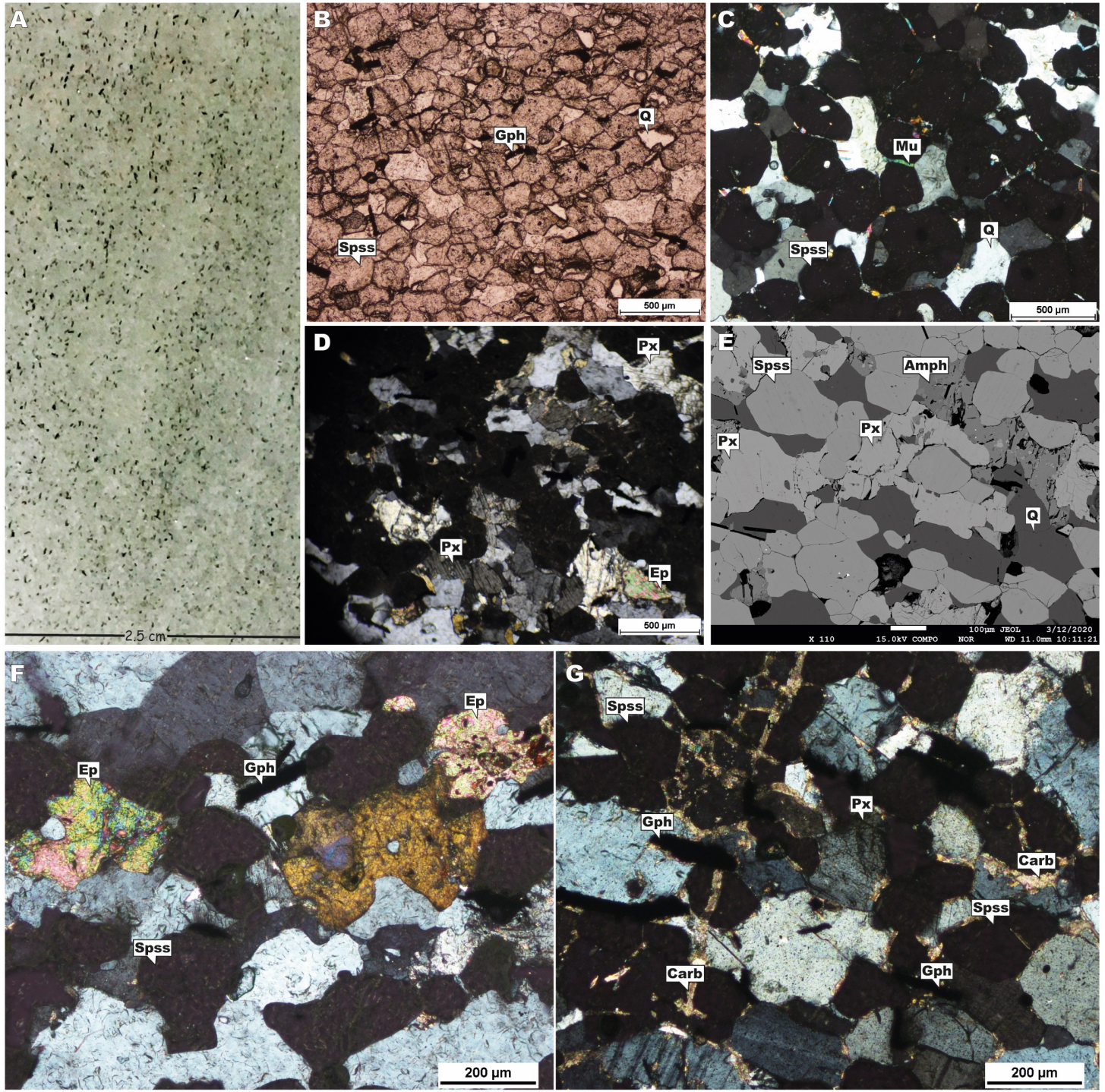
A
2.5 cm
B
Gph
Q
Spss
500 µm
C
Mu
Q
Spss
500 µm
D
Px
Px
Ep
500 µm
E
Spss
Amph
Px
Px
Q
100µm JEOL 3/12/2020
X 110 15.0kV COMPO NOR WD 11.0mm 10:11:21
F
Ep
Ep
Gph
Spss
200 µm
G
Spss
Px
Gph
Carb
Spss
Carb
Gph
200 µm

Figure 10

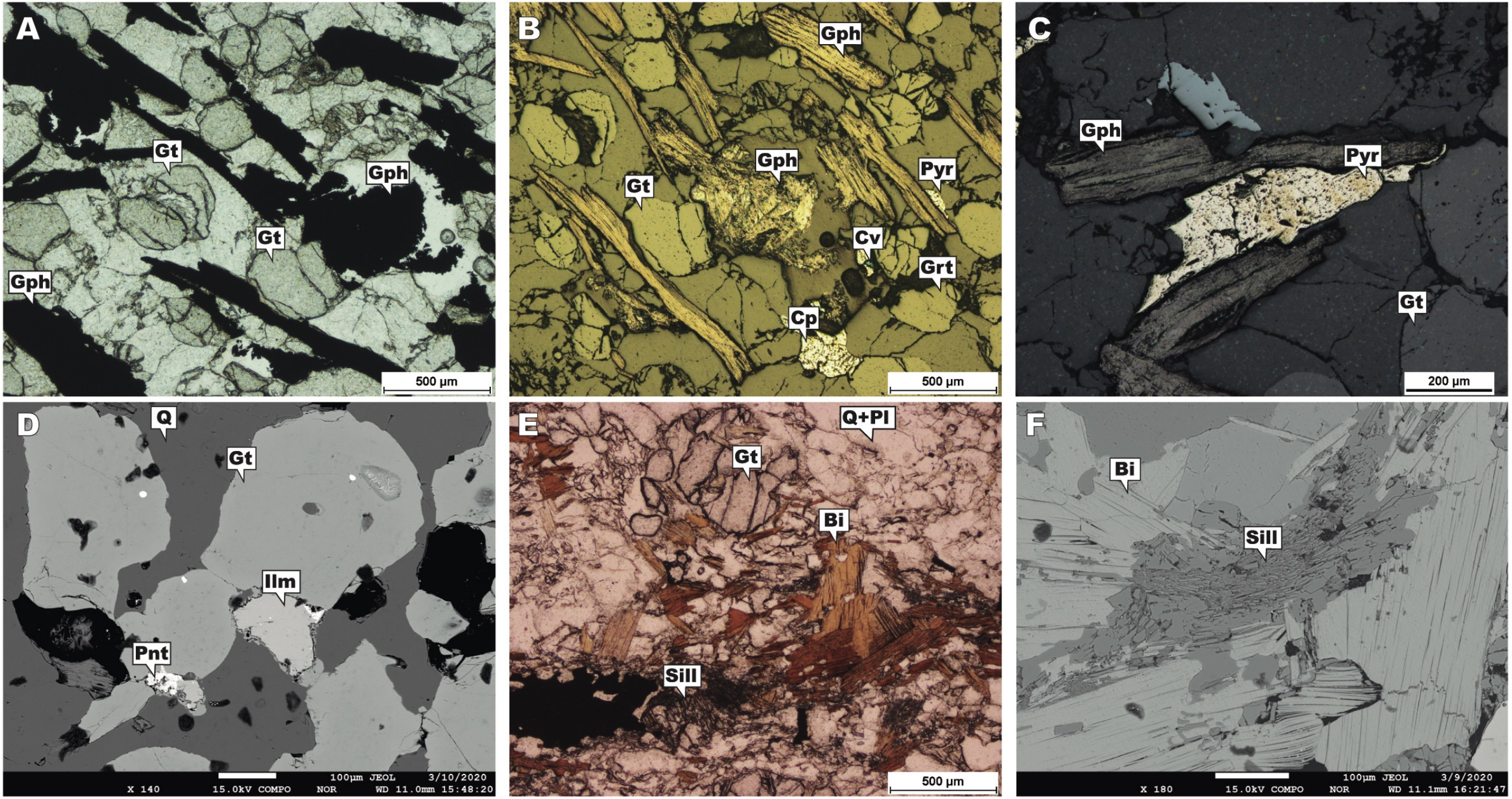
A
Gt
Gph
Gt
Gph
500 µm
B
Gph
Gph
Pyr
Gt
Cv
Grt
Cp
500 µm
C
Gph
Pyr
Gt
200 µm
D
Q
Gt
Ilm
Pnt
100µm JEOL 3/10/2020
X 140 15.0kV COMPO NOR WD 11.0mm 15:48:20
E
Q+Pl
Gt
Bi
Sill
500 µm
F
Bi
Sill
100µm JEOL 3/9/2020
X 180 15.0kV COMPO NOR WD 11.1mm 16:21:47

Figure 11

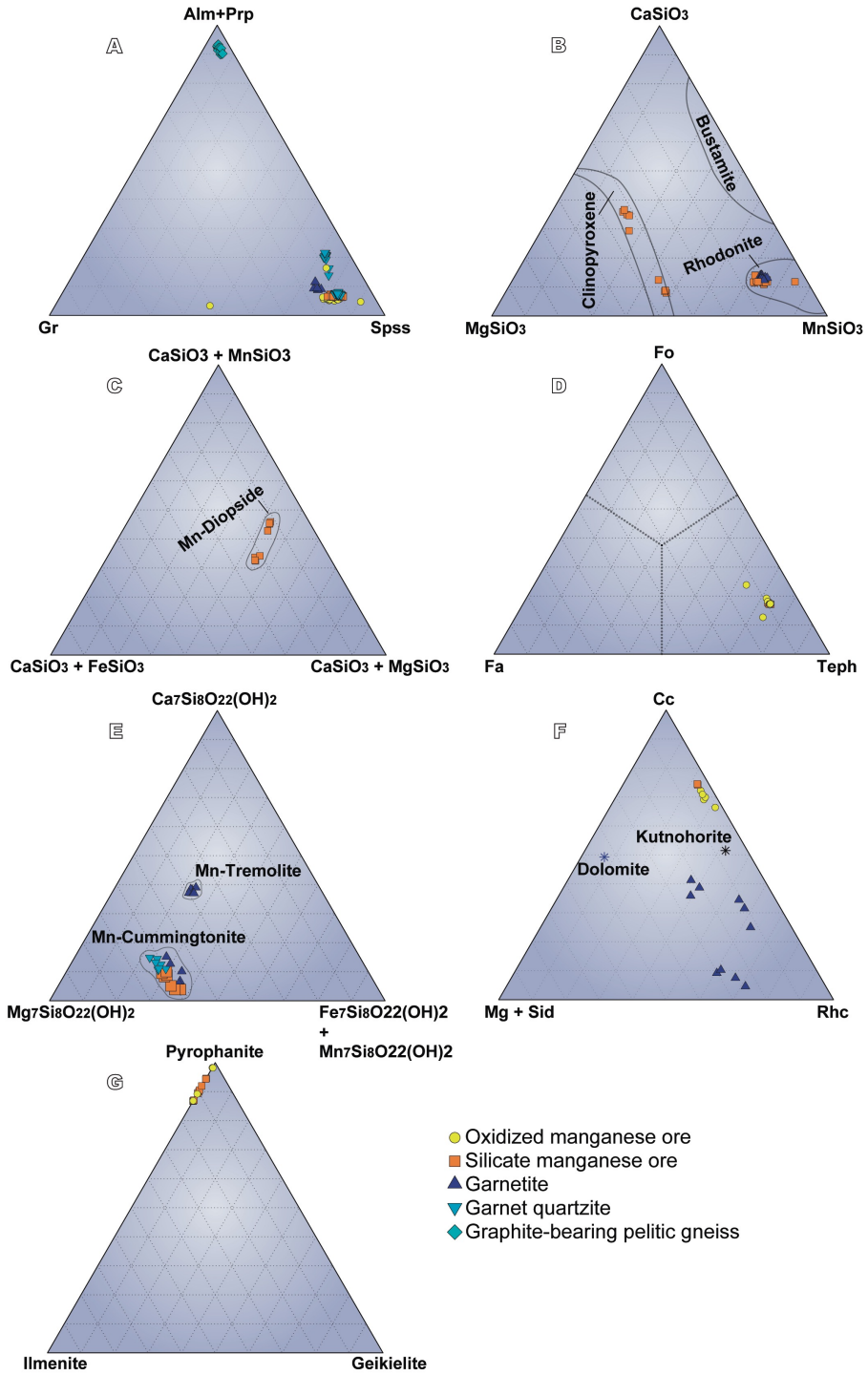
A
Alm+Prp
Gr
Spss
B
CaSiO3
Bustamite
Clinopyroxene
Rhodonite
MgSiO3
MnSiO3
C
CaSiO3 + MnSiO3
Mn-Diopside
CaSiO3 + FeSiO3
CaSiO3 + MgSiO3
D
Fo
Fa
Teph
E
Ca7Si8O22(OH)2
Mn-Tremolite
Mn-Cummingtonite
Mg7Si8O22(OH)2
Fe7Si8O22(OH)2
+
Mn7Si8O22(OH)2
F
Cc
Kutnohorite
Dolomite
Mg + Sid
Rhc
G
Pyrophanite
Ilmenite
Geikielite
Oxidized manganese ore
Silicate manganese ore
Garnetite
Garnet quartzite
Graphite-bearing pelitic gneiss

Figure 12

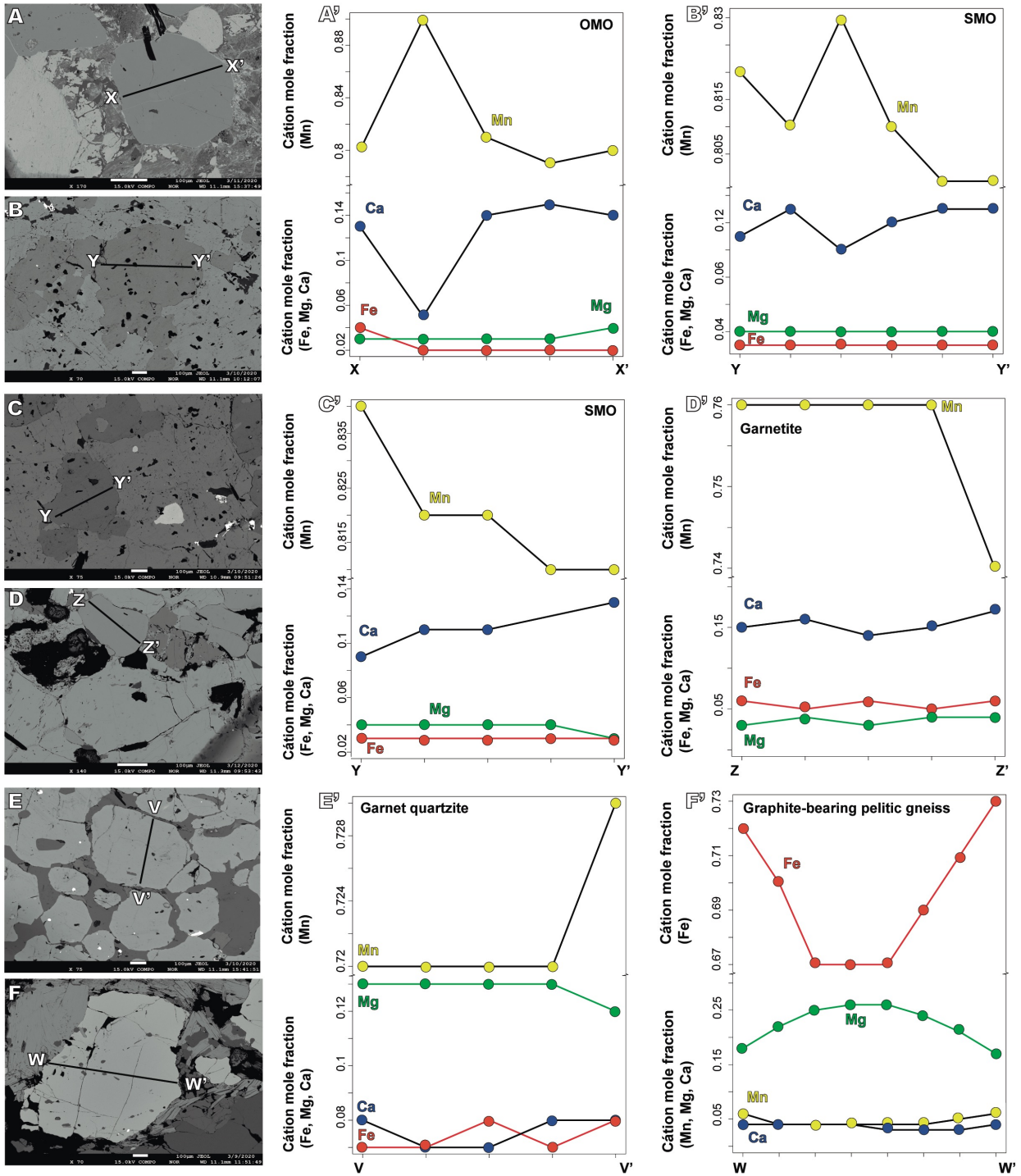
A
X'
X
B
Y
Y'
C
Y'
Y
D
Z
Z'
E
V
V'
F
W
W'
A'
OMO
Cation mole fraction (Mn)
Cation mole fraction (Fe, Mg, Ca)
Mn
Ca
Fe
Mg
X
X'
B'
SMO
Y
Y'
C'
SMO
D'
Garnetite
Z
Z'
E'
Garnet quartzite
V
V'
F'
Graphite-bearing pelitic gneiss
Cation mole fraction (Fe)
Cation mole fraction (Mn, Mg, Ca)
W
W'

Figure 13

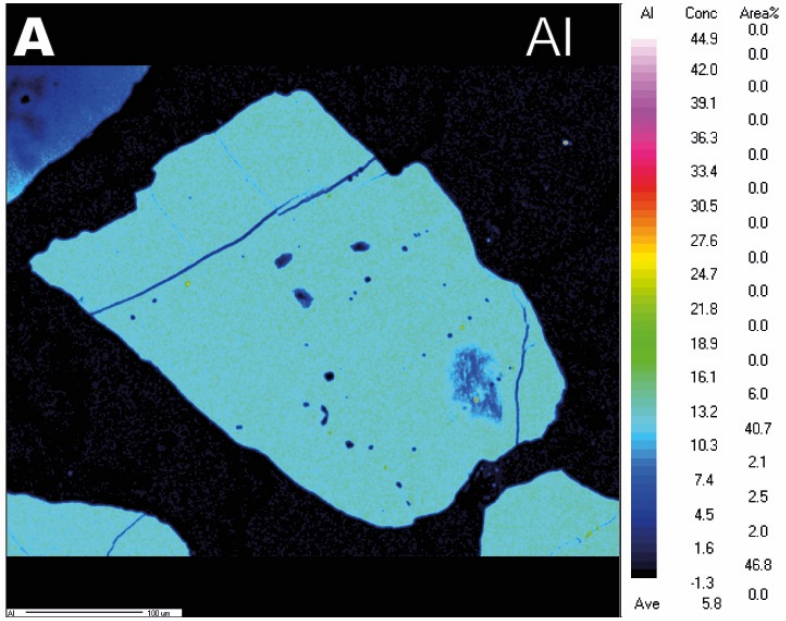

Al	Conc	Area%
	44.9	0.0
	42.0	0.0
	39.1	0.0
	36.3	0.0
	33.4	0.0
	30.5	0.0
	27.6	0.0
	24.7	0.0
	21.8	0.0
	18.9	0.0
	16.1	6.0
	13.2	40.7
	10.3	2.1
	7.4	2.5
	4.5	2.0
	1.6	46.8
	-1.3	0.0
Ave	5.8	

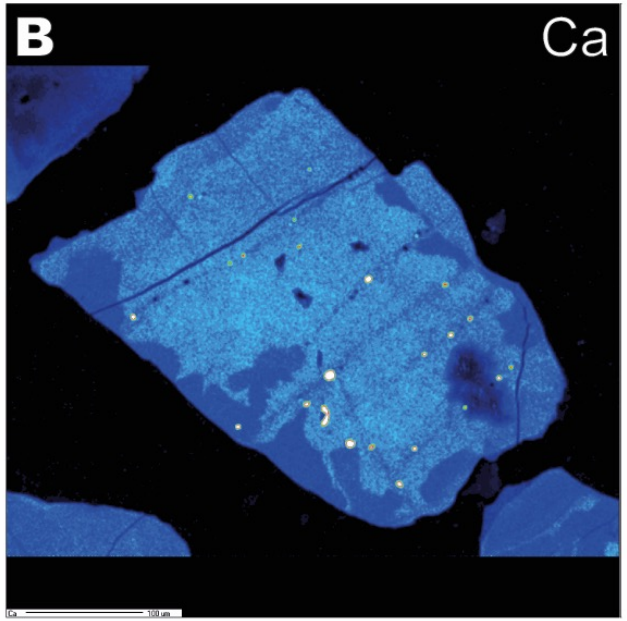

Ca	Conc	Area%
	19.8	0.1
	18.5	0.0
	17.3	0.0
	16.0	0.0
	14.7	0.0
	13.5	0.0
	12.2	0.0
	10.9	0.0
	9.6	0.0
	8.4	0.0
	7.1	0.0
	5.8	0.2
	4.6	33.9
	3.3	13.4
	2.0	4.5
	0.8	47.6
	-0.5	0.0
Ave	1.6	

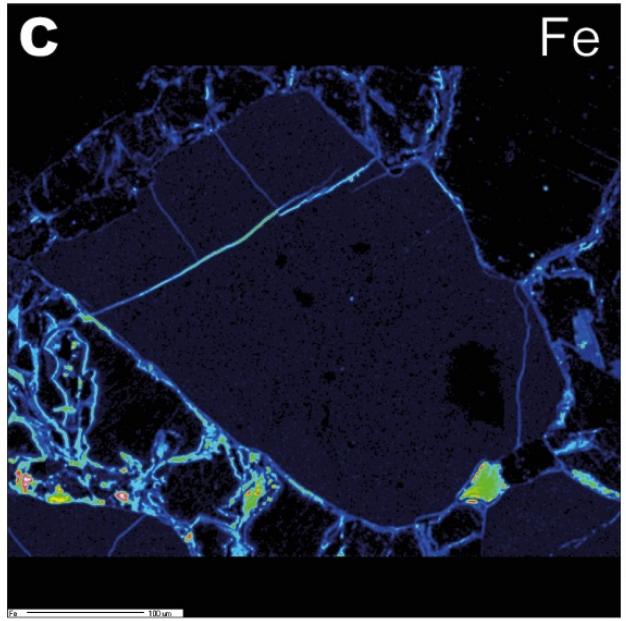

Fe	Conc	Area%
	62.8	0.0
	58.8	0.0
	54.9	0.0
	50.9	0.0
	46.9	0.0
	43.0	0.0
	39.0	0.0
	35.0	0.1
	31.0	0.1
	27.1	0.3
	23.1	0.7
	19.1	1.4
	15.1	2.0
	11.2	3.4
	7.2	5.6
	3.2	86.2
	-0.7	0.0
Ave	1.8	

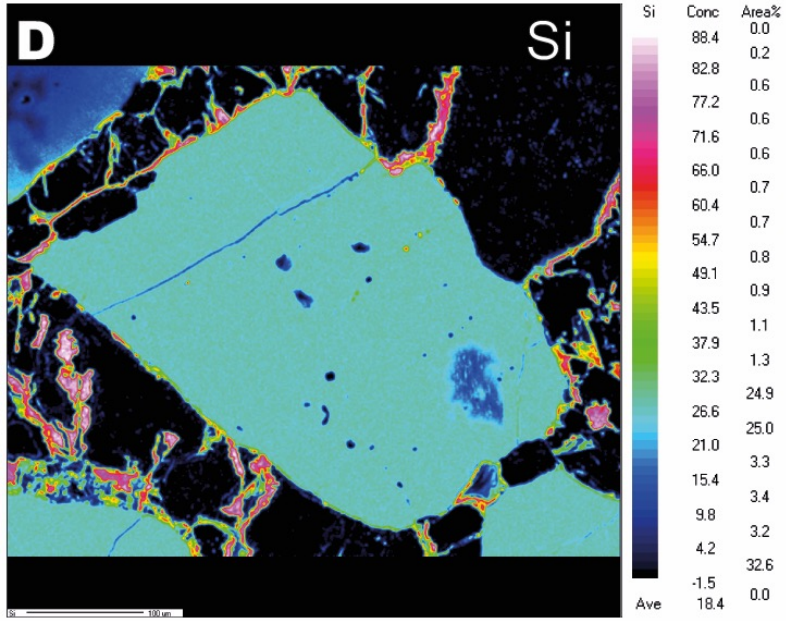

Si	Conc	Area%
	88.4	0.0
	82.8	0.2
	77.2	0.6
	71.6	0.6
	66.0	0.6
	60.4	0.7
	54.7	0.7
	49.1	0.8
	43.5	0.9
	37.9	1.1
	32.3	1.3
	26.6	24.9
	21.0	25.0
	15.4	3.3
	9.8	3.4
	4.2	3.2
	-1.5	32.6
Ave	18.4	0.0

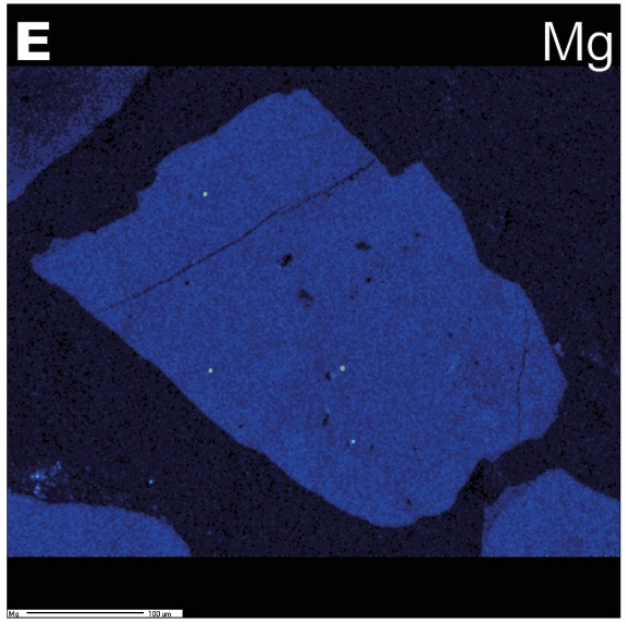

Mg	Conc	Area%
	7.2	0.0
	6.7	0.0
	6.2	0.0
	5.7	0.0
	5.2	0.0
	4.7	0.0
	4.2	0.0
	3.8	0.0
	3.3	0.0
	2.8	0.0
	2.3	0.0
	1.8	0.0
	1.3	0.0
	0.8	0.0
	0.3	6.8
	-0.2	43.5
	-0.6	49.7
Ave	-0.3	0.0

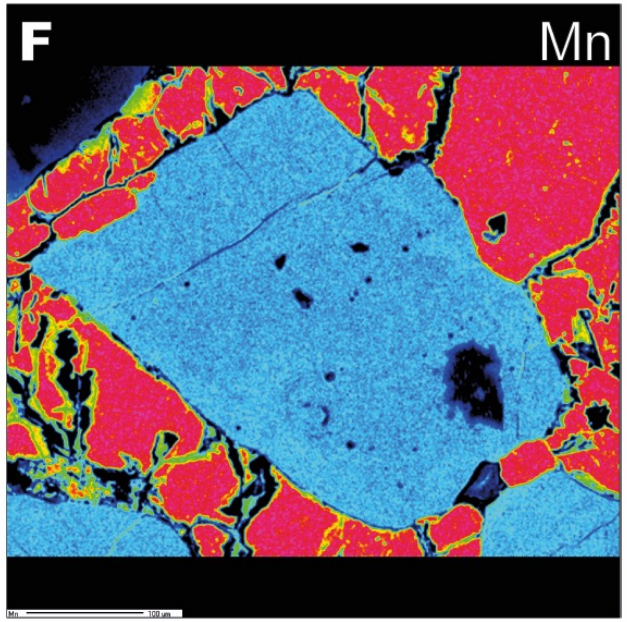

Mn	Conc	Area%
	94.2	0.0
	88.8	0.0
	83.5	0.0
	78.1	0.1
	72.8	11.3
	67.4	15.8
	62.0	2.9
	56.7	1.9
	51.3	1.6
	45.9	1.4
	40.6	1.4
	35.2	1.3
	29.9	18.6
	24.5	31.0
	19.1	2.0
	13.8	2.2
	8.4	3.0
Ave	41.2	5.4

Figure 14

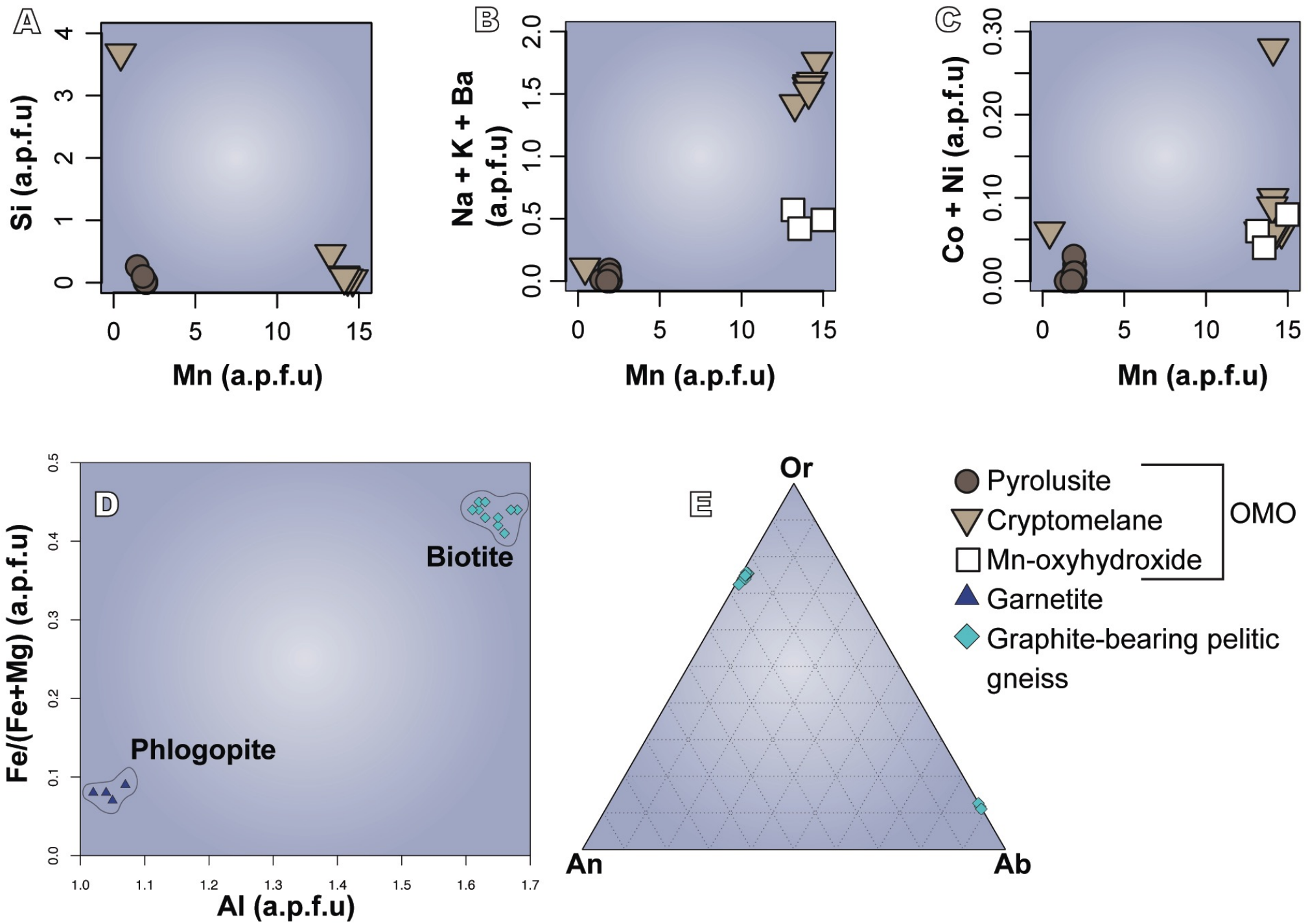
A
Si (a.p.f.u)
Mn (a.p.f.u)
B
Na + K + Ba (a.p.f.u)
Mn (a.p.f.u)
C
Co + Ni (a.p.f.u)
Mn (a.p.f.u)
D
Biotite
Phlogopite
Fe/(Fe+Mg) (a.p.f.u)
Al (a.p.f.u)
E
Or
An
Ab
Pyrolusite
Cryptomelane
Mn-oxyhydroxide
OMO
Garnetite
Graphite-bearing pelitic gneiss

Figure 15

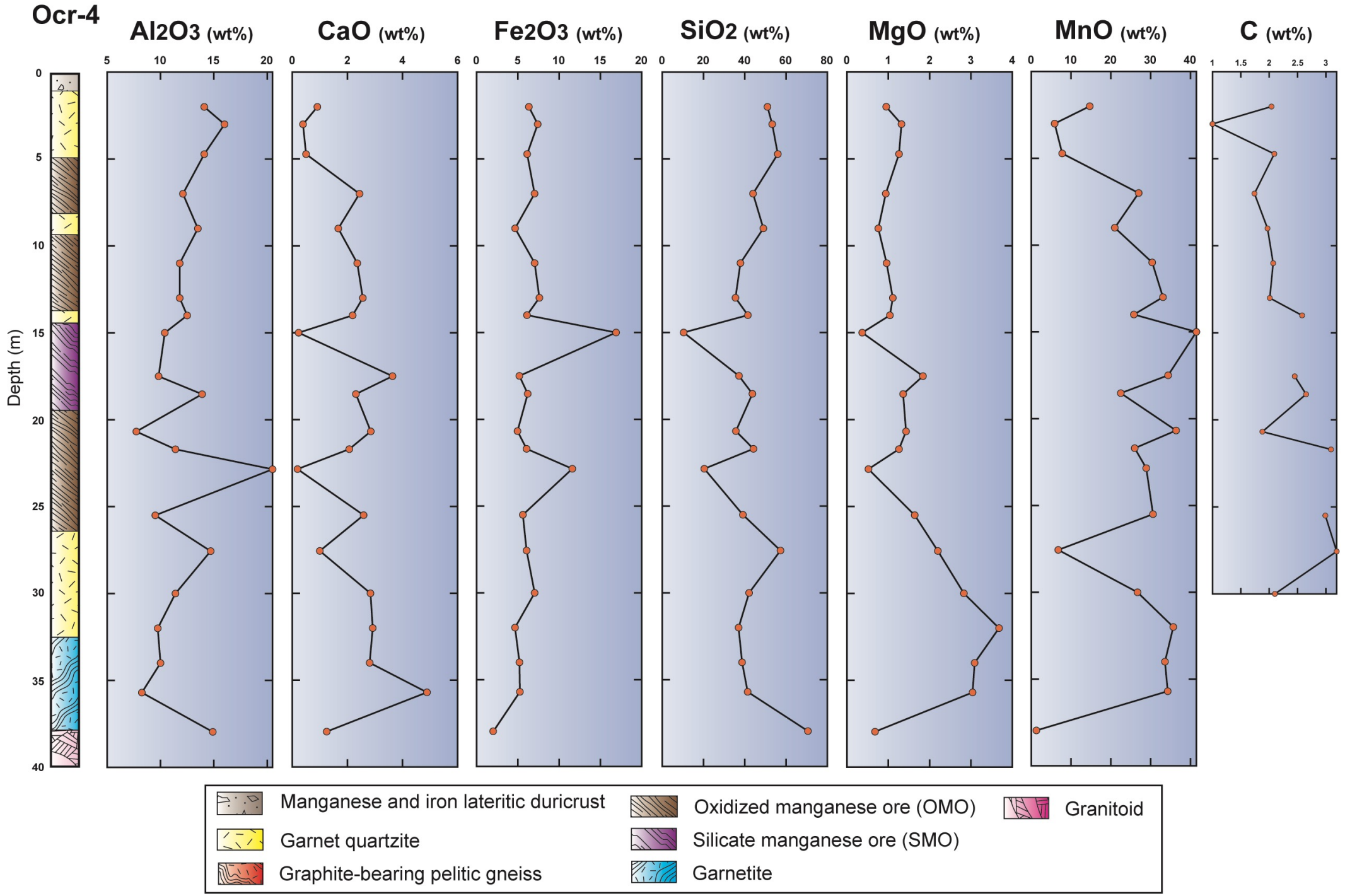
Ocr-4
Al2O3 (wt%)
CaO (wt%)
Fe2O3 (wt%)
SiO2 (wt%)
MgO (wt%)
MnO (wt%)
C (wt%)
Depth (m)
Manganese and iron lateritic duricrust
Garnet quartzite
Graphite-bearing pelitic gneiss
Oxidized manganese ore (OMO)
Silicate manganese ore (SMO)
Garnetite
Granitoid

Figure 16

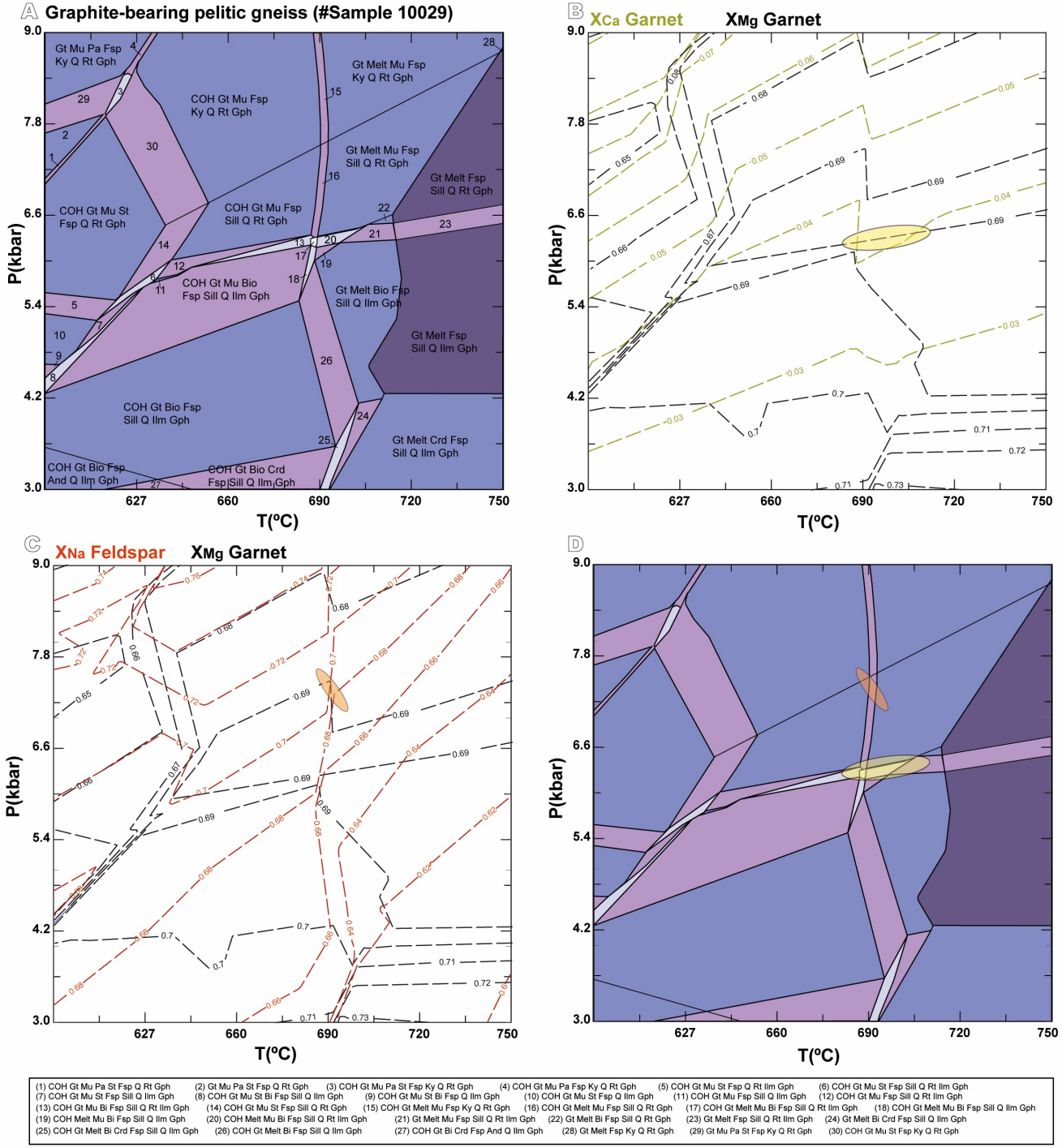
A Graphite-bearing pelitic gneiss (#Sample 10029)
Gt Mu Pa Fsp Ky Q Rt Gph
COH Gt Mu Fsp Ky Q Rt Gph
Gt Melt Mu Fsp Ky Q Rt Gph
Gt Melt Mu Fsp Sill Q Rt Gph
Gt Melt Fsp Sill Q Rt Gph
COH Gt Mu St Fsp Q Rt Gph
COH Gt Mu Fsp Sill Q Rt Gph
COH Gt Mu Bio Fsp Sill Q Ilm Gph
Gt Melt Bio Fsp Sill Q Ilm Gph
Gt Melt Fsp Sill Q Ilm Gph
COH Gt Bio Fsp Sill Q Ilm Gph
Gt Melt Crd Fsp Sill Q Ilm Gph
COH Gt Bio Fsp And Q Ilm Gph
COH Gt Bio Crd Fsp Sill Q Ilm Gph
P(kbar)
T(ºC)
B XCa Garnet XMg Garnet
C XNa Feldspar XMg Garnet
D
(1) COH Gt Mu Pa St Fsp Q Rt Gph (2) Gt Mu Pa St Fsp Q Rt Gph (3) COH Gt Mu Pa St Fsp Ky Q Rt Gph (4) COH Gt Mu Pa Fsp Ky Q Rt Gph (5) COH Gt Mu St Fsp Q Rt Ilm Gph (6) COH Gt Mu St Fsp Sill Q Rt Ilm Gph
(7) COH Gt Mu St Fsp Sill Q Ilm Gph (8) COH Gt Mu St Bi Fsp Sill Q Ilm Gph (9) COH Gt Mu St Bi Fsp Q Ilm Gph (10) COH Gt Mu St Fsp Q Ilm Gph (11) COH Gt Mu Fsp Sill Q Ilm Gph (12) COH Gt Mu Fsp Sill Q Rt Ilm Gph
(13) COH Gt Mu Bi Fsp Sill Q Rt Ilm Gph (14) COH Gt Mu St Fsp Sill Q Rt Gph (15) COH Gt Melt Mu Fsp Ky Q Rt Gph (16) COH Gt Melt Mu Fsp Sill Q Rt Gph (17) COH Gt Melt Mu Bi Fsp Sill Q Rt Ilm Gph (18) COH Gt Melt Mu Bi Fsp Sill Q Ilm Gph
(19) COH Melt Mu Bi Fsp Sill Q Ilm Gph (20) COH Melt Mu Bi Fsp Sill Q Rt Ilm Gph (21) Gt Melt Mu Fsp Sill Q Rt Ilm Gph (22) Gt Melt Bi Fsp Sill Q Rt Gph (23) Gt Melt Fsp Sill Q Rt Ilm Gph (24) Gt Melt Bi Crd Fsp Sill Q Ilm Gph
(25) COH Gt Melt Bi Crd Fsp Sill Q Ilm Gph (26) COH Gt Melt Bi Fsp Sill Q Ilm Gph (27) COH Gt Bi Crd Fsp And Q Ilm Gph (28) Gt Melt Fsp Ky Q Rt Gph (29) Gt Mu Pa St Fsp Ky Q Rt Gph (30) COH Gt Mu St Fsp Ky Q Rt Gph

Figure 17

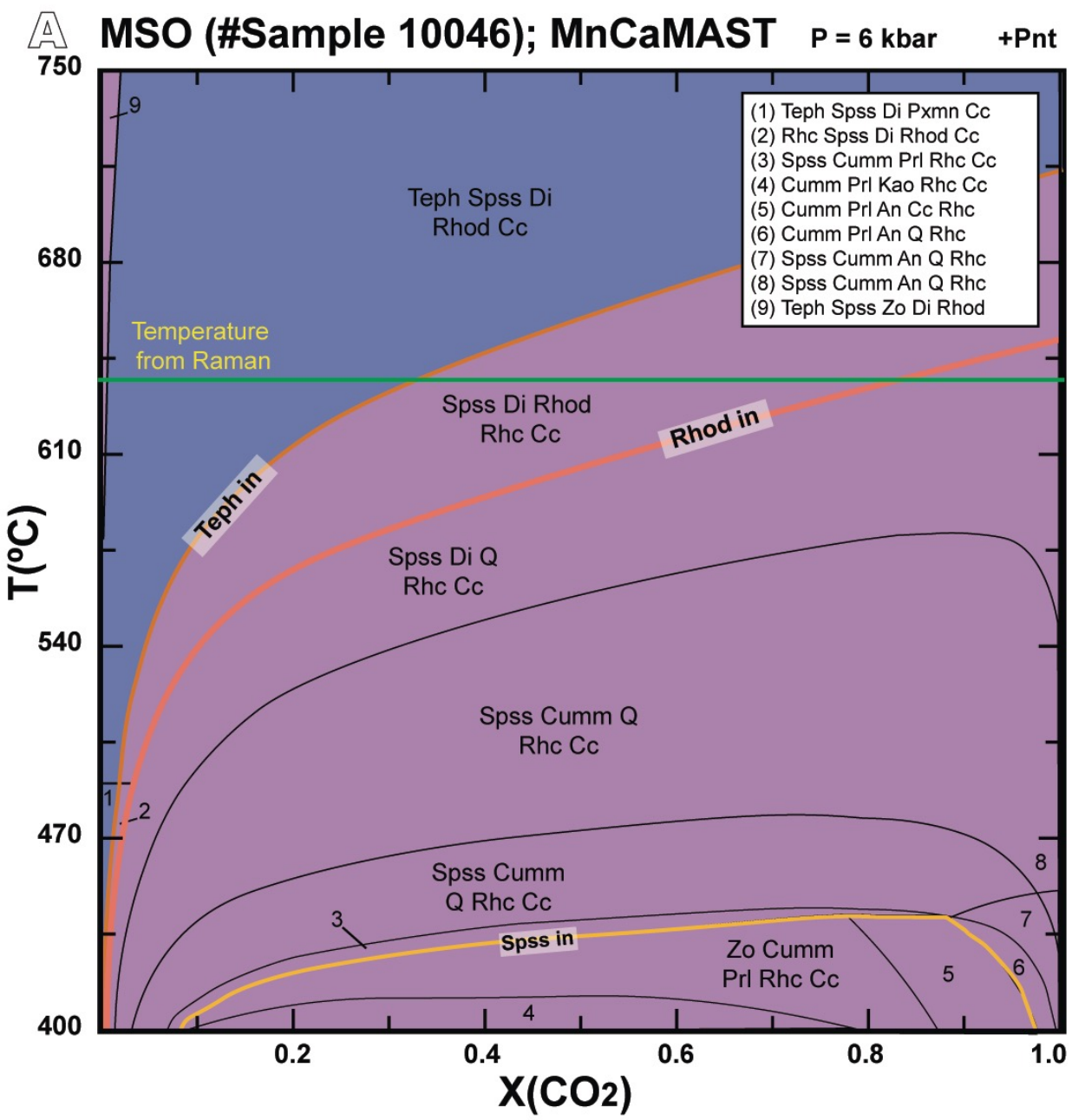
A
MSO (#Sample 10046); MnCaMAST
P = 6 kbar
+Pnt
(1) Teph Spss Di Pxmn Cc
(2) Rhc Spss Di Rhod Cc
(3) Spss Cumm Prl Rhc Cc
(4) Cumm Prl Kao Rhc Cc
(5) Cumm Prl An Cc Rhc
(6) Cumm Prl An Q Rhc
(7) Spss Cumm An Q Rhc
(8) Spss Cumm An Q Rhc
(9) Teph Spss Zo Di Rhod
Teph Spss Di Rhod Cc
Temperature from Raman
Spss Di Rhod Rhc Cc
Rhod in
Teph in
Spss Di Q Rhc Cc
Spss Cumm Q Rhc Cc
Spss Cumm Q Rhc Cc
Spss in
Zo Cumm Prl Rhc Cc
T(°C)
X(CO2)
750
680
610
540
470
400
0.2
0.4
0.6
0.8
1.0

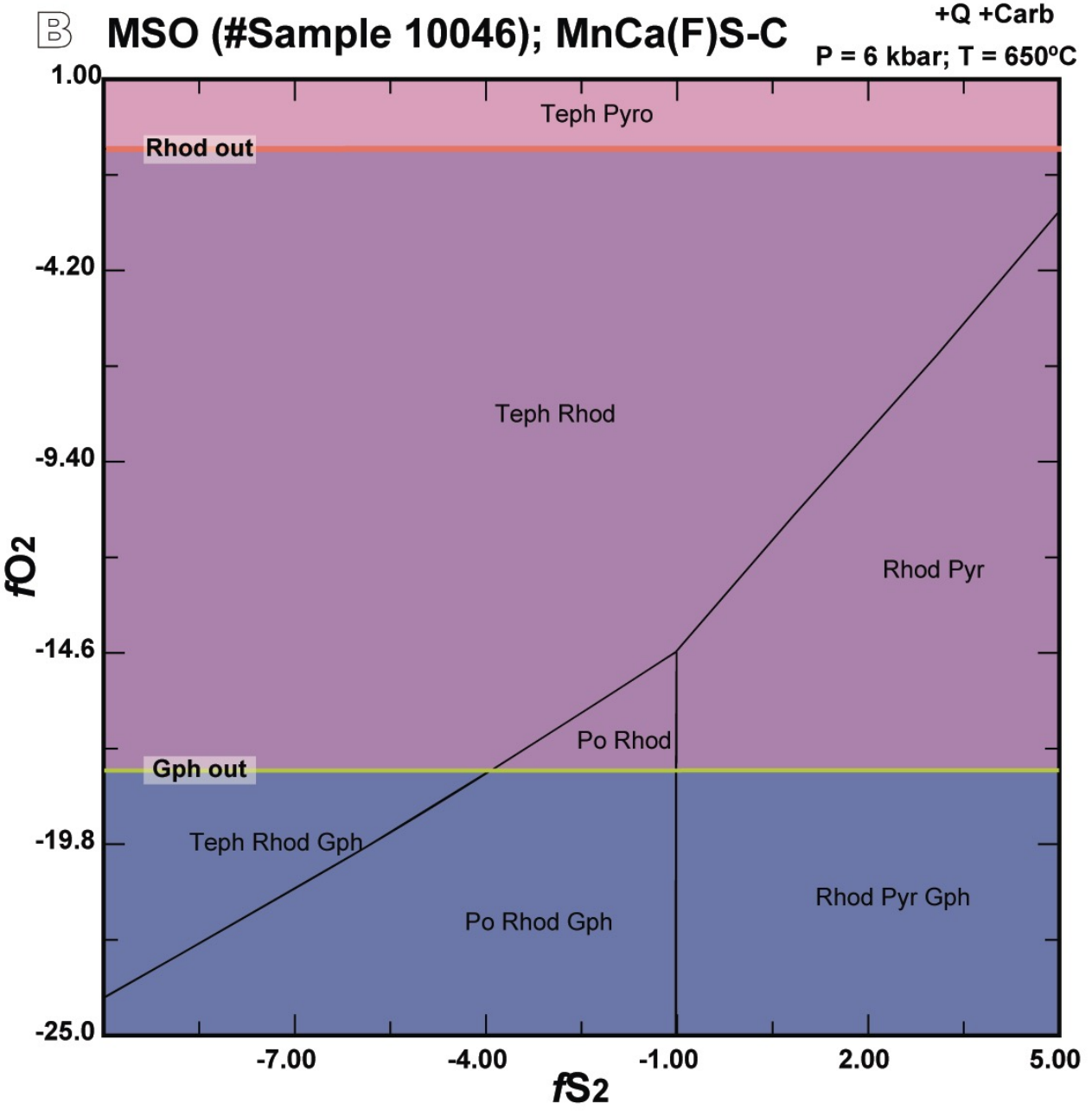
B
MSO (#Sample 10046); MnCa(F)S-C
+Q +Carb
P = 6 kbar; T = 650°C
Teph Pyro
Rhod out
Teph Rhod
Rhod Pyr
Po Rhod
Gph out
Teph Rhod Gph
Po Rhod Gph
Rhod Pyr Gph
fO2
fS2
1.00
-4.20
-9.40
-14.6
-19.8
-25.0
-7.00
-4.00
-1.00
2.00
5.00

Figure 18

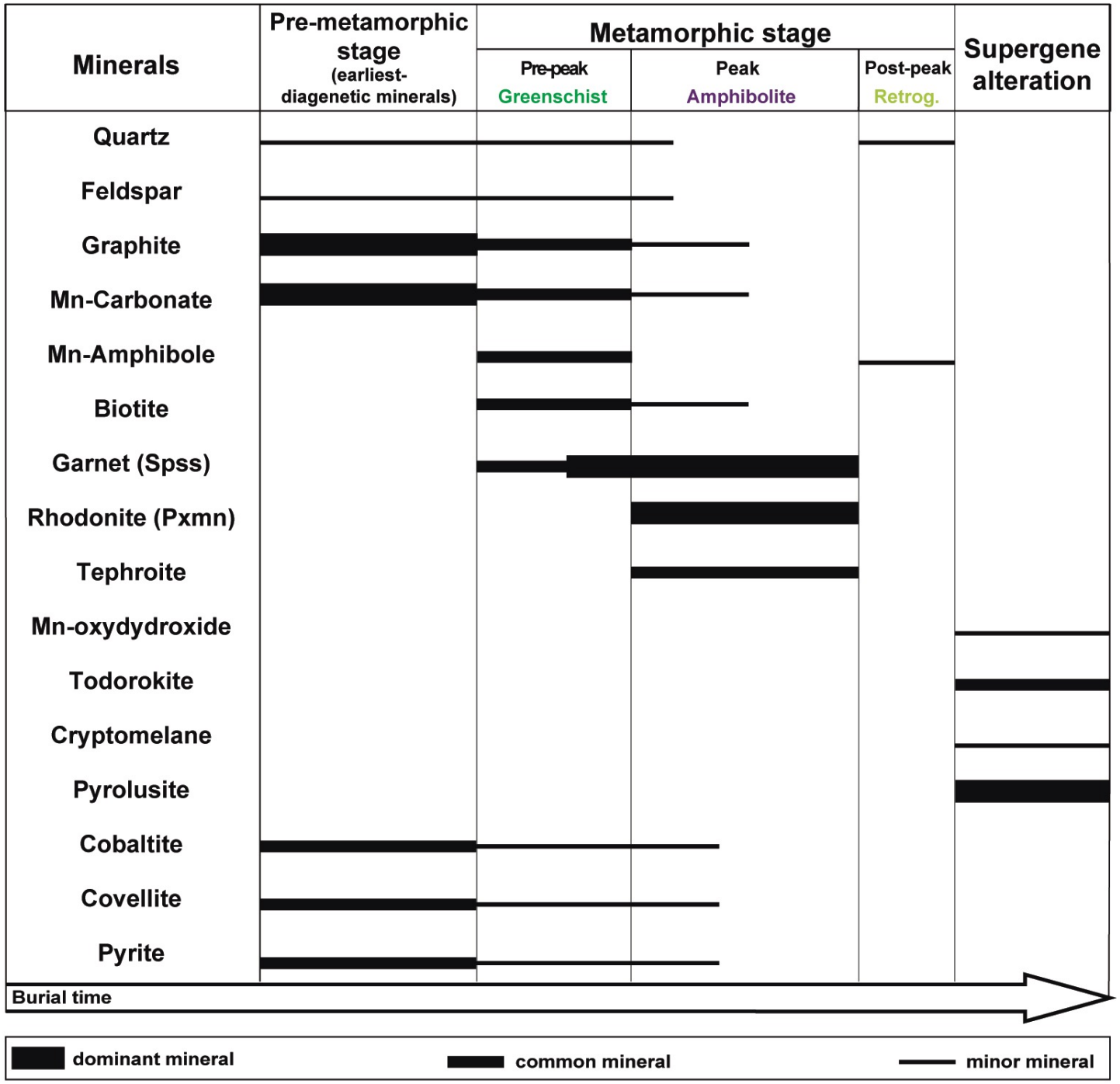
Minerals
Pre-metamorphic stage (earliest-diagenetic minerals)
Metamorphic stage
Pre-peak Greenschist
Peak Amphibolite
Post-peak Retrog.
Supergene alteration
Quartz
Feldspar
Graphite
Mn-Carbonate
Mn-Amphibole
Biotite
Garnet (Spss)
Rhodonite (Pxmn)
Tephroite
Mn-oxydydroxide
Todorokite
Cryptomelane
Pyrolusite
Cobaltite
Covellite
Pyrite
Burial time
dominant mineral
common mineral
minor mineral

Figure 19

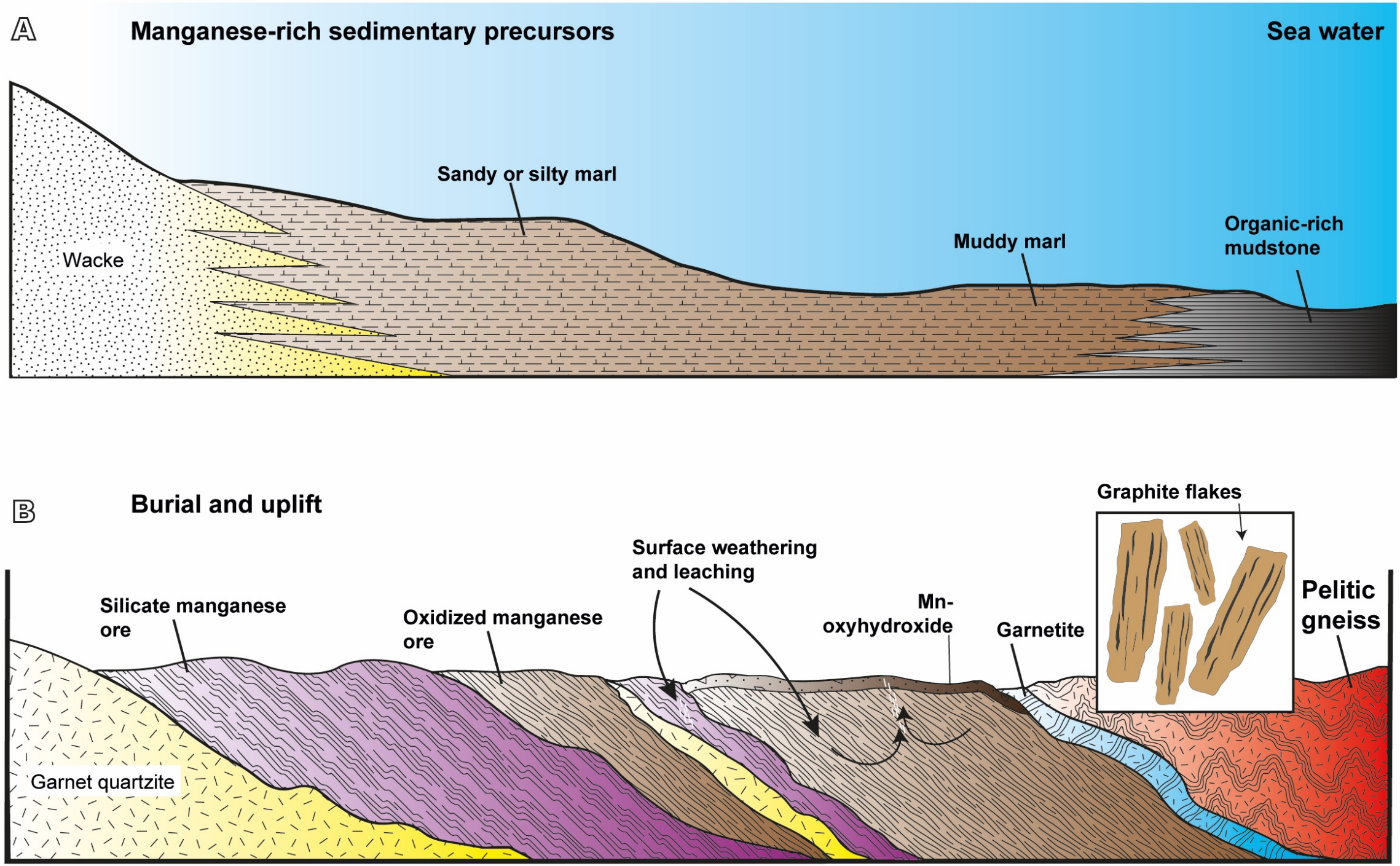
A
Manganese-rich sedimentary precursors
Sea water
Sandy or silty marl
Wacke
Muddy marl
Organic-rich mudstone
B
Burial and uplift
Graphite flakes
Surface weathering and leaching
Silicate manganese ore
Oxidized manganese ore
Mn-oxyhydroxide
Garnetite
Pelitic gneiss
Garnet quartzite